

Gamma-ray Spectroscopy of $T_z = \pm\frac{3}{2}$ Mirror Nuclei in the $f_{7/2}$ Shell: Isospin Breaking Effects at Large Proton Excess

James Robert Brown

A Thesis submitted for the degree of Doctor of Philosophy

Department of Physics

University of York

September 2009



Abstract

Isospin-breaking effects have been observed for the first time in $T = \frac{3}{2}$ isobaric analogue states in the fp shell. Gamma decays have been observed from $T_z = -\frac{3}{2}$ nuclei, ^{49}Fe and ^{53}Ni —presented here in new level schemes—and mirror energy differences have been computed following observation of analogue states in ^{49}V and ^{53}Mn , respectively.

The following details an attempt to observe excited states in ^{49}Fe using conventional fusion-evaporation techniques. Although ^{49}Fe was not populated at the expected level, it is shown that using new, meticulous analysis techniques developed as part of this thesis work, γ -ray spectroscopy at the sub-microbarn level can be achieved.

Following the failure to observe any excited states in ^{49}Fe using fusion-evaporation reactions, a new experimental method was developed. A high-luminosity, two-step fragmentation process was employed to allow access to highly proton-rich nuclei. Each member of a mirror pair was produced via mirrored fragmentation of a ^{56}Ni secondary beam, allowing observation of excited states by performing γ -ray spectroscopy on the fast moving fragments using the SeGA spectrometer. The $A = 49$ and $A = 53$, $T_z = \pm\frac{3}{2}$ mirror pairs were populated in mirrored fragmentation reactions, allowing the assignment of spins and parities of isobaric analogue states purely on mirror symmetry arguments. This work represents the first study of its kind and demonstrates the power of this approach for future studies of isobaric analogue states in very proton-rich systems.

An investigation of population asymmetry of isobaric analogue states following mirrored fragmentation reactions was also undertaken by studying γ -ray intensities in the well known $A = 54$, $T_z = \pm 1$ mirror pair. Observed population intensities were compared to two-particle knockout models.

Shell model calculations in the fp shell were carried out, with the inclusion of

isospin-breaking effects of both Coulomb and nuclear origin. Calculated mirror energy differences were found to be in good agreement with the data and reveal, for the first time, the importance of non-Coulomb isospin-breaking effects in $T = \frac{3}{2}$ isobaric analogue states.

Acknowledgements

The following work could not have been achieved without the help and support of a great many people. Firstly, I'd like to thank Mike Bentley, not only for his supervision over the last four years—which has always been carried out with a smile and a joke—but for having the confidence to take me on as a student after two years away from physics.

Other members of the nuclear physics group have also been of great help, particularly Mike Taylor for his technical support in the early days, Charles Barton, David Jenkins and Bob Wadsworth, for clarifying various subtleties of nuclear physics, and John, Paul, Mike and Christian for discussing numerous (mostly) physics issues over a bottomless cup of tea. Thanks also to Paul Kent, for his unique and *challenging* approach to working together.

Many collaborators have made this work possible, but special thanks must go to Alison Bruce and Silvia Lenzi for patiently teaching me the ways of the shell model, and Jeff Tostevin for his insight into two-nucleon knockout. The staff at Argonne and NSCL must be thanked for making the experiments possible when I had little idea what was going on, particularly Kim Lister and Darek Seweryniak at Argonne, and Kyle Siwek and Dirk Weisshaar who taught me all I know about MSU data analysis. Many thanks also go to the students at MSU who kept me sane, with beer and baseball, during what I hope was the most intense period of work I'll ever undertake.

Thanks also to Paul and Clare for letting me drag them out climbing when I needed to clear my head, and to everyone else who has made the last four years in York so enjoyable.

I should also thank my family for all their support, and for absolutely everything else, I must thank Esther.

Declaration

This thesis has been submitted for the degree of Doctor of Philosophy, in accordance with the regulations of the University of York. The work described herein has not been submitted for any other degree or qualification.

All work was carried out under the supervision of Prof. M. A. Bentley. Experimental work was undertaken in collaboration with staff at the Argonne National Laboratory and the National Superconducting Cyclotron Laboratory of Michigan State University, as well as other collaborators. Elements of the analysis described in Chapters 2, 4 and 5 were performed in conjunction others. This is clearly indicated at the relevant points in the text.

Contents

Abstract	1
Acknowledgements	3
Declaration	4
An Introduction to Isospin Breaking	16
1 Aspects of nuclear structure	18
1.1 The liquid drop model	18
1.2 The shell model	20
1.2.1 Nuclear potentials	21
1.2.2 Spin-orbit splitting	22
1.2.3 The residual interaction	23
1.2.4 The $f_{7/2}$ shell	24
1.3 Isospin and mirror nuclei	24
1.3.1 Mirror displacement energies	25
1.3.2 Mirror energy differences	26
1.3.3 Isospin breaking forces	27
2 Gamma-ray spectroscopy at the microbarn level	33
2.1 Fusion-evaporation reactions	33
2.2 Experimental detail	34
2.2.1 The Fragment Mass Analyzer	35
2.2.2 The Gammasphere array	37
2.3 Data Analysis	38
2.3.1 Data compression	39

2.3.2	Production of clean γ -ray spectra	40
3	Results of microbarn γ-ray spectroscopy	50
4	High-luminosity mirrored fragmentation reactions	52
4.1	Radioactive ion beams	52
4.1.1	Isotope Separation On-Line	53
4.1.2	Projectile Fragmentation	53
4.2	Beam production and the A1900	55
4.3	The S800 Spectrograph	57
4.3.1	Focal plane detectors	58
4.3.2	Aberration correction	60
4.3.3	Particle identification with the S800 spectrograph	61
4.4	The SeGA array	63
4.4.1	Energy and efficiency calibration of SeGA	66
4.4.2	Doppler reconstruction of γ rays	68
4.4.3	Production of clean γ -ray spectra	69
5	Results from fragmentation reactions	74
5.1	The $A=49$, $T_z = \pm\frac{3}{2}$ mirror pair	75
5.1.1	Spectroscopy of ^{49}V	75
5.1.2	Spectroscopy of ^{49}Fe	80
5.2	The $A=53$, $T_z = \pm\frac{3}{2}$ mirror pair	84
5.2.1	Spectroscopy of ^{53}Mn	84
5.2.2	Spectroscopy of ^{53}Ni	88
5.2.3	The $J^\pi = \frac{5}{2}^-$ state	89
5.3	Population anisotropies following mirrored fragmentation reactions . . .	93
5.3.1	Direct vs. indirect reactions	97
5.3.2	Lifetime of the 6^+ states	100
6	Shell-model calculations in the $f_{7/2}$ shell	105
6.1	Principles of shell-model calculations	105
6.1.1	Effective interactions	106
6.1.2	Truncations	106
6.2	Calculations of isospin-breaking terms	107

6.3	Results of shell-model calculations	110
6.3.1	The $A=49$ mirror pair	110
6.3.2	The $A=53$ mirror pair	115
6.3.3	The $A=54$ mirror pair	118
7	Conclusions	122
7.1	The future of fusion-evaporation experiments for the study of proton-rich nuclei	122
7.2	Further fragmentation experiments	123
7.3	The status of isospin-breaking phenomena	124
	List of Abbreviations	126
	Bibliography	129

List of Figures

1.1	Binding energy per nucleon curve for stable nuclei. The data points represent experimental data, while the line is the result of calculations with the semi-empirical mass formula (see Eqn. 1.1) with coefficients of $a_v = 15.8$ MeV, $a_s = 18.3$ MeV, $a_C = 0.7$ MeV, $a_a = 23.2$ MeV and $a_p = 12$ meV (taken from [12]).	19
1.2	Comparison of the general form of Woods-Saxon and harmonic oscillator potentials. The Woods-Saxon is a realistic potential with a uniform central region and a diffuse surface. The harmonic oscillator is a reasonable approximation to this.	22
1.3	Calculation of the probability distribution for the separation of a pair of nucleons coupled to different angular momenta J . The centre of each plot corresponds to zero separation between the nucleons. Image taken from [11], from calculations carried out in [15]. (Original in colour.) . .	28
1.4	Mirror energy differences for the $A = 42$ mirror pair, compared to harmonic oscillator CME (with the ground state normalised to zero) and the $A = 54$ mirror pair (plotted as $-MED$ as the $(f_{7/2})^{-2}$ configuration will lead to active proton-holes in ^{54}Fe , rather than ^{54}Ni). Note the discrepancy between the general downward trend of the CME, compared to the increase at $J = 2$ for the MED.	31
2.1	Schematic diagram of the elements of the FMA, showing the quadrupole doublets (Q1-4), electric dipoles (ED1/2) and magnetic dipole (MD). The target (t) and degrader foil (d) are shown, along with the Gamma-sphere array (GS). The slits (s) and focal plane detectors—ion chamber (IC) and micro-channel plate (MCP)—can also be seen after Q4.	36

2.2	Schematic diagram of the Argonne micro-channel plate detector, taken from [22].	37
2.3	Schematic diagram showing the segmentation of the Gammasphere crystals. The different hit regions described in the text are indicated. . . .	38
2.4	Example ΔE – E matrix used for identification of Z . E is on the x -axis and ΔE_1 on the y -axis. Each downward slanting distribution corresponds to residues of a different atomic number. (Original in colour.) . . .	42
2.5	Gamma-ray spectra produced in coincidence with Fe residues using three different ΔE – E matrices, see text for details. The multiple-matrix technique significantly reduces statistics but improves the ratio of Fe to nearby isotopes (^{49}Cr and ^{49}Mn). γ rays from other strongly populated isotopes such as V, present due to random coincides, remain in approximately the same proportion. (Original in colour.)	42
2.6	Plots of A/Q , as measured with the MCP for (a) Cr isotopes, dominated by ^{49}Cr , and (b) Mn isotopes, composed of slightly more ^{52}Mn than ^{49}Mn . Differences between the distributions are apparent but with insufficient dispersion for effective mass selection.	43
2.7	Mass spectrum for Cr isotopes, produced using the Et^2 technique (see text for details). The single peak corresponds to ^{49}Cr —the only Cr isotope produced in this experiment—and demonstrates the ~ 2.5 amu resolution achievable with this technique.	45
2.8	A vs. A/Q plot gated on $Z = 25$ residues. A is derived from measurements of Et^2 and A/Q from the MCP. The two overlapping but discernible regions correspond to ^{49}Mn and ^{52}Mn . Polygonal gates can be applied to plots such as these to uniquely select the nucleus of interest without inclusion of any neighbouring isotopes. (Original in colour.) . . .	45
2.9	Gamma-ray spectrum produced by selecting $Z = 26$, $A = 49$ residues, with timing conditions and background subtraction. The spectrum is dominated by $A = 49$ residues other than ^{49}Fe , with small amounts of other isotopes, e.g. ^{46}Ti	48
2.10	^{49}Fe gated spectrum with background subtractions, see text for details.	49

4.1	Schematic of the A1900 fragment separator and the K500 and K1200 coupled cyclotrons, taken from [37].	55
4.2	Time-of-flight spectrum of the secondary beam, measured between the XFP and OBJ scintillators	57
4.3	Schematic image of the S800 spectrograph with the SeGA array installed at the target position. The blue and yellow objects are the magnetic dipoles and quadrapoles of the analysis line. The OBJ scintillator is located at the left edge of the image. The S800's superconducting dipole magnets are shown in brown and the focal plane detectors in red. (Original in colour.)	58
4.4	Detail of S800 focal plane detectors, taken from [40].	59
4.5	PID used to identify reaction products at the focal plane of the S800. Corrected time-of-flight measured from the OBJ to E1 scintillators is plotted on the x -axis, with energy loss (ΔE) in the ionisation chamber shown on the y -axis. (Original in colour.)	63
4.6	Schematic of the Segmented Germanium Array, viewed from upstream. The two detector rings at 37° and 90° are visible, along with the target position shown in blue. Note that, in his work, one detector was absent from each ring. Image taken from [40]. (Original in colour.)	64
4.7	Schematic diagrams of a SeGA crystal. The radial and lateral segmentation is shown and the labelling convention used to identify them.	65
4.8	Flowchart depicting the process used to assign the first segment hit for use in the Doppler reconstruction.	67
4.9	Efficiency curve for the forward ring of SeGA. Data points are measured with a ^{152}Eu source, the line is a fit to this data.	68
4.10	Gamma-ray spectrum created in coincidence with ^{56}Ni recoils. Decays from the $J^\pi = 6^+, 4^+$ and 2^+ states can be seen following inelastic scattering of the ^{56}Ni beam.	70
4.11	γ -ray timing spectra for the raw TDC values and relative to the OBJ scintillator. The timing window applied is indicated. (Original in colour.)	71
4.12	γ -ray spectra in coincidence with ^{48}Cr recoils, with and without time-gates. The reduction of the <i>bremsstrahlung</i> background is clear. (Original in colour.)	72

4.13	γ -ray spectra produced in coincidence with ^{53}Mn recoils, with various gating conditions applied. See text for details. (Original in colour.) . . .	73
5.1	Gamma-ray spectrum produced in coincidence with ^{49}V recoils at the focal plane. The spectrum has been enhanced above 1.4 MeV to show the weak, high-energy peaks more clearly. Peaks labelled in parentheses are tentative but included for completeness.	75
5.2	Level scheme of ^{49}V showing the γ rays observed in this work. Energies, ordering, and spins and parities are taken from [17]. Tentatively observed γ rays are labelled in parentheses. Transition widths are proportional to γ ray intensities measured in this work.	76
5.3	Gamma-ray spectrum produced in coincidence with ^{49}V recoils and the 1022 keV γ -ray transition.	77
5.4	Gamma-ray spectrum in coincidence with ^{49}V recoils with additional timing conditions applied. (Original in colour.)	79
5.5	Gamma-ray spectra of ^{49}V (top) and ^{49}Fe (bottom) with timing conditions applied. Gamma-ray energies of peaks of interests are labelled and mirrored transitions are indicated.	80
5.6	(a) Partial level scheme of ^{49}V as observed in this work. All values, except intensities, are taken from [17]. (b) Proposed level scheme for ^{49}Fe constructed based on mirror symmetry arguments. The 1101 keV γ ray could be attributed to decays from two possible states, both of which are displayed tentatively, see text for details. Transition widths are proportional to γ -ray intensities.	83
5.7	Gamma-ray spectrum produced in coincidence with ^{53}Mn recoils detected at the focal plane. Above 1.7 MeV the spectrum has been rebinned to 16 keV/channel to show the weak, high-energy transitions. . .	84
5.8	Partial level scheme of ^{53}Mn showing the γ -rays and states observed in this work. Transition widths are proportional to measured intensities. Energies, ordering, and spins and parities of states are taken from [52].	85

5.9	Gamma-ray spectrum produced in coincidence with ^{53}Mn recoils and the ~ 1120 keV γ ray. Presence of the 1441 keV peak and absence of the 378 keV peak indicates the ~ 1120 keV peak belongs mainly to the 1122 keV $\frac{13}{2}^-$ to $\frac{11}{2}^-$ transition.	86
5.10	(a) ^{53}Mn spectrum created with timing and multiplicity conditions. (b) Gamma-ray spectrum created in coincidence with ^{53}Ni recoils with identical timing and multiplicity conditions as applied to ^{53}Mn . Mirrored transitions are indicated. The energy of the low energy peak is discussed in Section 5.2.3.	88
5.11	^{53}Mn γ -ray spectrum showing the shift of the 378 keV peak resulting from its 117 ps lifetime.	89
5.12	Plot demonstrating the iterative process used to determine the energy and half-life of the $J^\pi = \frac{5}{2}^-$ state in ^{53}Ni . With successive iterations the large fluctuations quickly converge, see text for details.	91
5.13	(a) Partial level scheme of ^{53}Mn , created as in Fig. 5.8. (b) New level scheme of ^{53}Ni created in this work. Spins and parities are tentative as they are assigned based purely on mirror symmetry arguments. Transition widths are proportional to relative intensities measured in this work.	92
5.14	(a) Gamma-ray spectrum in coincidence with ^{54}Fe recoils. (b) ^{54}Ni γ -ray spectrum. Both spectra are made without additional gating conditions. The peaks labelled 411 and 451 keV are shifted, as discussed in Sec. 5.3.2.	94
5.15	Partial level schemes of (a) ^{54}Fe and (b) ^{54}Ni states observed in this work. Energies of γ rays, and the ordering, energies, spins, and parities of states are taken from [55] and [9] for (a) and (b) respectively. Transition widths are proportional to relative γ -ray intensities, measured in this work.	95
5.16	Nucleon removal threshold diagrams for ^{56}Ni , supplied by Jeff Tostevin [59]. The yellow regions represent the energy window for two nucleon knockout, orange regions denote single nucleon removal to bound states, while blue regions show the window for single nucleon removal to unbound states. (Original in colour.)	98
5.17	Spectra showing the shifts in energy of the γ decays from the 6^+ states of (a) ^{54}Fe and (b) ^{54}Ni	101

- 5.18 ^{54}Ni spectra before the Doppler correction is applied for the 37° (top) and 90° (bottom) detector rings, with the Doppler corrected spectra from all detectors (middle). The ^{54}Ni transitions of interest are labelled, and the origins of these peaks in the uncorrected spectra are indicated. Several additional peaks are evident in the uncorrected spectra which must originate from stationary sources, see text for details. 102
- 6.1 Theoretical and experimental energy levels for ^{53}Mn , showing the evolution of theoretical levels with t , i.e. the number of excitations allowed to the upper fp shell. Note that a $J^\pi = 13/2^-$ state cannot be made from a pure $\pi(f_{7/2})^{-3}$ configuration, hence is not present in the $t = 0$ scheme. Theoretical energies converge towards experimental values, reaching good agreement by $t = 5$ 107
- 6.2 Proton and neutron occupation numbers in ^{49}Cr for the $p_{3/2}$, $f_{5/2}$, and $p_{1/2}$ orbitals, with the fractional occupation of the $f_{7/2}$ shell, e.g. $m_{\pi f_{7/2}}/4$. Note that the $p_{1/2}$ occupation is negligible and the $f_{7/2}$ occupation increases, with a corresponding decrease in $p_{3/2}$, as the band termination at $J^\pi = 31/2^-$ is approached. (Original in colour.) 109
- 6.3 Contributions to the $A = 49$, $T_z = \pm 3/2$ MED from individual isospin-breaking terms, along with the resultant predicted MED curve. See text for details. (Original in colour.) 110
- 6.4 Experimental and theoretical mirror energy differences for the $A = 49$, $T_z = \pm 3/2$ mirror pair. 113
- 6.5 Final ^{49}Fe level scheme, taking into account shell-model calculations and incorporating the states observed by Dossat *et al.* [51]. See text for details. 115
- 6.6 Individual isospin breaking contributions to the MED of the $A=53$, $T_z = \pm 3/2$ mirror pair, along with the total calculated MED. The V_{CM} term is included with and without the V_{Cu} and V_{Cl_s} terms to indicate the influence of these single-particle effects. (Original in colour.) 116
- 6.7 The experimental and theoretical MED curves for the $A=53$, $T_z = \pm 3/2$ mirror pair. 118
- 6.8 (b) Revised ^{54}Ni level scheme following the considerations discussed in the text. (a) ^{54}Fe level scheme for comparison. 120

List of Tables

1.1	Coulomb (V_C) and nuclear (V_B) isospin breaking two-body matrix elements in the $f_{7/2}$ shell, in keV. CME are calculated with the harmonic oscillator potential, taken from reference [16]. Nuclear matrix elements are extracted from the $A = 42$ and 54 MED. In each case, following the methodology of Zuker <i>et al.</i> [8], the centroids, $V_{centr} = \frac{\sum_J[V(2J+1)]}{\sum_J(2J+1)}$ have been subtracted in order to aid comparison. Though the values for V_B are derived from experimental values, no uncertainties are quoted here as these are intended as indicative values rather than genuine measurements of matrix elements.	32
2.1	Table summarising the segmentation routine carried out in order to minimise Doppler broadening. The ratio of energies detected in the side channel and central contacts is used, i.e. $R_{seg.} = E_{side}/E_{cent.}$	41
2.2	Table of predicted cross sections for the ten strongest exit channels from the $^{40}\text{Ca}+^{12}\text{C}\rightarrow^{52}\text{Fe}^*$ reaction, calculated using PACE 4 [28].	48
4.1	Main constituents of the secondary beam, as delivered to the reaction target, measured using the time-of-flight spectra in Fig. 4.2.	56
5.1	Details of excited states of ^{49}V observed in this experiment. All values, except relative γ -ray intensities ($I_{\gamma(rel)}$), are taken from [17].	78
5.2	Details of excited states observed in ^{49}Fe , with details of relevant isobaric analogue states in ^{49}V included for comparison. Ground state half-lives for ^{49}Fe and ^{49}V are taken from [51] and [17] respectively.	82
5.3	Details of excited states of ^{53}Mn observed in this experiment. All values, except relative γ -ray intensities ($I_{\gamma(rel)}$), are taken from [52].	87

5.4	Details of new excited states observed in ^{53}Ni , with details of relevant isobaric analogue states in ^{53}Mn included for comparison. Ground state half-life for ^{53}Ni and ^{53}Mn are taken from [51] and [52] respectively. . .	93
5.5	Details of excited states observed in ^{54}Fe and ^{54}Ni . All values except relative γ -ray intensities are taken from [55] for ^{54}Fe and [9] and [55] for ^{54}Ni	96
5.6	Proton (S_π) and neutron (S_ν) separation energies produced in Hartree-Fock calculations for the sub-shells in ^{56}Ni , taken from [59], along with the maximum occupation of each sub-shell (occ.).	99
5.7	Relative isotopic abundances in natural Ge.	103
5.8	Table identifying the origin of various γ -ray background peaks observed in this work, taken from [64]. Letters refer to peaks labelled in Fig. 5.18.	104
6.1	Calculated $B(E2)$ values for $6^+ \rightarrow 4^+$ transitions and half-lives ($t_{1/2}$) for the 6^+ states of ^{54}Fe and ^{54}Ni . Half-lives are calculated using experimental γ -ray energies, see text for details. Experimental values for ^{54}Fe (taken from ref. [55]) are also presented.	119

An Introduction to Isospin Breaking

Charge symmetry and charge independence of the nuclear force are two of the underlying principles of nuclear physics. From these assumptions, we would expect perfect degeneracy between isobaric analogue states, save for the effects of the Coulomb force. Precise measurements of nucleon-nucleon scattering, however, have demonstrated a slight charge asymmetry to the nuclear interaction (discussed fully in [1]). Furthermore, experimental data have long been available for the displacement energies between the ground states of mirror nuclei (mirror displacement energies, MDE), however the work of Nolen and Schiffer revealed that despite our good understanding of the Coulomb force, calculations of MDE are surprisingly inaccurate [2], providing strong evidence for charge-symmetry breaking (CSB) in bulk nuclear systems.

In spite of these observations, measurement of mirror energy differences—MED, i.e. the energy difference between excited analogue states in mirror nuclei (nuclei with exchanged numbers of protons and neutrons)—have been shown to be an effective probe of nuclear structure. This is due, in part, to the measurement of MED relative to the ground state so charge-symmetry breaking effects contributing to MDE are eliminated. This leaves only spin dependent contributions from (the well understood) Coulomb force, allowing insight into some subtle facets of nuclear structure.

Modern MED studies have developed from the instigative work of Cameron *et al.* [3], where mirror energy differences for the $A = 49$, $T_z = \pm\frac{1}{2}$ mirror pair, plotted as a function of spin, were interpreted intuitively in terms of particle alignments (angular momentum re-coupling) and used as a probe of subtle changes in nuclear structure. More recent MED studies have used state-of-the-art shell-model calculations, and devised methods for including isospin-breaking Coulomb terms to quantitatively interpret experimentally observed MED curves [4, 5, 6, 7, for example]. However, the need for

the introduction of a spin-dependent nuclear isospin-breaking term has become evident through the study of the $A = 42$ and 54 mirror pairs [8, 9], and the inclusion of such a term has been shown to be as important as contributions from the Coulomb force. Furthermore, evidence has been found to indicate the importance of charge symmetry-breaking effects in other $f_{7/2}$ nuclei [10]. Inclusion of this nuclear isospin-breaking force in shell-model predictions has now dramatically improved agreement between experiment and theoretical MED curves right across the $f_{7/2}$ shell [11], allowing theoretical reproduction of experimental MED curves to within tens of keV. The nature of this isospin breaking component to the nuclear force remains a mystery, moving mirror energy difference studies from a useful probe of nuclear structure, to an interesting research field in itself.

The following work represents continued efforts to understand this phenomenon by extending MED studies to more exotic systems with larger values of isospin. To date, MED studies in the $f_{7/2}$ shell have been limited to $|T_z| \leq 1$ mirror pairs. In the following work, experiments are undertaken to measure MED for $T_z = \pm\frac{3}{2}$ mirror pairs through gamma-ray spectroscopy following fusion-evaporation (Chapters 2 and 3) and high-luminosity fragmentation reactions (Chapters 4 and 5). In Chapter 1, an outline of nuclear models is given, along with details of isospin-breaking forces, and in Chapter 6 these models are used to perform shell-model calculations for comparison with experimental data. In Chapter 7, this work is discussed and conclusions drawn, along with a discussion of future work in this field.

Chapter 1

Aspects of nuclear structure

The atomic nucleus can be described effectively by a great many different models, some historical and obsolete, others complementary, describing different facets of nuclear behaviour. One overriding universality of these models is their phenomenological nature. The nucleus is, of course, constructed from protons and neutrons, which in turn are made up of quarks, however no model exists which can describe bulk nuclear behaviour from the fundamental perspective of quark-quark interactions (save perhaps for the simplest of nuclei). What follows is a brief introduction to some of the nuclear models and methods relevant to this work.

1.1 The liquid drop model

The liquid drop model approximates nuclear material to an incompressible fluid with uniform density. This assumption is reasonable when we consider the binding energy curve of Fig. 1.1. A great deal of nuclear physics can be inferred from this plot, including three of the key parameters of nuclear binding. Firstly, it indicates that the nuclear force quickly saturates at a little over 8 MeV per nucleon and adding more nucleons does not further increase the binding beyond its typical value. Hence, a first approximation to the nuclear potential will simply be proportional to the number of nucleons (A), i.e. $V_{nuc.} \propto a_v A$. This saturation implies the short range of the nuclear force, hence at the nuclear surface, there will be fewer nucleons to interact with one another. This will lead to a negative surface term in the nuclear potential, $-a_s A^{2/3}$. A further negative term will result from the Coulomb repulsion of the protons, which, due to the long range nature of the Coulomb interaction, will scale with the number of

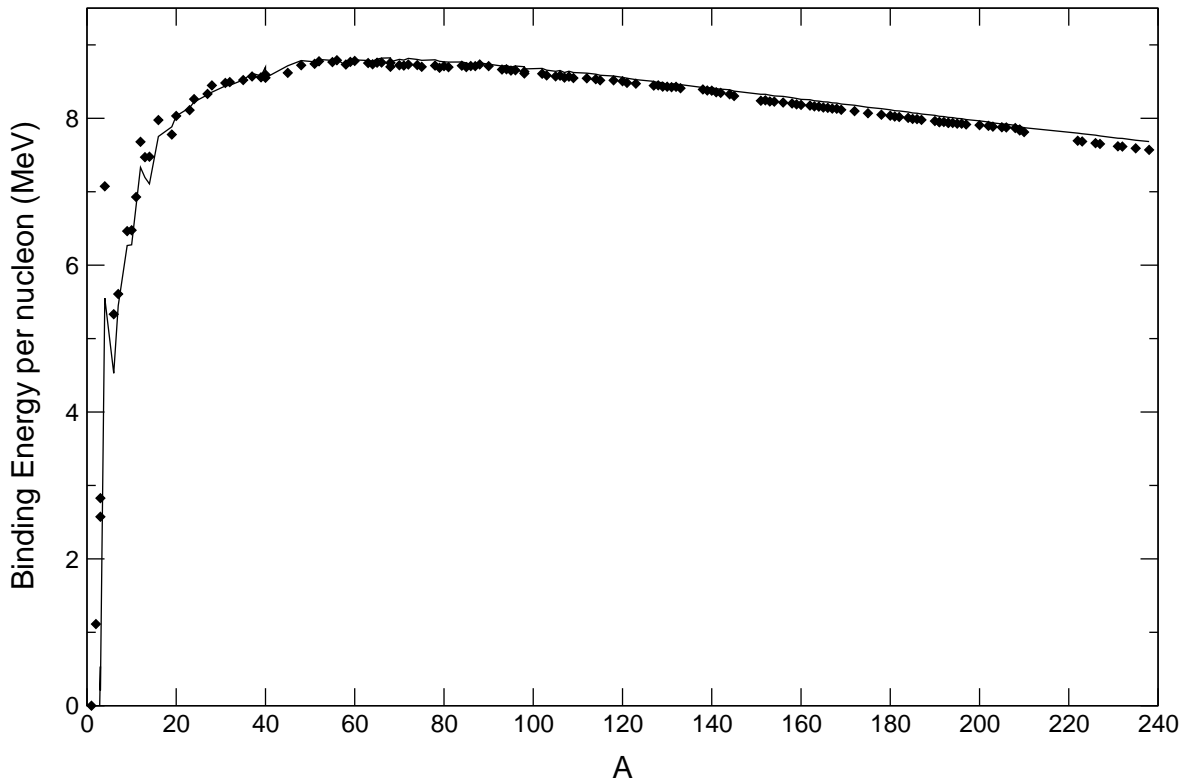


Figure 1.1: Binding energy per nucleon curve for stable nuclei. The data points represent experimental data, while the line is the result of calculations with the semi-empirical mass formula (see Eqn. 1.1) with coefficients of $a_v = 15.8$ MeV, $a_s = 18.3$ MeV, $a_C = 0.7$ MeV, $a_a = 23.2$ MeV and $a_p = 12$ MeV (taken from [12]).

interacting protons. The incompressibility of nuclear material implies that the volume of a nucleus (v) is proportional to the number of nucleons, hence the radius can be approximated by $1/r \propto A^{-1/3}$. We can then assume the Coulomb contribution to nuclear binding will be given by $-a_C Z(Z-1)A^{-1/3}$.

These three terms—only briefly outlined here—are the essence of the liquid drop model, however, treated alone they do not reproduce the binding energy curve in Fig. 1.1. In order to do so we must introduce two further terms which have their origins in the independent particle model. If we briefly borrow a result from Section 1.2—as nucleons are added into a nucleus they must fill, from the bottom, two independent sets of discrete energy levels, one for protons and one for neutrons—we immediately see that if we have a great disparity in the proton-to-neutron ratio, we have one set of energy levels filled far higher than the other. This suggests that in order to minimise its potential energy, the nucleus must maintain an equal number of protons and neutrons—neglecting of course the effects of the Coulomb force. We therefore expect a further asymmetry term to the nuclear interaction in the form $a_a(N-Z)^2/A$. This

contribution explains why stable nuclei up to the medium mass range tend to have roughly equal numbers of protons and neutrons. At larger masses, the long range Coulomb interaction becomes more significant and breaks this symmetry, requiring more neutrons to maintain stability.

The final term in this discussion stems from the result that binding energy can be gained by coupling a pair of like nucleons such that their angular momentum vectors are anti-aligned, i.e. their total angular momentum (J) is zero. This phenomenon is the origin of the familiar staggering in separation energy plots from odd to even mass nuclei. Here, this is quantified such that a gain in binding energy of $a_p A^{-1/2}$ is obtained for even-even nuclei where every nucleon is paired off, odd-odd nuclei lose an equal amount, while odd mass nuclei are unchanged.

Summing these five terms results in a formula for the total binding energy ($B.E$) of the nucleus known as the semi-empirical or Weizsäcker mass formula:

$$B.E = a_v A - a_s A^{2/3} - a_C Z(Z-1)A^{-1/3} - \frac{a_a(N-Z)^2}{A} \pm \delta \quad (1.1)$$

where $\pm\delta = +a_p A^{-1/2}$, $-a_p A^{-1/2}$ or 0 for even-even, odd-odd, and odd mass nuclei respectively. This function, with appropriate coefficients, can now effectively reproduce the experimental binding energy curve, as can be seen in Fig. 1.1.

1.2 The shell model

An alternative approach to understanding nuclear interactions starts from a more fundamental level. By assuming that the nuclear potential can be approximated by two-body interactions between nucleons, the Hamiltonian is given by

$$H = T + V = \sum_{i=1}^A \frac{\mathbf{p}_i^2}{2m_i} + \sum_{i>k=1}^A V_{ik}(\mathbf{r}_i - \mathbf{r}_k). \quad (1.2)$$

This Hamiltonian has $3 \times A$ coordinates, hence becomes extremely complex for all but the lightest nuclei. This can be simplified by using a mean field $U_i(\mathbf{r})$, which acts on all nuclei, rather than considering the individual nuclear interactions. Thus, the

Hamiltonian may now be written

$$H = \sum_{i=1}^A \left[\frac{\mathbf{p}_i^2}{2m_i} + U_i(\mathbf{r}) \right] + \sum_{i>k=1}^A V_{ik}(\mathbf{r}_i - \mathbf{r}_k) - \sum_{i=1}^A U_i(\mathbf{r}) \equiv H_0 + H_{res.} \quad (1.3)$$

The aim is then to find a potential which acts on all nucleons, approximating a real two-body potential such that the residual interaction ($H_{res.}$) is a small perturbation on H_0 , which accounts for the remainder of the effects of nucleon-nucleon interactions.

1.2.1 Nuclear potentials

A number of potentials are suitable for this task but one common feature is the use of spherically-symmetric central potentials. By expressing position vectors in polar coordinates, angular and radial components can be separated, simplifying the problem. This results in the orbital angular momentum dependence of energy levels and leads to a basic shell structure. One of the most realistic potentials available is the Woods-Saxon potential, with the form

$$V(r) = \frac{V_0}{1 + \exp\left(\frac{r-R_0}{a}\right)}, \quad (1.4)$$

where V_0 is the depth of the potential well, R_0 is the nuclear radius, and a is the surface diffuseness term. This provides the desired uniform central region with a diffuse surface. A simpler alternative is the harmonic oscillator potential:

$$V(\mathbf{r}) = \frac{1}{2}k\mathbf{r}^2 = \frac{1}{2}m\omega^2\mathbf{r}^2, \quad (1.5)$$

which provides a reasonable approximation to a real nuclear potential but is easy to handle mathematically. Both these potentials can be seen in Fig. 1.2.

Solving the Schrödinger equation with the harmonic oscillator potential leads to energy eigenvalues given by $E_{n,l} = (2n + l + \frac{1}{2})\hbar\omega$. From this we can see that states with $\Delta l = -2\Delta n$ (where $\Delta l = l_2 - l_1$ and $\Delta n = n_2 - n_1$) will be degenerate in energy. For a given orbital angular momentum l , coupled to the spin angular momentum vector s , we have total angular momentum $j = l \pm s$, hence can have $2j + 1$ m_j sub-states. The Pauli exclusion principle restricts the maximum number of nucleons in a given level which results in a basic shell structure with magic numbers at 2, 8, 20, 40, 70 and



Figure 1.2: Comparison of the general form of Woods-Saxon and harmonic oscillator potentials. The Woods-Saxon is a realistic potential with a uniform central region and a diffuse surface. The harmonic oscillator is a reasonable approximation to this.

112. This fails to reproduce all the known experimental magic numbers (2, 8, 20, 28, 50, 82 and 126) hence, other forces must be considered.

One such consideration is the addition of a term in l^2 which increases the binding energy for nucleons with larger angular momentum. Such a term has the desirable effect of increasing the potential at larger radii, whilst flattening it in the nuclear interior, producing a potential more like that of the Woods-Saxon. This lifts the $\Delta l = -2\Delta n$ degeneracy by increasing the binding for higher angular momentum nucleons but a further interaction is required in order to reproduce the experimentally observed magic numbers.

1.2.2 Spin-orbit splitting

This issue was finally solved both by Goeppert-Mayer, and independently by Haxel, Jensen and Suess, for which the Nobel Prize for Physics was awarded in 1963. The introduction of an interaction between the spin and orbital angular momentum of a nucleon, such that parallel alignments are favoured (i.e. $V_{\mathbf{l}\cdot\mathbf{s}} = -V_{ls}(\mathbf{r})\mathbf{l}\cdot\mathbf{s}$), results in the lowering in energy of a state with $j = l + s$ while the $j = l - s$ state is raised. This interaction now reproduces all experimental magic numbers on or near the line of stability.

The observation (and explanation) of these magic numbers is perhaps the single most significant development of nuclear structure as a huge amount of physics stems directly from it. The shell structure of nuclei explains the spins and parities of the ground states of many nuclei as well as some excited states, while the shell closures explain much about binding energies and separation energies. The excited states of a nucleus with one nucleon outside a closed shell will be dominated by the orbital which that nucleon occupies, whilst the ‘core’ can essentially be ignored. This idea can be extended to nuclei with several nucleons (or nucleon holes) outside a closed shell, such that only the interactions of these valence nucleons are important. However, in order to predict the energies of these states we must now consider the residual interactions introduced earlier.

1.2.3 The residual interaction

The residual interaction is essentially everything which is left after the mean-field central potential has been subtracted from the real Hamiltonian, i.e. this accounts for individual nucleon-nucleon interactions. This term is quantified through two-body matrix elements which can be obtained from nucleon-nucleon scattering experiments. However, for a many body system these interactions very quickly become too complex to handle, so a reduced model space must be defined and the Hamiltonian transformed into an effective one applicable to this reduced space. This can be achieved via three methods:-

Realistic — a realistic interaction is used (i.e. one consistent with two and three nucleon systems) in the full model space to obtain an effective interaction in a truncated model space.

Effective — theoretical energy eigenvalues are fitted to experimental data to obtain two-body matrix elements directly, without calculating the interaction itself.

Schematic — use a general form of the two-body potential and fit a small number of parameters to obtain good agreement between calculated energy eigenvalues and experimental data.

We now have all the basic ingredients for solving the nuclear many-body problem, i.e. the shell model. The basic process is to separate out the many-body Hamiltonian into a one-body Hamiltonian with a mean field and a correction Hamiltonian describing the residual interactions, construct the basis and compute the many-body Hamiltonian

matrix elements. We then construct the Hamiltonian energy matrix and solve for the lowest energy eigenvalues and corresponding eigenvectors.

Though it is somewhat beyond the scope of the present work, it is worth pointing out that nuclei with a large number of valence nucleons that reside in the mid-shell regions frequently exhibit behaviour consistent with a deformed, rather than spherical shape and collective excitations. The inclusion of residual interactions with a sufficiently large model space can reproduce these experimental results and progress is being made to bridge the gulf between the shell model and collective models.

1.2.4 The $f_{7/2}$ shell

The above process can be applied to any region of the nuclear chart, with the caveat that a suitable model space truncation can be found to allow computation. The $1f_{7/2}$ shell occupies a unique place in the nuclear chart where a single sub-shell is well separated from all others, creating a region where only one orbital is dominant. Nuclei in this region ($40 < A < 56$) exhibit a wealth of different behaviour, from single-particle-like nature near the shell closures at N (or Z) = 20 and 28, to deformed collective excitations at the centre of the shell. All this behaviour can be well described by the shell model, the latter requiring inclusion of the upper fp orbitals (i.e. $2p_{3/2}$, $1f_{5/2}$ and $2p_{1/2}$) while the former can be reasonably approximated by a pure $\pi(f_{7/2})^{Z-20} \otimes \nu(f_{7/2})^{N-20}$ configuration. This unique phenomenon allows great insight into the structure of nuclei in this region through use of very simple models and is ideally suited to MED studies as Coulomb matrix elements can be reliably extracted due to the simple nature of the model space.

1.3 Isospin and mirror nuclei

So far, the interactions between protons and neutrons have been treated identically. This treatment is one of the principle tenets of nuclear physics and can be expressed more rigorously as the charge symmetry and charge independence of the nuclear force,

i.e.

$$V_{\pi\pi} = V_{\nu\nu} \quad (1.6)$$

$$V_{\pi\nu} = \frac{V_{\pi\pi} + V_{\nu\nu}}{2}. \quad (1.7)$$

Because of this symmetry it is convenient to define the *isospin* quantum number t , which treats protons and neutrons as two states of the same particle, the nucleon. Mathematically, this quantum number can be treated identically to angular momentum, hence the projection on the z -axis is $t_z = +\frac{1}{2}$ for neutrons and $t_z = -\frac{1}{2}$ for protons. We can now define the projection of the total isospin (T) of a nucleus as

$$T_z = \sum^A t_z = \frac{N - Z}{2}. \quad (1.8)$$

This formalism can greatly simplify the quantum mechanical treatment of the nucleus, however, charge symmetry would imply perfect degeneracy between the binding and excitation energies of mirror nuclei. This degeneracy is of course lifted by the Coulomb force which creates a long-range repulsive force felt only by protons. (Note that for mirror nuclei, only charge asymmetry is considered as there are the same number of np pairs in each member of the mirror pair, hence charge dependence cannot have an effect here.)

1.3.1 Mirror displacement energies

The Coulomb interaction between protons will manifest itself principally in the mirror displacement energies, i.e. the difference in binding energy of isobaric analogue states (here we limit ourselves to consideration of the ground states of mirror nuclei, however these arguments can be applied to any isobaric analogue states).

The Coulomb energy for a uniformly charged sphere is given by

$$E_C = \frac{3e^2 Z(Z-1)}{5R} \quad (1.9)$$

which can be expressed in terms of the isospin projection T_z , as

$$E_C = \frac{3e^2}{5R} \left[\frac{A}{4}(A-2) + (1-A)T_z + T_z^2 \right]. \quad (1.10)$$

Hence, assuming the nuclear radius is identical for isobaric analogue states, the isospin dependence of the Coulomb energy of a nucleus is apparent. This produces the main contribution to the MDE, albeit in a rather oversimplified form. Further corrections include the proton-neutron mass difference, contributions from the Pauli principle which acts to increase the separation between protons, and an electromagnetic spin-orbit term (this last effect turns out to be significant for mirror energy differences and is discussed further in Section 1.3.3). Precise calculations of these terms were carried out by Nolen and Schiffer [2] and compared to experimental energy differences, however a consistent underestimate of $\sim 7\%$ was found. This is the well known Nolen-Schiffer anomaly and has been cited as evidence for charge-symmetry breaking.

Other contributions to the binding energy differences have been considered which include Coulomb distortions of the wave function, isospin impurities in the core and intra-shell interactions. More recent calculations have explained charge-symmetry breaking in terms of meson exchange [13], which combined with detailed knowledge of neutron skins [14] has reduced the discrepancy between experimental and calculated energy differences to the level of ~ 100 keV, virtually eliminating the Nolen-Schiffer anomaly.

1.3.2 Mirror energy differences

The mirror energy difference of a mirror pair is defined as the difference in excitation energy of isobaric analogue states, i.e.

$$MED_J = E_{J, T_z=-T}^* - E_{J, T_z=+T}^*. \quad (1.11)$$

As this is measured relative to the ground state of each nucleus, the effects of the MDE are eliminated, however, a number of spin dependent contributions to the excitation energy exist which lift the degeneracy of the analogue states. As the Coulomb force is well understood this quantity has the potential to be a useful probe of nuclear structure, as well as a laboratory in which to investigate charge symmetry breaking. In order to do this we must first construct a theoretical framework from which we can understand the Coulomb contributions to MED.

1.3.3 Isospin breaking forces

The main contributions to MED have been derived by a number of authors from the study of many different mirror pairs. This work was compiled and formalised by Zuker *et al.* [8] and discussed in more detail by Bentley and Lenzi [11]. The main contributions are as follows.

The Coulomb multipole term

From a microscopic perspective, in order to generate excited states in nuclei, pairs of nucleons must recouple from their minimum energy coupling of $J = 0$ towards the maximum alignment allowed by the Pauli principle. However, the Pauli principle also dictates that this alignment of angular momentum vectors must produce a corresponding increase in the spatial separation of the pair of nucleons which, in the case of a proton pair, will lead to a reduction in the Coulomb energy between this pair. For a pair of neutrons, the same alignment effects take place, but with no corresponding change in Coulomb energy. This effect is nicely visualised in Fig. 1.3, a plot of the probability distribution for the separation of a pair of nucleons coupled to different angular momenta.

In order to incorporate this effect in the shell model framework, Coulomb matrix elements (CME) must be introduced which account for the changing Coulomb energy between a pair of protons coupled to different angular momenta. CME can be extracted via a variety of methods (as described by Williams *et al.* [10]), directly from the $A = 42$, $T_z = \pm 1$ mirror pair for example. In the following work, however, the methods used throughout reference [11] are used, i.e. the harmonic oscillator potential is used to calculate CME. This is done in order to prevent the inadvertent inclusion of other isospin-breaking phenomena, such as single particle effects (see later), which could be swept up in the $A = 42$ CME, preventing insight into the underlying nuclear physics when other mirror pairs are considered. A detailed description of the calculation of CME using the harmonic oscillator potential shall not be given here (more details can be found in [16]). In brief, CME may be calculated by expanding the Coulomb interaction between two protons as a series of Legendre polynomials, i.e.

$$V_C(r_{12}) = \frac{e^2}{r_{12}} = \frac{e^2}{\sqrt{r_1^2 + r_2^2 - 2r_1r_2 \cos \gamma}} = e^2 \sum_{k=0}^{\infty} \frac{r_{<}^k}{r_{>}^{k+1}} P_k(\cos \gamma) \quad (1.12)$$

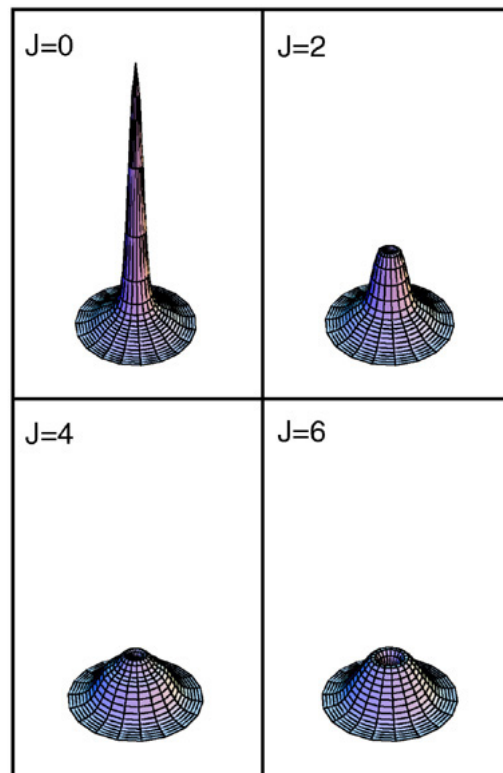


Figure 1.3: Calculation of the probability distribution for the separation of a pair of nucleons coupled to different angular momenta J . The centre of each plot corresponds to zero separation between the nucleons. Image taken from [11], from calculations carried out in [15]. (Original in colour.)

where $r_<$ and $r_>$ are the smaller and larger of r_1 and r_2 , γ is the angle between them, and k is the multipole order. An expression is then found for the CME, and separated into angular and radial components, the radial part is solved numerically using the harmonic oscillator potential. This produces values of 418 keV, 357 keV, 324 keV and 318 keV for the $J = 0, 2, 4$ and 6 , $f_{7/2}$ Coulomb matrix elements [16].

The monopole term — Radial effects

As alluded to in Section 1.3.1, the radii of the two members of a mirror pair may differ which, from equation (1.10), will lead to differences in the Coulomb energy. This contribution will of course be accounted for in the CDE, hence will not show up in MED. However, radial changes as a function of angular momentum, irrespective of whether the radii differ in each member of a mirror pair, will produce energy differences due to the different proton number.

Orbitals with different angular momentum l , have different mean radii, hence

changes in the occupation of orbitals will produce energy differences. In the $f_{7/2}$ shell, low-spin states tend to have considerable admixtures from the upper fp shell while, as the band termination is approached, states become more closely approximated by a pure $f_{7/2}$ configuration, particularly in the mid-shell region where deformation is driven by the partial occupation of upper fp orbitals. Furthermore, mirror symmetry arguments suggest that the total occupation numbers for each member of a mirror pair will be the same (albeit with exchanged values for protons and neutrons), hence it is the difference in charge between the two members of the mirror pair which produces the spin dependent energy difference.

The monopole term — Single-particle effects

In Section 1.2.2 the interaction between the orbital angular momentum of a nucleon (l), and its intrinsic spin (s) was discussed in reference to the strong nuclear force and used to explain the known magic numbers. A similar interaction exists for the electromagnetic force, i.e. electromagnetic spin-orbit interaction (EMSO), as mentioned in Section 1.3.1. Due to the relatively weak nature of the electromagnetic force in comparison to the strong force (the EMSO interaction is typically 1% of its nuclear analogue), it is often ignored, however, there are circumstances where it becomes significant.

The general expression for the EMSO potential is

$$V_{Cts} = (g_s - g_l) \frac{1}{2m_N^2 c^2} \left(\frac{1}{r} \frac{dV_C}{dr} \right) \vec{l} \cdot \vec{s} \quad (1.13)$$

where g_s and g_l are the gyromagnetic factors and m_N is the nucleon mass. Nolen and Schiffer [2] used this to estimate the contribution of this interaction to MDE by assuming the Coulomb potential V_C , is provided by a uniform charged sphere, hence

$$E_{Cts} \simeq (g_s - g_l) \frac{1}{2m_N^2 c^2} \left(\frac{-Ze^2}{R_C^3} \right) \langle \vec{l} \cdot \vec{s} \rangle \quad (1.14)$$

where $\langle \vec{l} \cdot \vec{s} \rangle = l/2$ or $-(l+1)/2$ for $j = l + s$ and $j = l - s$ respectively. When we consider the sign of the gyromagnetic factors ($g_s^\pi = 5.586$, $g_l^\pi = 1$, $g_s^\nu = -3.828$, and $g_l^\nu = 0$) we see that the single-particle energies of proton levels will sink relative to the neutrons, producing a contribution to the MDE. Furthermore, if we consider a single particle excitation from an orbital with $j = l + s$, to one with $j = l - s$, if the excitation

occurs for a proton in one member of a mirror pair and a neutron in the other, this will produce a considerable energy difference, contributing to the MED of the excited state.

A further effect, which again is analogous to one mentioned in Section 1.2.1 is the inclusion of a term proportional to l^2 . This contribution to the single-particle splitting of a proton in a shell with principle quantum number n , and is given in Duflo and Zuker [14] as

$$E_{Cu} = \frac{-4.5Z_{cs}^{13/12} [2l(l+1) - n(n+3)]}{A^{1/3}(n+3/2)} \quad (1.15)$$

where Z_{cs} is the proton number of the core.

Nuclear isospin-breaking terms

As has been discussed, non-Coulomb charge-symmetry breaking effects have long been known through their contribution to mirror displacement energies. These effects will not show up in MED studies due to the measurement of energies relative to the ground state, only an angular-momentum dependent CSB term would be visible.

As mentioned earlier, Coulomb matrix elements can be extracted directly from the $A = 42$, $T_z = \pm 1$ mirror pair. If we assume that these nuclei can be described by a pure $(f_{7/2})^2$ configuration on top of an inert ^{40}Ca core, the MED of this mirror pair should be dominated by the Coulomb multipole term produced by coupling the valence nucleons to different spins. The MED should, therefore, be a reasonable approximation to the CME. These values are plotted in Fig. 1.4, along with the harmonic oscillator CME quoted earlier (with the $J = 0$ state normalised to zero). From this figure it is immediately clear that this simple interpretation is incorrect. Not only does the $A = 42$ MED not follow the harmonic oscillator CME, the increase at $J = 2$ is at odds with the discussion of the Coulomb multipole term presented earlier, i.e. that Coulomb energy must reduce as a pair of protons are re-coupled to larger spins. This phenomenon is often referred to as the ‘ $J = 2$ anomaly.’

One notable consideration is that the pure $(f_{7/2})^2$ configuration may not be suitable. Indeed the low-lying states are known to have significant contributions from core excitations (though considering the average of the two lowest lying $J^\pi = 2^+$ states yields much the same picture [9]). However, if we consider the $A = 54$, $T_z = \pm 1$ mirror pair, (plotting $-MED$, as the $(f_{7/2})^{-2}$ configuration will lead to active proton-holes in ^{54}Fe ,

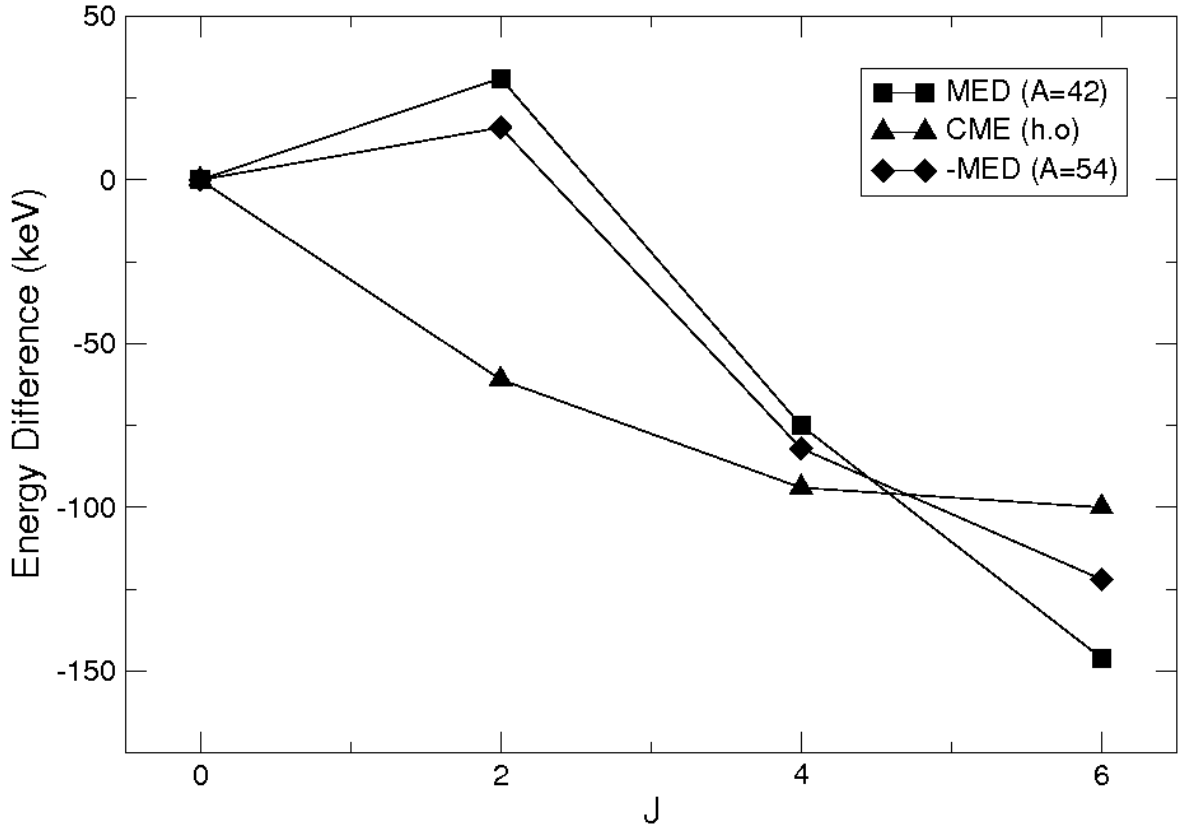


Figure 1.4: Mirror energy differences for the $A = 42$ mirror pair, compared to harmonic oscillator CME (with the ground state normalised to zero) and the $A = 54$ mirror pair (plotted as $-MED$ as the $(f_{7/2})^{-2}$ configuration will lead to active proton-holes in ^{54}Fe , rather than ^{54}Ni). Note the discrepancy between the general downward trend of the CME, compared to the increase at $J = 2$ for the MED.

rather than ^{54}Ni) we see a similar trend (see Fig. 1.4) [9]. Though the $A = 56$ shell closure is known to be poor, it seems unlikely that core excitations from the sd shell in the case of the $A = 42$ pair, will produce the same effects on the MED as excitations to the upper fp for the $A = 54$ pair. We must therefore conclude that this is a result of a spin-dependent, charge-symmetry breaking component to the nuclear force.

Following on from this, we can obtain a measure of the CSB nuclear term by subtracting the Coulomb contributions from the $A = 42$ MED, i.e.

$$MED_{J, A=42, T=1} = E_{J, 42\text{Ti}}^* - E_{J, 42\text{Ca}}^* = V_C(J) + V_B(J) \quad (1.16)$$

where V_C accounts for all Coulomb terms and V_B represents any nuclear CSB terms. If, for simplicity, we assume that V_C is simply the contributions from the Coulomb multipole term (V_{CM}) we obtain the values in Table 1.1.

It is clear from this table that the contributions to MED from isospin-breaking

Table 1.1: Coulomb (V_C) and nuclear (V_B) isospin breaking two-body matrix elements in the $f_{7/2}$ shell, in keV. CME are calculated with the harmonic oscillator potential, taken from reference [16]. Nuclear matrix elements are extracted from the $A = 42$ and 54 MED. In each case, following the methodology of Zuker *et al.* [8], the centroids, $V_{centr} = \frac{\sum_J[V(2J+1)]}{\sum_J(2J+1)}$ have been subtracted in order to aid comparison. Though the values for V_B are derived from experimental values, no uncertainties are quoted here as these are intended as indicative values rather than genuine measurements of matrix elements.

	$J = 0$	$J = 2$	$J = 4$	$J = 6$
$V_C = V_{f_{7/2}}^{ho}$	87.54	26.54	-6.46	-12.46
$V_B(A = 42) = \text{MED}(A = 42) - V_C$	-1.18	90.82	17.82	-47.18
$V_B(A = 54) = -\text{MED}(A = 54) - V_C$	-7.39	66.48	-0.40	-61.81
$V_B(\text{average})$	-4.29	78.65	8.71	-54.49

nuclear forces are as significant as Coulomb contributions, hence must be included in shell-model calculations if good agreement between experiment and theory is to be achieved. Such calculations have been carried out across the $f_{7/2}$ shell (see Section 6.2 for details on performing such calculations) and excellent agreement between experimental and calculated MED has been achieved [8]. Similar calculations and experimental results are discussed in the review by Bentley and Lenzi [11].

Chapter 2

Gamma-ray spectroscopy at the microbarn level

Over the last few decades, fusion-evaporation reactions have been a staple of gamma-ray spectroscopy. These reactions have allowed the observation of excited states up to high-spin right across the nuclear chart leading to a wealth of new physics such as vibrational and rotational excitations, super-deformed bands and shape coexistence, to name but a few. More recently these reactions, combined with the development of large, high-efficiency high-resolution Compton-suppressed Ge arrays and efficient methods of reaction channel selection, have allowed unprecedented access to high-spin states in exotic nuclei, particularly those neutron deficient, at or beyond the $N = Z$ line. These proton-rich nuclei are extremely difficult to produce and study, hence require devices with the utmost sensitivity and selectivity. They are, however, the very nuclei needed for the study of isobaric analogue states.

The following chapter reports on attempts to perform γ -ray spectroscopy on $T_z = -\frac{3}{2}$ nucleus ^{49}Fe , using fusion-evaporation reactions. This experiment employed a standard Gammasphere-FMA set-up, however, novel analysis techniques are developed in order to achieve spectroscopy at the microbarn level.

2.1 Fusion-evaporation reactions

Fusion-evaporation reactions are indirect reactions which can be initiated when a beam of nucleons with modest energy (typically a few MeV per nucleon) impinge on a target nucleus. If the centre-of-mass energy is above the Coulomb barrier, these two nuclei

may fuse to form a compound system which stays together long enough to share its excitation energy amongst its constituent nucleons. If any individual nucleon (or group of nucleons) acquires sufficient energy, the nucleus will eject these particles allowing it to rapidly lose energy, analogous to evaporative cooling of a liquid. The isotopes which the compound system decays into (i.e. the residues) are statistically distributed and depend only on the excitation energy of the compound nucleus with no *memory* of the combination of beam and target which produced it. A specific compound nucleus could be made from any number of beam/target combinations, thus the most appropriate reaction can be selected based on practicalities such as the availability of intense beams or the chemical stability of the target. Furthermore, the particle evaporation stage produces a variety of isotopes from one beam/target combination, allowing a number of isotopes to be produced in one experiment.

Though the evaporation of particles is an effective method of de-excitation, in heavy-ion fusion-evaporation reactions, a great deal of angular momentum can be generated in the compound nucleus which is not effectively removed through particle emission. This means—following particle emission—the residue is left in a high-spin state, thus must decay to the ground state via a cascade of gamma rays (though nuclei with excessive angular momentum may undergo fission). Detection of this cascade allows a wealth of information to be gathered on the evolution of nuclear structure with angular momentum. Furthermore, the use of fusion-evaporation reactions has been so prolific as they allow access to many isotopes a reasonable way from stability using stable beams and targets. Experiments using direct reactions with stable beams, however, are limited to nuclei nearer stability.

2.2 Experimental detail

An experiment was carried out in an attempt to observe gamma decays from excited states of the $T_z = -\frac{3}{2}$ nucleus ^{49}Fe . As the natural-parity *yrast* states (lowest energy state of a given spin) of ^{49}V are already well known [17], this would allow the first observation of $T = \frac{3}{2}$ isobaric analogue states above $A = 33$ [18]. The nucleus of interest was to be populated via a fusion-evaporation reaction utilising a ^{40}Ca beam supplied by the ATLAS accelerator of Argonne National Laboratory impinging on a ^{12}C target. The effective target thickness was $679 \mu\text{g}/\text{cm}^2$ ($601 \mu\text{g}/\text{cm}^2$ at an angle of

27.75° to the beam line) and the beam energy was 231.5 MeV. Reaction residues were identified with the Fragment Mass Analyzer (Section 2.2.1) and correlated with γ rays observed with the Gammasphere array (Section 2.2.2).

The beam energy was chosen based on the work of Cerny *et al.* [19], who measured a cross section of $\sim 0.5 \mu\text{b}$ for the reverse reaction at a beam energy of 65 MeV. The 231.5 MeV ^{40}Ca beam produced a centre-of-mass energy ~ 3 MeV higher than that used by Cerny, allowing population of the first few excited states of ^{49}Fe , and was predicted to yield a slightly higher cross section of $\sim 1.5 \mu\text{b}$. Furthermore, a short test run had been performed in 2004 to assess the feasibility of this experiment. This test utilised the Fragment Mass Analyser for identification of nuclei and a single clover γ -ray detector. In 10 hours of beam time, the detection of approximately 3000 ^{49}Fe recoils was reported and the $1.5 \mu\text{b}$ cross section estimate was confirmed [20].

2.2.1 The Fragment Mass Analyzer

As mentioned at the beginning of the chapter, the ability to efficiently select the channel of interest from the multitude of possible decays of the compound nucleus is crucial when performing γ -ray spectroscopy on weakly populated isotopes. This can be achieved by the detection of the evaporated particles, hence inferring what the reaction product was. When studying proton-rich nuclei it is inevitable that neutrons must be evaporated in order to produce the nuclei of interest. Neutrons are extremely difficult to detect efficiently, therefore, it is often prudent to detect the residue directly. This can be achieved by choosing a reaction in inverse kinematics, hence the compound system is formed with considerable linear momentum. The forward focused residues are passed into a spectrometer where they can be separated from unreacted beam and identified.

At Argonne National Laboratory this task is performed by the Fragment Mass Analyzer (FMA) [21]. The FMA is a triple-focussing recoil mass spectrometer utilising a combination of one magnetic and two electric dipoles, along with two focussing magnetic quadrupole doublets. These units (arrange as shown in Fig. 2.1) first separate out the unreacted beam (usually dumping it onto the anode of the first electric dipole), then disperses the reaction products in A/Q so they can be identified by a suite of detectors at the focal plane. In this experiment the FMA was optimised for $A = 49$ residues with charge state $Q = 19$. Slits located after the final quadrupole were used

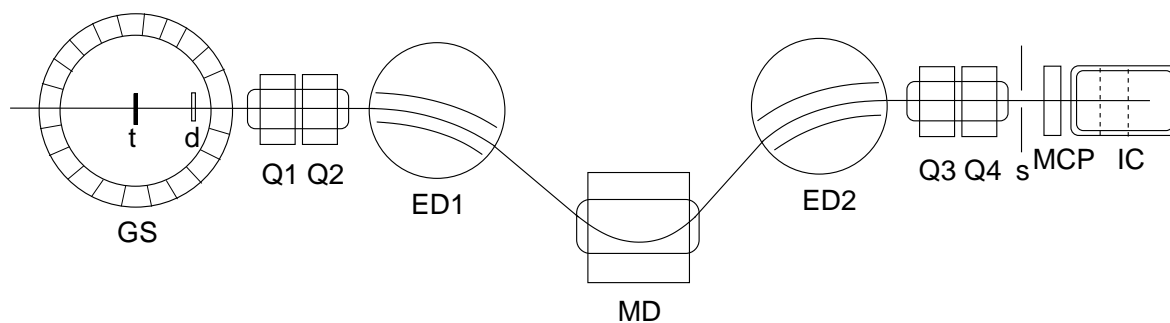


Figure 2.1: Schematic diagram of the elements of the FMA, showing the quadrupole doublets (Q1-4), electric dipoles (ED1/2) and magnetic dipole (MD). The target (t) and degrader foil (d) are shown, along with the Gammasphere array (GS). The slits (s) and focal plane detectors—ion chamber (IC) and micro-channel plate (MCP)—can also be seen after Q4.

to remove other A/Q values.

Due to the maximum voltage attainable by the electric dipoles of the FMA (500 kV), the beam-like residues had to be slowed by a natural Ti degrader foil, 1.248 mg/cm² thick, placed ~ 0.4 m after the target. This reduced the energy of the beam entering the FMA to a manageable ~ 124 MeV.

Focal plane detectors

Several detectors are placed at the focal plane of the FMA to facilitate identification of the reaction products once they have been dispersed. These consist of a micro-channel plate detector (MCP) [22] and an ionisation chamber. The ionisation chamber is a split anode device filled with isobutane and used to measure the energy of the residue at the focal plane of the FMA. The gas pressure was chosen such that residues of interest were completely stopped within the third segment of the chamber allowing determination of atomic number via $\Delta E-E$ techniques (see Section 2.3.2).

The MCP, a schematic of which can be seen in Fig. 2.2, consists of a thin foil placed perpendicular to the path of the reaction products, which emits electrons when ions pass through it. These are accelerated towards a wire plane before a further wire plane deflects them through 90° onto the channel-plate electron multipliers. The resultant electrons are collected on a resistive anode with electrodes at the four corners. Position sensitivity is achieved through calculation of the collected charge ratios, allowing A/Q to be determined. Furthermore, this device provides a timing signal for residues reaching the focal plane which is used in the trigger as well as other timing measurements (see Section 2.3).

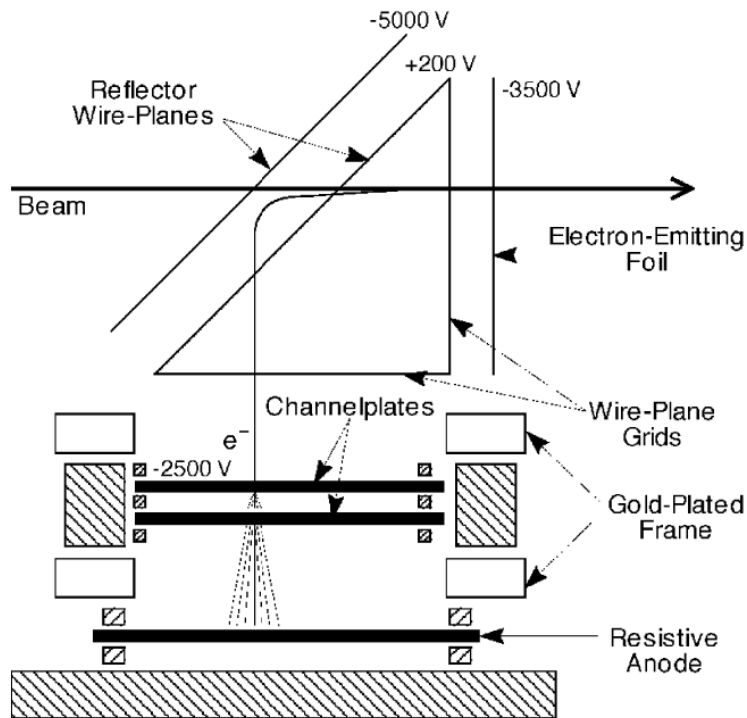


Figure 2.2: Schematic diagram of the Argonne micro-channel plate detector, taken from [22].

2.2.2 The Gammasphere array

Gammasphere [23, 24] is an array of up to 110 Compton-suppressed, high-purity Ge detectors. These are arranged in an icosahedron shape with 17 rings of detectors surrounding the target position at the entrance to the FMA, producing a coverage approaching 4π . The Compton suppression is provided by BGO elements between and behind each Ge crystal to veto γ rays which scatter in or out of the crystal without depositing their full energy. During this experiment, the forward-most detector ring had to be removed in order to accommodate the first quadrupole of the FMA. Furthermore, the second and third rings were deactivated as, due to γ rays produced in the degrader foil, the rate in these detectors was too high leading to excessive dead-time. Several further detectors were absent for repairs leaving a total of 93 detectors.

The detectors in rings closest to 90° (where Doppler broadening is greatest) are electronically segmented. These detectors have an outer contact split into two D-shaped elements, see Fig. 2.3. Calculation of the ratio of energy collected in one of these side-channels to the high-resolution signal from the central contact, i.e. $R_{seg.} = E_{side}/E_{cent.}$, provides a measure of where the γ -ray hit the crystal so can be used to reduce the effects of Doppler broadening beyond the limit set by the solid angle of the detector

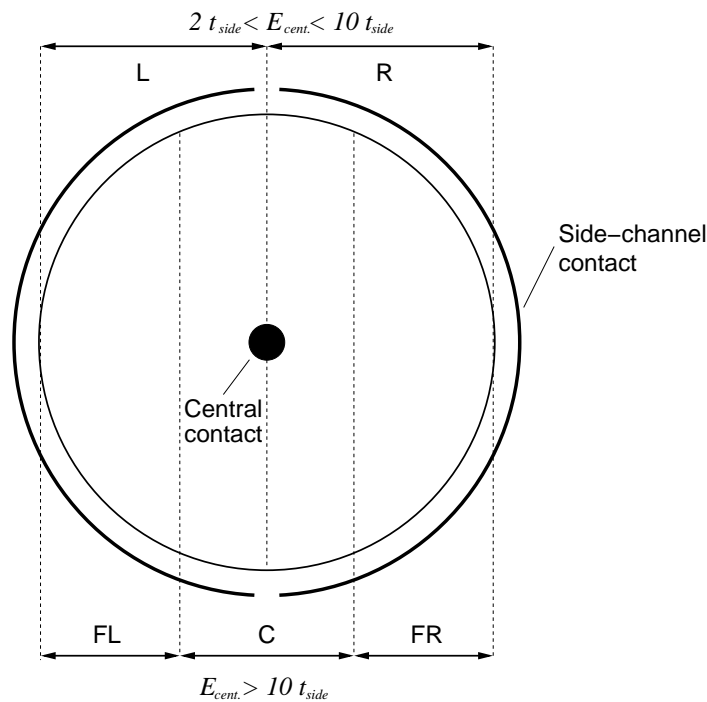


Figure 2.3: Schematic diagram showing the segmentation of the Gammasphere crystals. The different hit regions described in the text are indicated.

(see Section 2.3.2).

As this was a very low cross-section experiment (relative to the total reaction cross section of approximately 1 barn), clean identification of the exit channel was critical. Accordingly, data acquisition was triggered by the detection of an ion at the focal plane of the FMA (determined by the MCP), in coincidence with the detection of one or more γ rays in Gammasphere. In experiments such as these, a second trigger condition is often provided by a high-fold γ ray detection event with no requirement on the detection of an ion in the FMA, thus allowing high-fold γ -ray coincidence analysis to be performed. In this case, no excited states were known in the nucleus of interest, hence every observed γ ray must be correlated with a residue at the focal plane. Therefore, in order to minimise dead-time, such a secondary trigger condition was not utilised.

2.3 Data Analysis

In total, approximately 150 hours of data were taken, however, later analysis revealed that a problem had occurred with the data acquisition system (DAQ) causing some data to be lost. It is believed that the origin of the problem was that the time required to write out the full data stream following an event was sometimes greater than that

allowed by the DAQ. This resulted in some of the data from virtual station 25 (the last station to write its data to tape) not being written out for some events. This station holds the data from the FMA data stream, i.e. the ionisation chamber signals and two timing signals:

RFPR — a *TAC* started by the *RF* (a signal generated by the accelerator) and stopped by the trigger,

RFTAC — a *TAC* started by the MCP and stopped by a delayed *RF* signal.

The last data word within this stream is the *RFTAC* signal so this is missing from $\sim 50\%$ of the events recorded. In some cases, earlier data was also not written out, e.g. the ion chamber information.

The absence of this data was a severe loss as the *RFTAC* is used to calculate the Et^2 parameter (see Section 2.3.2) which is crucial for the identification of ^{49}Fe recoils. As such, half of the data was made unusable, reducing the data taken to an effective 75 hours.

The off-line data analysis was split into two stages, a compression stage and an analysis stage.

2.3.1 Data compression

An initial compression stage was utilised to remove redundant information within the data and to perform some basic manipulation of some parameters. The first such calculation determined the position of ions detected at the focal plane of the FMA. This was achieved through manipulation of the signals from the four corners of the MCP, which were summed in hardware to produce a signal from either side (in the dispersive direction) of the detector, q_1 and q_2 . The position in the dispersive plane (x) is then calculated as

$$x = \frac{q_2 - q_1}{q_2 + q_1}. \quad (2.1)$$

A number of correction factors were also applied to various parameters (such as the ion chamber signals and timing signals) to account for gain drift during the experiment. Both the high-resolution and side-channel data from each Ge detector were gain matched to 1 keV per channel. Any Ge signals in which pileup occurred or the γ -ray energy recorded was zero were labelled as invalid and events with no valid Ge signals were discarded, as were events in which part of the data stream had been lost.

The *RFPR* signal was subtracted from the individual *getime* signals (a *TAC* started by an individual Ge signal and stopped by the trigger) to produce a *TAC* effectively started by an individual Ge signal and stopped by the *RF* signal from the accelerator (referred to as *RFGE* from now on). This *TAC* has the best possible resolution, hence gating on this (carried out in the post-compression stage) can greatly reduce the number of random γ -recoil coincidences. This value was output with the high resolution Ge energy in place of the *getime* word.

Finally, a segmentation routine was carried out on the 65 segmented detectors in order to reduce the effects of Doppler broadening. The degree to which the detector can be split up into different regions depends on the energy detected by the central contact and the threshold energy of the side channel (t_{side}). The threshold sets the minimum energy needed for a signal to be recorded and has to be set considerably higher for the side channel than the central contact as noise is a more significant issue. For high-energy γ rays, the detectors can be divided into three regions, labelled far-left, far-right or centre hits. Medium energy γ rays are split into two regions, left and right, while low energy γ rays are considered to have hit the centre of the detector. The details of these distinctions are tabulated in Table 2.1. Once the necessary calculations and groupings have been made it is only necessary to output a binary signal to tag where each γ ray hit the detector. This is output in place of the highest-energy bits and pileup bits of the γ -ray data, again minimising data storage requirements.

The above processes removed significant amounts of redundant data, reducing further data sorting times for the following stage where the bulk of the analysis is performed.

2.3.2 Production of clean γ -ray spectra

Z selection

Critical to the success of this experiment was the clean identification of the residues of interest, and their associated γ rays. This requires good selection of both *A* and *Z*. *Z* selection was achieved through use of ΔE -*E* methods using the three signals collected in the ionisation chamber at the focal plane of the FMA. This chamber has its anode split into three, effectively producing two thin detection regions (ΔE_1 and ΔE_2) and a thick one (ΔE_3) in which all of the nuclei of interest were stopped. Three ΔE -*E*

Table 2.1: Table summarising the segmentation routine carried out in order to minimise Doppler broadening. The ratio of energies detected in the side channel and central contacts is used, i.e. $R_{seg.} = E_{side}/E_{cent.}$.

Energy Range	Energy Ratio	Region Hit	Angular offset ($^{\circ}$)
$E_{cent.} > 10t_{side}$			
	$R_{seg.} > 0.9$	FR	+2.9
	$0.9 > R_{seg.} > 0.1$	C	0
	$R_{seg.} < 0.1$	FL	-2.9
$10t_{side} > E_{cent.} > 2t_{side}$			
	$R_{seg.} > 0.5$	R	+2.4
	$R_{seg.} < 0.5$	L	-2.4
$E_{cent.} < 2t_{side}$			
		C	0

matrices were produced from these signals, i.e. ΔE_1 vs. E , ΔE_2 vs. E and ΔE_{12} vs. E (where $E = (\Delta E_1 + \Delta E_2 + \Delta E_3)/3$ and $\Delta E_{12} = (\Delta E_1 + \Delta E_2)/2$). As a result of the high beam-energy, these three matrices all display good separation (as can be seen in Fig. 2.4) but in order to achieve optimal Z selection with minimal overlap from neighbouring isotopes, cuts were applied to all three matrices. The effect of this technique can be seen in Fig. 2.5 which compares the γ -ray spectrum produced by selecting the Fe region of the three matrices, with one using only the ΔE_{12} vs. E matrix. The former technique reduces statistics overall but produces a greater reduction in γ rays from nearby isotopes (i.e. Mn and Cr). The ratio of γ rays from other strongly populated isotopes (such as V) to Fe γ rays remains unchanged, indicating that these are present as a result of random coincidences rather than genuine overlap of the regions in Fig. 2.4.

Mass selection — Et^2

Unusually in this experiment, Z selection was not sufficient to obtain a clean γ -ray spectrum for ^{49}Fe . Though the FMA disperses reaction products in A/Q and has slits at the focal plane to select the $A = 49$ residues, the presence of charge-state ambiguities will allow other Fe isotopes to be transmitted to the focal plane, e.g. ^{52}Fe in charge state $Q = 21$. Due to the extremely low cross section for ^{49}Fe , the intensity

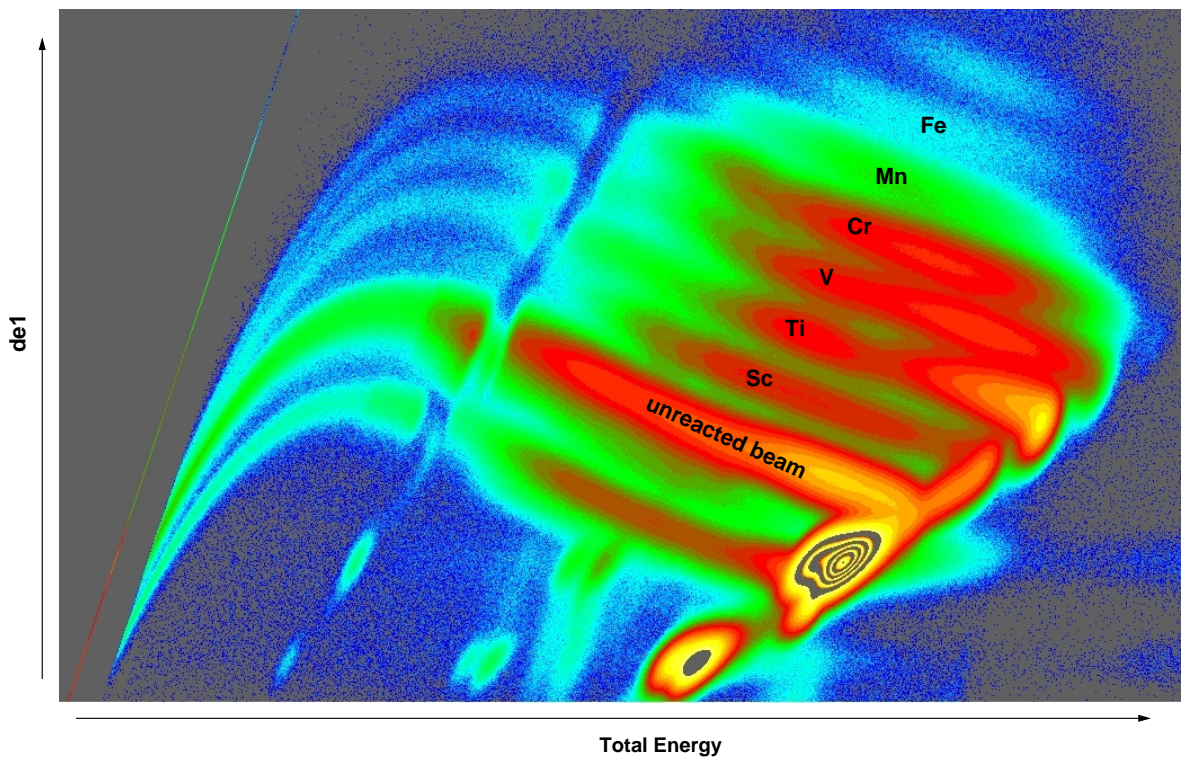


Figure 2.4: Example $\Delta E-E$ matrix used for identification of Z . E is on the x -axis and ΔE_1 on the y -axis. Each downward slanting distribution corresponds to residues of a different atomic number. (Original in colour.)

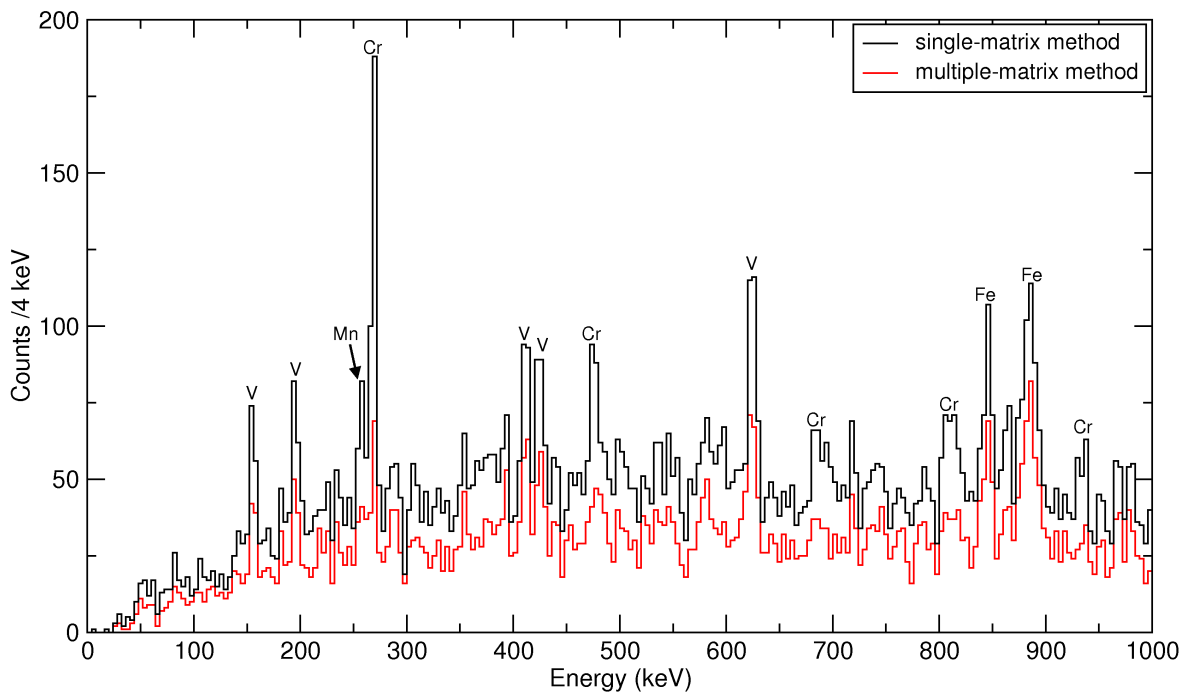


Figure 2.5: Gamma-ray spectra produced in coincidence with Fe residues using three different $\Delta E-E$ matrices, see text for details. The multiple-matrix technique significantly reduces statistics but improves the ratio of Fe to nearby isotopes (^{49}Cr and ^{49}Mn). γ rays from other strongly populated isotopes such as V, present due to random coincides, remain in approximately the same proportion. (Original in colour.)

of these transmitted contaminants will overwhelm the isotopes of interest, despite in many instances, being produced in reactions with oxygen contamination on the target. The FMA did generate some dispersion of the charge-state ambiguities which could be measured with the MCP, however, as can be seen in Fig. 2.6, this was insufficient to allow clean mass selection.

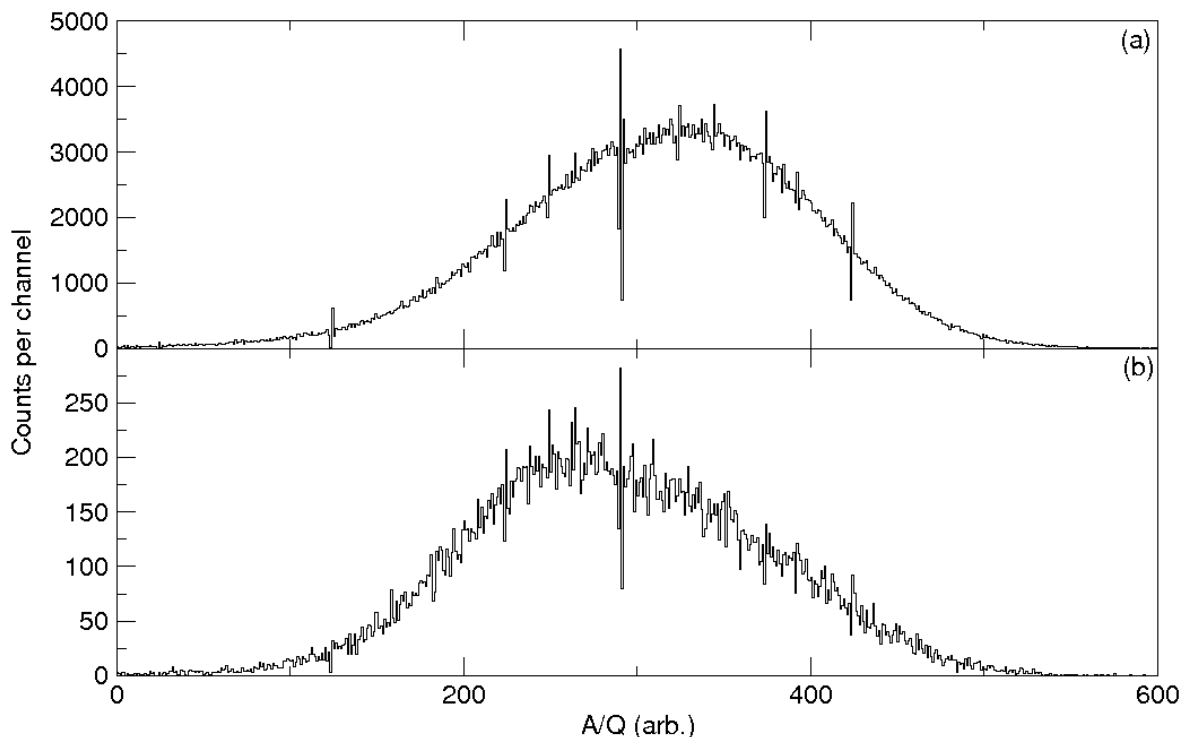


Figure 2.6: Plots of A/Q , as measured with the MCP for (a) Cr isotopes, dominated by ^{49}Cr , and (b) Mn isotopes, composed of slightly more ^{52}Mn than ^{49}Mn . Differences between the distributions are apparent but with insufficient dispersion for effective mass selection.

In order to overcome this, an Et^2 method was employed similar to that described in ref. [25]. This is based on the simple kinematic assumption that the mass of a recoiling nucleus is proportional to the product of its kinetic energy and the square of its time-of-flight (tof). The tof was determined from the $RFTAC$ signal. As this TAC was started by the channel plate and stopped by the delayed RF signal, it had to be reversed (started by RF , stopped by channel plate) and calibrated to 1 ns per channel using the known 82 ns periodicity of the accelerator and calculations of the expected time-of-flight. In previous experiments, calculations of the energy relied on applying arbitrary corrections to the energy detected in the ionisation chamber to compensate for the energy lost in the thin entrance window and the micro-channel plate. The value for this was determined via an iterative process until the centroids of the Et^2 peaks of

known isotopes (identified from γ ray analysis) of the same mass lined up in the same channel. In this case however, the technique was found to be unsuitable, probably due to the presence of the degrader foil which induced a much greater energy loss.

A new method was developed as part of this thesis work in collaboration with Paul Kent, a fellow PhD student at York [26], to calibrate the energy signal exactly and compensate for losses. This was achieved through consideration of the Cr region of the $\Delta E-E$ matrix. This was chosen because it was a very intense reaction channel with only a single Cr isotope (^{49}Cr) delivered to the focal plane (to a reasonable approximation). The *tof* signal for Cr (calibrated as above) was plotted versus $E^{-1/2}$. This should produce a straight line that passes through the origin, with the gradient equal to $s\sqrt{A/2}$, where s is the path length and A is the mass of the nucleus. By measuring the gradient and intercept, a correction factor and offset were calculated to *map* the line to the desired values. We now have fully calibrated energy and time measurements so the mass of the residue can be calculated exactly as:

$$A = 2E \left(\frac{t}{s} \right)^2. \quad (2.2)$$

This calibration was carried out solely using ^{49}Cr , hence did not work perfectly for other isotopes. For V isotopes for example, good mass separation was achieved but the three isotope peaks (identified from known γ rays as ^{47}V , ^{48}V and ^{49}V) were not in the expected channels. It was found that this issue could be resolved by incrementally adding (or subtracting) a constant to the energy of residues with Z lower (or higher) than that of Cr. These offsets have been reproduced with simulations of energy losses in the degrader foil and ionisation chamber window [26]. The downside to this method is the explicit Z dependence of the Et^2 calculation, i.e. adding an energy offset dependent on Z which is itself determined through measurements of energy. Nevertheless, this new method yields a resolution of ~ 2.5 amu, a considerable improvement over previous methods. An example of this can be seen in Fig. 2.7.

Furthermore, creating a matrix of A (calculated using the above method) versus x (position at the focal plane) as seen in Fig. 2.8, essentially allowed the plotting of variables proportional to mass on two independent axes, thus yielding far better discrimination between neighbouring masses. This was particularly useful in this experiment as it allowed the creation of complex shaped polygonal software gates that

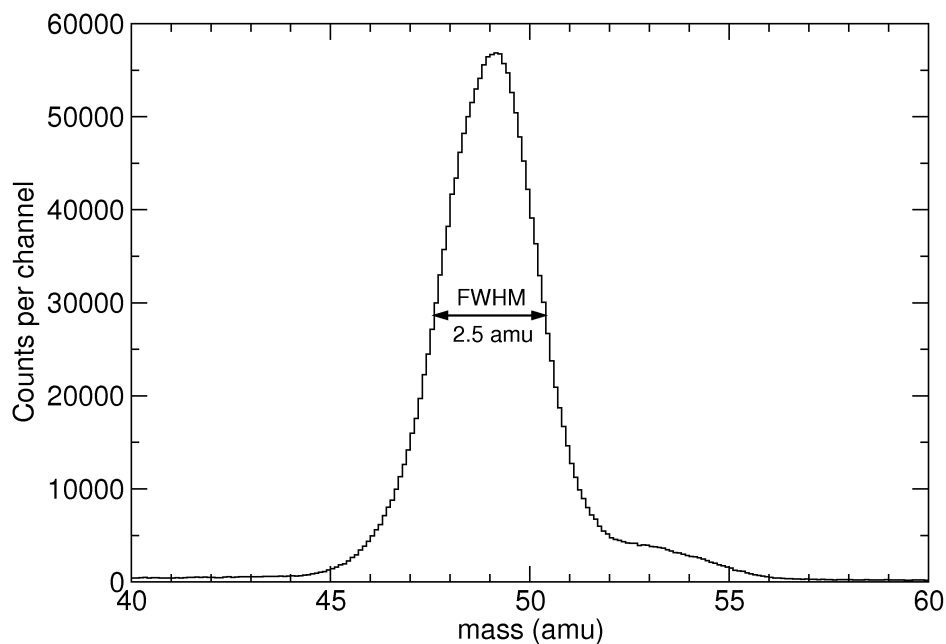


Figure 2.7: Mass spectrum for Cr isotopes, produced using the Et^2 technique (see text for details). The single peak corresponds to ^{49}Cr —the only Cr isotope produced in this experiment—and demonstrates the ~ 2.5 amu resolution achievable with this technique.

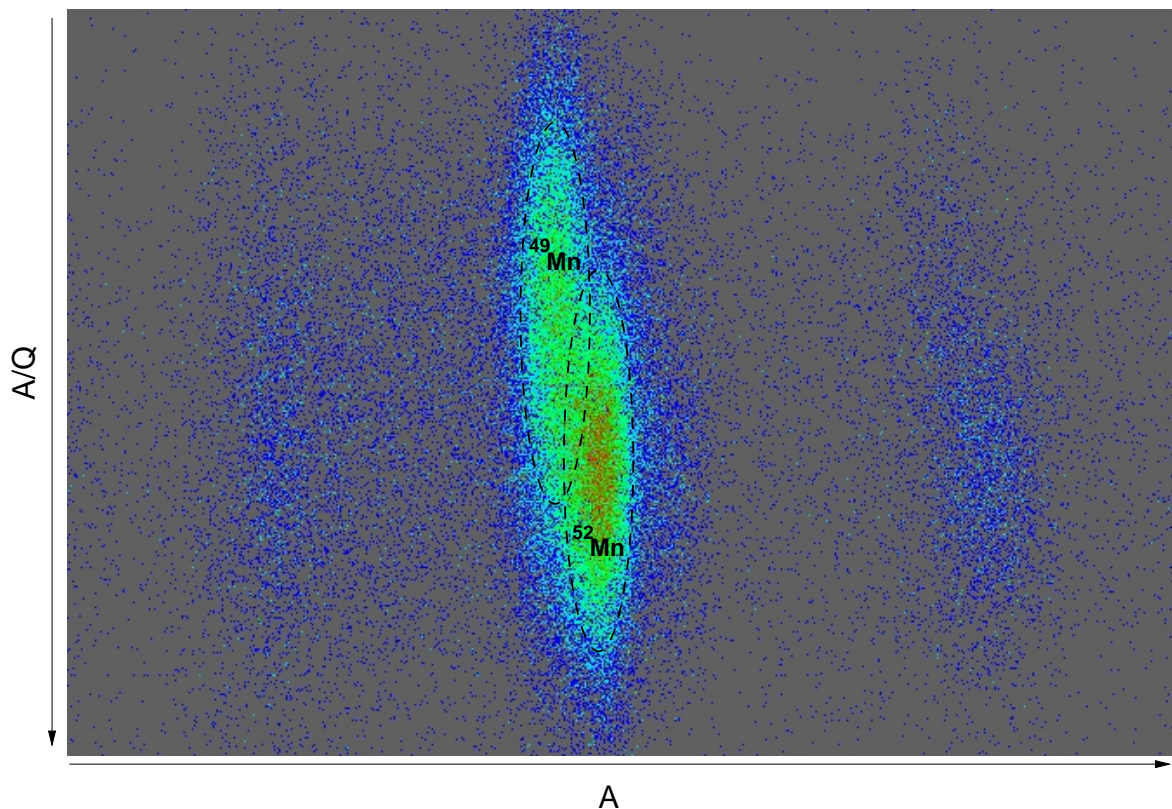


Figure 2.8: A vs. A/Q plot gated on $Z = 25$ residues. A is derived from measurements of Et^2 and A/Q from the MCP. The two overlapping but discernible regions correspond to ^{49}Mn and ^{52}Mn . Polygonal gates can be applied to plots such as these to uniquely select the nucleus of interest without inclusion of any neighbouring isotopes. (Original in colour.)

avoided all unwanted masses, thus removing the need to do a background subtraction at this stage. This detailed analysis considerably improved on the resolution previously achieved through similar methods and was crucial for low cross section studies such as this.

Doppler correction

The beam energy used in this experiment leaves the reaction residues with a velocity of $\sim 0.08 c$ when the γ rays are emitted. This will cause a considerable Doppler shift, as well as substantial broadening of the peaks due to the finite size of the individual Ge detectors. As such, it is crucial to apply an accurate Doppler correction to the γ -ray energy and use the segmentation of the detectors near 90° to minimise the effects of Doppler broadening. The following analysis procedures were developed in collaboration with Paul Kent [26] in order to achieve the best possible Doppler correction, making the most of the limited statistics available in this low cross section experiment.

This was achieved by measuring the centroid of a known peak in each of the 14 detector rings and plotting this value versus $\cos \theta$ for each ring. This was done for the 1084 keV, $\frac{9}{2}^- \rightarrow \frac{5}{2}^-$ transition in ^{49}Cr [17] as it was a very intense transition. A straight line was fitted to the two forward-most and backward-most rings allowing an initial value of β to be determined using the non-relativistic Doppler shift formula, i.e. $\frac{E_0}{E} = 1 - \beta \cos \theta$. This value is then used to apply a crude Doppler correction using the relativistic Doppler shift formula, $\frac{E_0}{E} = \gamma(1 - \beta \cos \theta)$, where $\gamma = (1 - \beta^2)^{-1/2}$. The variance of the now Doppler corrected centroids was calculated and an iterative localisation algorithm was applied to minimise variance by varying β .

Additionally, a procedure to minimise the peak broadening effects of variations in β was undertaken following the technique developed in ref. [27]. The ^{49}Cr region in the $\Delta E-E$ matrix was sliced into ten sections along the total energy axis and β was calculated using the above method for each slice. This was plotted against the average total energy for that slice, producing a clear linear relationship. The gradient and intercept were determined and used in later analysis to apply a recoil-energy dependant Doppler correction on an event-by-event basis.

The reason for the linear relation between total energy and β (rather than β^2) is not fully understood but it is thought to result from energy loss in the degrader foil and the ionisation chamber window removing the expected linearity with β^2 . Once β and γ

had been calculated, the relativistic Doppler correction was applied to the γ -ray energy, with the angle for each γ ray adjusted according to the segmentation tag created during the compression stage. As this Doppler correction method was performed on ^{49}Cr it will not be exactly correct for other nuclei. However, comparison of γ -ray peak widths from a variety of nuclei suggest that these discrepancies are minimal.

The above technique, coupled with the segmentation routine, served to minimise the two principle effects leading to the Doppler broadening of γ -ray peaks:

$\Delta\theta$ — the variation in angle at which γ rays are detected, which is manifested most significantly at 90° , and

$\Delta\beta$ — the variation of velocity at which the γ rays are emitted, which is most significant at 0° and 180° .

While the former is a standard analysis procedure which has been integral in the design of detector arrays for some time, the latter is a novel technique, found to be as significant at forward and backward angles as the segmentation is at 90° .

Further background removal

The analysis up to this point allowed the selection of $Z = 26$ and $A = 49$, producing an ^{49}Fe spectrum. This spectrum is shown in Fig. 2.9, with an additional gate (and background subtraction) on the RFGGE timing signal to reduce γ rays detected as random coincidences with scattered beam. This spectrum, although free from ^{52}Fe , contains several identifiable peaks from the strongest reaction channels, namely ^{49}Cr , ^{48}V , ^{49}V and ^{46}Ti (see Table 2.2). Although ^{49}V is not one of the strongest channels, it is present here as nuclei with $A = 49$ are preferentially transmitted through the FMA. Conversely, ^{45}Ti is not transmitted, whereas ^{46}Ti is present due to a charge-state ambiguity (i.e. $A/Q = 46/18 \approx 49/19$).

It appears that this residual background was principally from $A = 49$ residues so an attempt was made to generate a suitable $A = 49$ background spectrum that could be subtracted. This was achieved by producing a γ -ray spectrum with the same gating conditions used for the ^{49}Fe spectrum (e.g. polygonal $A = 49$ gate, timing gate and background subtraction) but with no condition on Z . This produced a very intense spectrum dominated by the $A = 49$ nuclei produced in the experiment. A tiny fraction of this was subtracted from the ^{49}Fe spectrum to remove the remaining contaminants.

The resulting spectrum is shown in Fig. 2.10. It is clear that all the contaminants

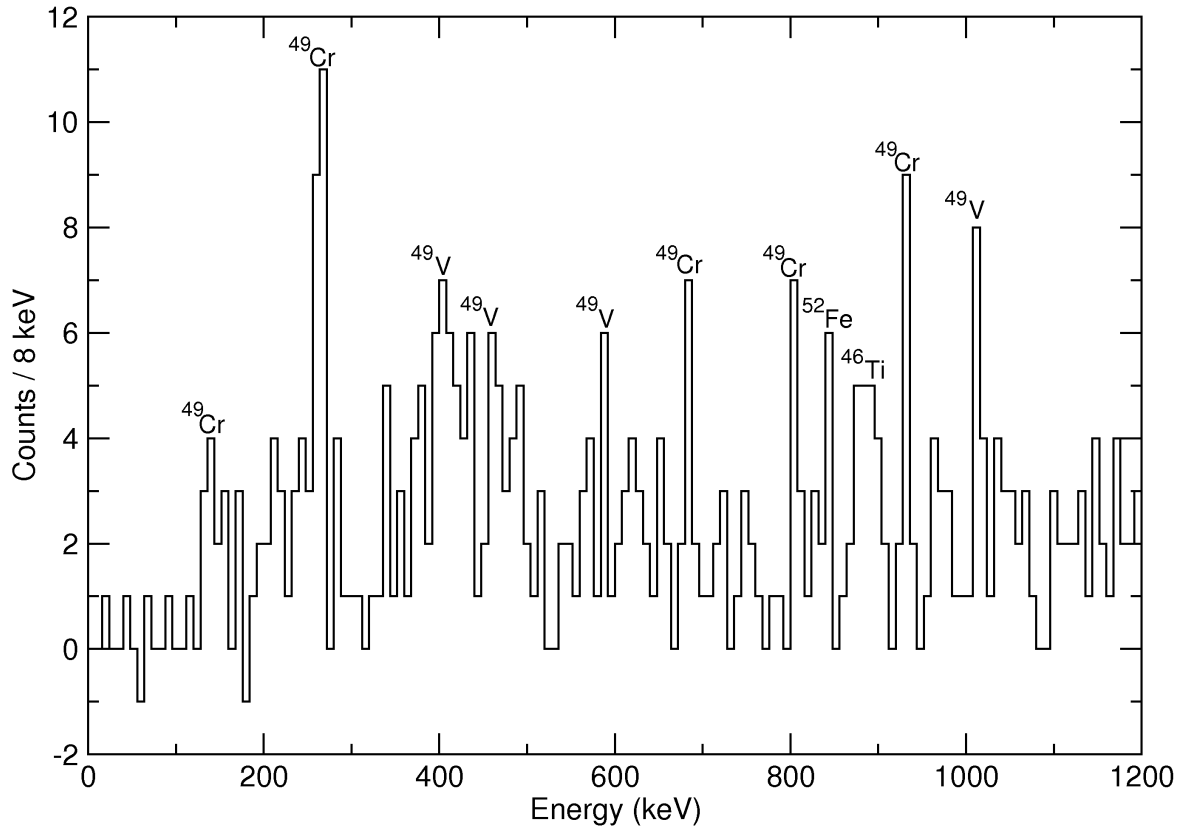


Figure 2.9: Gamma-ray spectrum produced by selecting $Z = 26$, $A = 49$ residues, with timing conditions and background subtraction. The spectrum is dominated by $A = 49$ residues other than ^{49}Fe , with small amounts of other isotopes, e.g. ^{46}Ti .

Table 2.2: Table of predicted cross sections for the ten strongest exit channels from the $^{40}\text{Ca} + ^{12}\text{C} \rightarrow ^{52}\text{Fe}^*$ reaction, calculated using PACE 4 [28].

Isotope	σ (mb)	σ/σ_{tot} (%)
^{48}V	311	28.5
^{45}Ti	142	13.0
^{46}Ti	126	11.5
^{49}Cr	113	10.3
^{46}V	70	6.5
^{48}Cr	68	6.3
^{45}Sc	51	4.7
^{43}Sc	42	3.9
^{49}V	33	3.0
^{39}K	31	2.8

have successfully been removed without over subtraction of any peaks. However, there are no peaks which deviate significantly from the background level, indicating that ^{49}Fe has not been produced at the expected $\sim 1.5 \mu\text{b}$ level. This results in an essentially empty spectrum and is discussed further in Chapter 3.

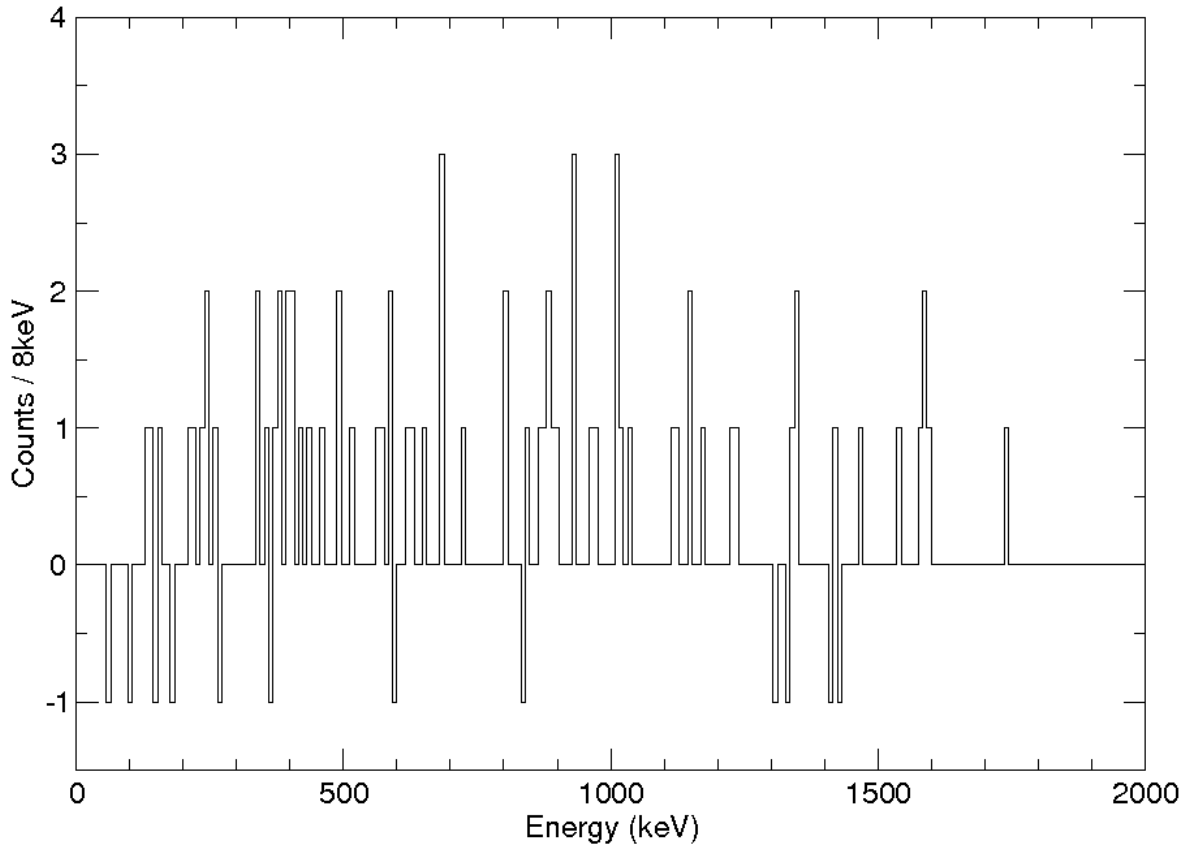


Figure 2.10: ^{49}Fe gated spectrum with background subtractions, see text for details.

Chapter 3

Results of microbarn γ -ray spectroscopy

The absence of any discernible peaks in the ^{49}Fe spectrum in Fig. 2.10 leads us to believe that ^{49}Fe was not populated at the expected $1.5 \mu\text{b}$ level. Crude yield calculations suggest that had the cross section been $1.5 \mu\text{b}$, even given the loss of data outlined in Section 2.3, we would expect to have seen ~ 75 γ rays in the strongest peak, i.e. the $\frac{11}{2}^- \rightarrow \frac{7}{2}^-$ transition. Given the level of statistics present in Fig. 2.10, a peak with 10 counts would be readily visible, hence an upper limit of $0.2 \mu\text{b}$ is implied. This result conflicts strongly with the results of the test experiment which reported ~ 3000 ^{49}Fe recoils observed in 10 hours of beam-time and confirmed the cross section estimate. It is believed that the limitations of the *old Et²* method (thought to stem from the presence of the degrader foil) were not noted due to the absence of sufficient γ -ray data, and the reported 3000 ^{49}Fe residues were most likely the tail of the ^{52}Fe distribution.

The best explanation as to why the cross section was not as expected stems from the origin of the estimate. It was based on the work of Cerny *et al.* [19] who reported a $\sim 0.5 \mu\text{b}$ cross section for the inverse reaction at a centre-of-mass energy of 50 MeV. No uncertainty was quoted for this value so its reliability cannot be assessed. Furthermore, Cerny's experiment was not attempting to observe excited states in ^{49}Fe so a centre-of-mass energy ~ 3 MeV higher was chosen in order to populate the first few excited states.

There is some evidence that the variation of cross section with beam energy for $3n$ evaporation channels forms a very narrow distribution, peaked near the Coulomb barrier [29]. As our beam energy produced a centre-of-mass energy ~ 30 MeV above the

Coulomb barrier, it seems quite likely that our beam energy was too high, leading to a significant reduction in the cross section. Similar results have been observed in $3n$ exit channels in the $A = 100$ region where factors of 50 reduction in cross section have been reported between experiments near the Coulomb barrier and those ~ 30 MeV above it [30]. Given these considerations, if another attempt were made to perform γ -ray spectroscopy on ^{49}Fe with this reaction, it is critical that a full excitation function is performed in order to determine the optimum reaction energy.

Nevertheless, the rigorous analysis required to produce a γ -ray spectrum without any residual contamination, through justifiable techniques, demonstrates the level of low cross-section spectroscopy which can be achieved using Gammasphere and the FMA. The development of new and existing analysis techniques such as the improvements to the Et^2 calculations; the use of multiple ion chamber matrices; the precise recoil-energy dependent, event-by-event Doppler correction calculations and segmentation routine; in addition to the careful consideration of sources of background contamination, were all essential in achieving this level of sensitivity.

Chapter 4

High-luminosity mirrored fragmentation reactions

As we have seen in Chapters 2 and 3, it is extremely difficult to observe excited states in $T_z = -\frac{3}{2}$, $f_{7/2}$ nuclei using fusion-evaporation reactions from stable beams. This results primarily from the prohibitively small production cross sections for the nuclei of interest compared to stronger contaminant exit channels, and the strong energy dependence of the cross section. Therefore, in order to further the study of MED in this region a new method of production has been sought. This chapter reports on an experiment to demonstrate the suitability of a high-luminosity, *mirrored* fragmentation technique for the study of proton-rich nuclei in the $f_{7/2}$ shell. Details are given of the experimental setup and the analysis performed using standard NSCL techniques and software.

4.1 Radioactive ion beams

In recent years, a number of radioactive ion beam (RIB) facilities have become available with bespoke recoil separation and spectroscopy devices. These facilities permit access to previously unreachable regions of the nuclear chart such as the neutron dripline. RIBs are generally produced by one of two methods: isotope separation on-line (ISOL), or projectile fragmentation.

4.1.1 Isotope Separation On-Line

ISOL facilities use beams of light ions (or even proton beams) accelerated to high energies (100 MeV – 1 GeV) which impinge on thick targets of heavy material such as uranium carbide. Reaction products are thermalised in the target and allowed to diffuse to the surface where they are ionised, separated from unwanted species and re-accelerated. This allows the energy of the RIB to be exactly specified by the experimenter, hence this method is of particular applicability to nuclear-astrophysics where stellar environments can be simulated with beams at $\sim 0.5 - 2$ MeV/nucleon. A major virtue of this technique is the high beam quality (i.e. purity, spot size, angular divergence and energy range) that can be achieved, comparable even to that of stable beam experiments. This method, however, is limited to certain species, primarily as a result of chemical processes preventing the extraction of the reaction product from the target. Additionally, and to a lesser extent, the relatively slow beam production mechanism (~ 100 ms or greater) can limit the beams which can be produced as reaction products begin to beta decay before they are delivered to the experiment, resulting in loss of beam intensity, or no beam at all in extreme cases. Indeed, the release of reaction products from the target is dependent on a number of factors, such as the target composition and temperature, making the development of a particular beam a research project in itself.

4.1.2 Projectile Fragmentation

The alternative method, projectile fragmentation, typically uses heavier beams accelerated to between 0.1 and 1 GeV/nucleon and incident on relatively thin targets, although still thick when compared to a typical target from a fusion-evaporation experiment. The projectile is fragmented into a variety of lighter nuclei which emerge from the target at close to their incident velocity. This residual beam cocktail is then separated *in-flight*, primarily using electric and magnetic fields, before being delivered to the experiment. As the secondary beam remains at high energies throughout, it can be delivered to the experiment in times of the order of 100 ns, hence losses from beta decay are far less significant than for ISOL. The beam quality, however, is poorer than that achievable with ISOL techniques.

Reactions at such high energies can proceed via a number of processes. If the

collision between beam and target is head-on, both will be broken up into many small pieces. Alternatively, extremely peripheral collisions can directly remove particles from either the target (spallation) or the beam (knockout). Intermediate processes take a two-stage form analogous to fusion-evaporation known as abrasion-ablation [31]. Here the violent collision shears off several particles in the interaction region (abrasion), leaving the remaining nucleons in an excited state which decays via particle emission (ablation).

The beta decay half-lives of $T_z = -\frac{3}{2}$ nuclei in the $f_{7/2}$ shell are generally less than 100 ms, hence ISOL production methods are not well suited to the study of these isotopes. Projectile fragmentation, therefore, remains the best option for such experiments, particularly as the independence of cross section from beam energy remove the danger of failing to populate the nuclei of interest. Furthermore, studies have suggested that fragmentation reactions which remove five or more particles from a projectile at intermediate or relativistic beam energies are purely statistical in nature (as for fusion-evaporation reactions), hence will preferentially populate *yrast* states. Alternatively, single-hole states are selectively populated in *direct*, one-nucleon knockout reactions [32]. Two-proton removal from neutron-rich nuclei, as well as two-neutron knockout from neutron-deficient nuclei have also been shown to proceed as direct reactions [33, 34]. Three- to five-particle removal channels represent a transitional region in which both direct and statistical processes compete [35]. For these reasons, fragmentation reactions are highly suitable for the study of mirror energy differences in isobaric analogue states, particularly in many-particle removal exit channels where high-spin *yrast* states will be populated.

In order to confirm the applicability of high-luminosity, projectile fragmentation experiments to the study of MED in $f_{7/2}$ shell nuclei, an experiment was carried out at the National Superconducting Cyclotron Laboratory (NSCL) of Michigan State University. Proton rich nuclei in the $f_{7/2}$ shell were produced—along with their neutron rich mirror partners—by mirrored fragmentation reactions from a radioactive beam of the $N = Z$ nucleus, ^{56}Ni . The products of these reactions were identified with the S800 spectrograph (Section 4.3) and gamma decays from excited states were observed with the SeGA array (Section 4.4). This work represents the first attempt to study isobaric analogue states in this way.

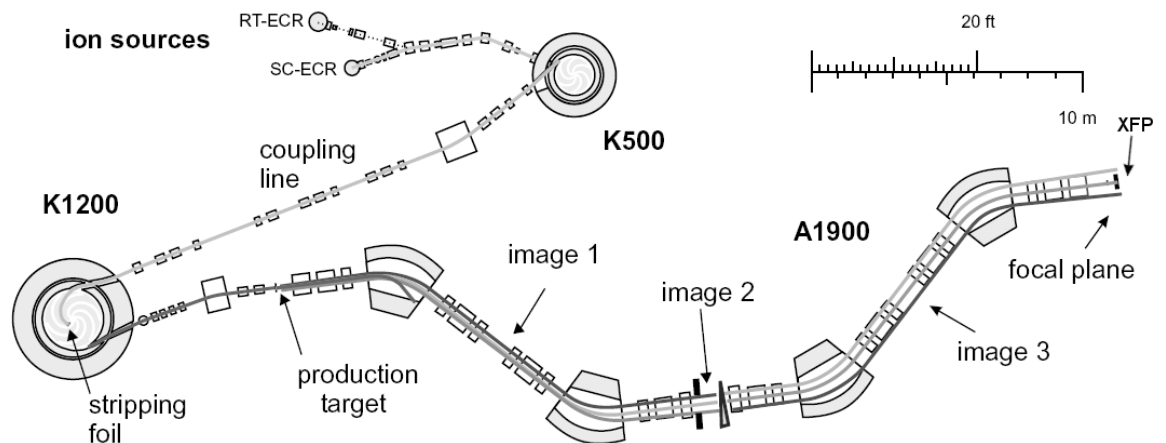


Figure 4.1: Schematic of the A1900 fragment separator and the K500 and K1200 coupled cyclotrons, taken from [37].

4.2 Beam production and the A1900

The radioactive ^{56}Ni beam was produced by fragmenting a ^{58}Ni beam provided by the Coupled Cyclotron Facility (CCF) [36]. This method was chosen over direct fragmentation of ^{58}Ni as, due to the smaller number of nucleons removed, the cross sections to the $T_z = -\frac{3}{2}$ nuclei of interest were larger. Although a ^{58}Ni beam orders of magnitude more intense than ^{56}Ni was available, other elements of the detector system, namely the OBJ scintillator (see Section 4.3) would be excessively damaged by such an intense beam. Furthermore, the detection rate in the Ge array (SeGA, see Section 4.4) would have been prohibitively high. An additional benefit to the two-step fragmentation method lies in the fact that ^{56}Ni is an $N = Z$ nucleus, which facilitates the production of both members of a mirror pair in mirrored fragmentation reactions, e.g. ^{53}Mn and ^{53}Ni are produced by the removal of either three protons, or three neutrons respectively. One would naively expect identical populations of analogue states from such reactions, hence allowing spin assignments and the construction of new level schemes based purely on mirror symmetry arguments.

The ^{58}Ni beam at 160 MeV/nucleon impinged on a 610 mg/cm^2 ^9Be production target at the object point of the A1900 fragment separator. At this high beam energy, knockout and fragmentation reactions are dominant, producing many beam-like residues with $A < 58$.

The A1900 is a high acceptance projectile fragmentation separator [37] located immediately after the K1200 element of the CCF accelerator, see Fig. 4.1. The device

Table 4.1: Main constituents of the secondary beam, as delivered to the reaction target, measured using the time-of-flight spectra in Fig. 4.2.

Beam constituent	Fraction of total transmitted beam (%)
^{56}Ni	64.48(18)
^{55}Co	31.60(12)
^{54}Fe	3.54(4)
^{53}Mn	0.34(1)
^{52}Cr	0.033(4)

utilises dipole and superconducting quadrupole magnets, with hexapole and octupole coils for aberration correction. The mixture of unreacted primary and secondary beam is initially filtered by a dispersive beam line consisting of a pair of 45° bend dipole magnets in conjunction with a variable aperture. Further selection is achieved with a 300 mg/cm^2 achromatic Al wedge and a set of momentum slits at the intermediate image position. This degrades the incident beam from a single magnetic rigidity ($B\rho$), leaving exiting ions with different momenta, dependent on their atomic number. A second dispersive beam line produces the final secondary beam cocktail consisting primarily of ^{56}Ni , with lesser amounts of lighter $N = 28$ isotones. The constitution of the secondary beam is detailed in Table 4.1.

This beam cocktail is delivered from the focal plane of the A1900, through an analysis line, which focuses it onto the reaction target at the target position of the S800 spectrograph. Two plastic scintillators positioned at the extended focal plane of the A1900 (XFP, see Fig. 4.1) and the object position (OBJ) of the S800 ($\sim 30 \text{ m}$ downstream of the XFP) provide identification of ions through time-of-flight measurements. An example secondary beam time-of-flight spectrum can be seen in Fig. 4.2. Software gates applied to this spectrum allow the secondary beam incident on the reaction target to be identified event-by-event, hence the desired reaction channel can be selected.

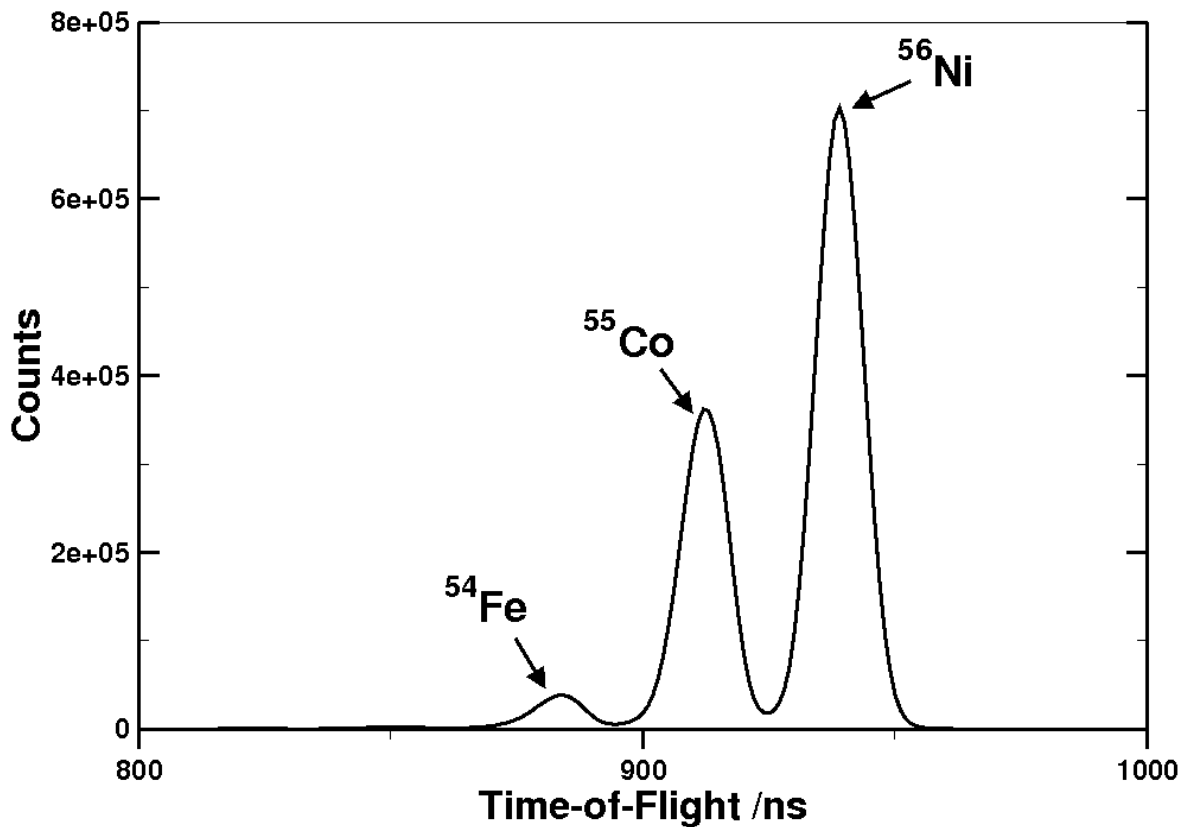


Figure 4.2: Time-of-flight spectrum of the secondary beam, measured between the XFP and OBJ scintillators

4.3 The S800 Spectrograph

The S800 is a high-resolution, large acceptance spectrograph designed for use in fast, radioactive beam experiments [38]. The device consists of the analysis line, for the identification of incoming ions, and the main spectrograph (see Fig. 4.3). This utilises two 75° bend superconducting magnets (with a maximum magnetic rigidity of 4 Tm) to disperse reaction fragments at the focal plane, where a suite of detectors is used to identify the reaction fragments.

The secondary beam cocktail from the A1900 is incident on a 188 mg/cm² ⁹Be reaction target, located after the analysis line at the target position of the S800 spectrograph. Fragmentation reactions with this target produce the nuclei of interest in excited states, the gamma decays from which are detected by SeGA, which surrounds the target.

The S800 analysis line can be operated in two different modes dependent on the objectives of the experiment. If precise measurement of momentum distributions are desired, requiring the maximum resolution the device can deliver, it is operated in

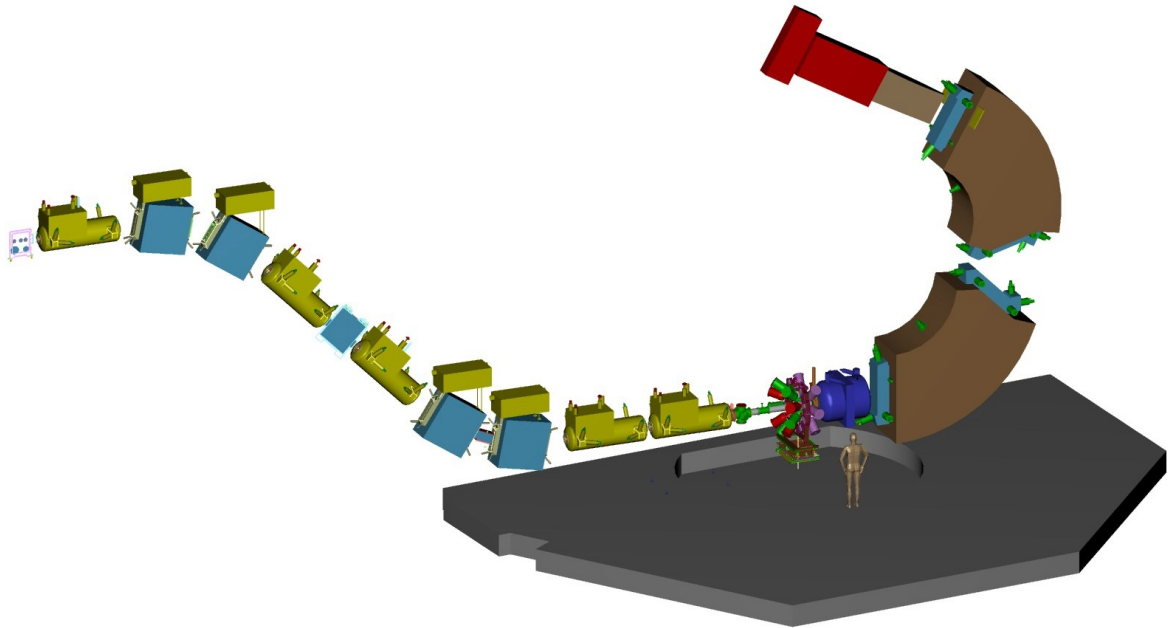


Figure 4.3: Schematic image of the S800 spectrograph with the SeGA array installed at the target position. The blue and yellow objects are the magnetic dipoles and quadrupoles of the analysis line. The OBJ scintillator is located at the left edge of the image. The S800's superconducting dipole magnets are shown in brown and the focal plane detectors in red. (Original in colour.)

dispersion-matched mode. In this experiment, however, the key objective was γ -ray spectroscopy, hence the device was operated in *focussed* mode. This focussed the beam into a spot on the target, allowing the best possible γ -ray energy resolution.

4.3.1 Focal plane detectors

The focal plane detectors [39] (the positions of which can be seen in Fig. 4.4) consist of two cathode readout drift counters (CRDCs), immediately followed by a segmented ionisation chamber and three plastic scintillators. All these devices have dimensions of 59 cm in the dispersive plane (x) and 30 cm in the transverse plane (y).

Cathode Readout Drift Counters

The CRDCs are tracking detectors which measure the positions of particles as they traverse the focal plane. They consist of a volume of gas (1.5 cm thick) filled with 80% CF_4 and 20% C_4H_{10} at 140 Torr. Incident particles ionise this gas mix, the electrons from which drift in the applied electric field to an anode wire where they are multiplied in a Townsend avalanche. Close to the anode wire are 224 individual

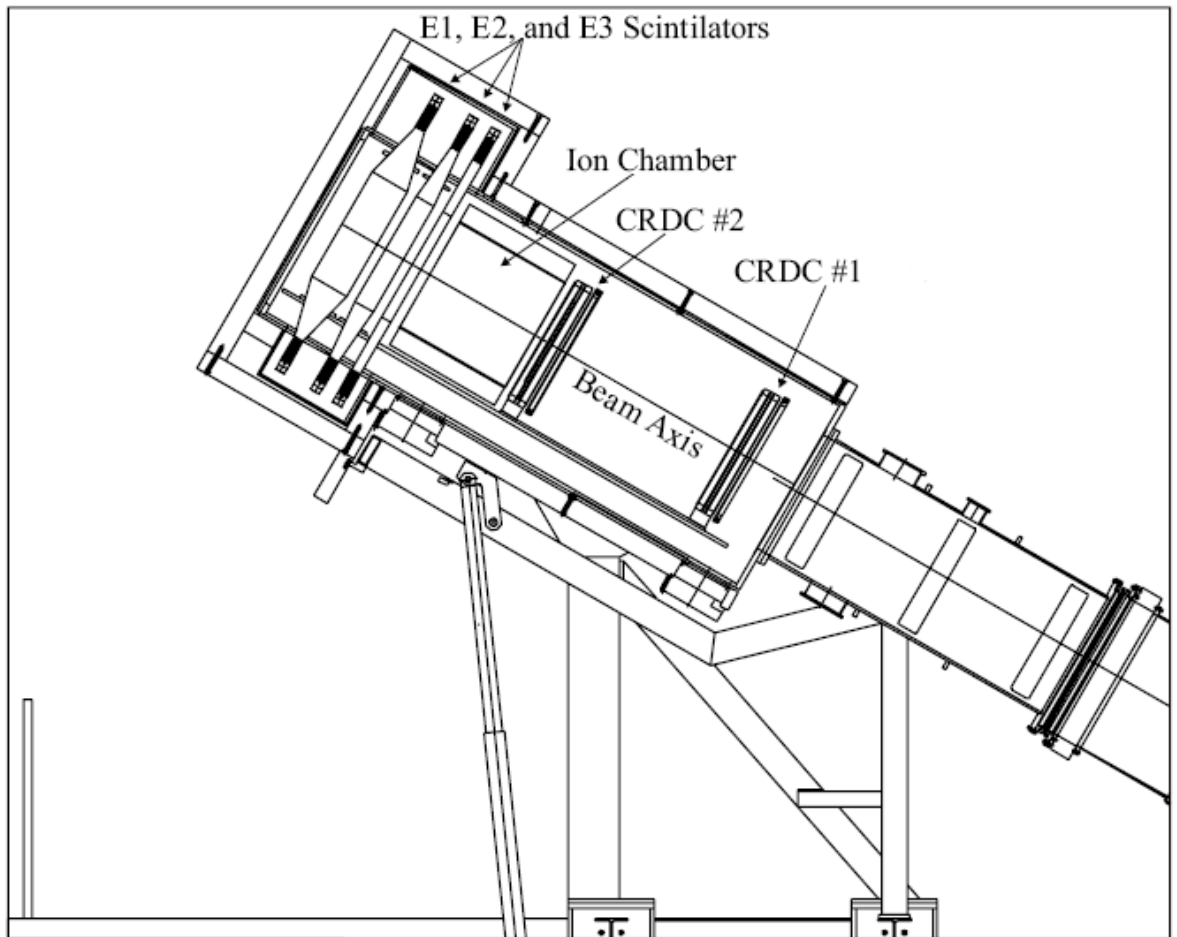


Figure 4.4: Detail of S800 focal plane detectors, taken from [40].

2.54 mm cathode pads to detect induced signals which are readout individually. A centre-of-gravity method can then be used to determine the position in the dispersive plane, or a Gaussian fit can be applied if greater resolution is required. The y position is provided by the drift time of electrons relative to the timing signal from the first scintillator. This method has been shown to provide position resolution of < 0.5 mm [39]. The use of two CRDCs, separated by 1 m, allows determination of incident angles. For example, the angle in the dispersive plane is calculated as

$$a = \tan^{-1} \left(\frac{x_2 - x_1}{d} \right) \quad (4.1)$$

where x_1 and x_2 are the positions measured in the two CRDCs and d is the separation between them.

Ion Chamber

The S800 ionisation chamber is a Frisch gridded ion chamber with a segmented anode. The chamber is 41 cm deep and filled with P10 gas at 300 Torr. The segmented anode consists of sixteen, 3 cm strips arranged perpendicular to the ions path, with individual preamplifiers within the chamber. Measurement of energy loss allows identification of incident ions, see Section 4.3.3.

Scintillation Detectors

The exit window of the ion chamber is formed by the first of three plastic scintillators (E1, E2 and E3) which are 5, 10 and 20 cm thick respectively. Incident ions generate light within the material which is guided to photomultiplier tubes where it is converted to an electrical signal. This is primarily used for timing information but, as all incident ions will be stopped within the material, energy loss and total energy measurements can also be taken. The signals are readout from both ends of the scintillators to allow mean time measurements, independent of the position. Timing responses of 160 ps FWHM have been reported [39].

4.3.2 Aberration correction

In large acceptance, high-resolution spectrographs such as the S800, aberrations in the magnetic field can have significant effects on the resolution of the device. In the A1900 these effects are corrected through the use of hexapole and octapole coils to make fine adjustments, however, due to the large acceptance of the S800, these corrections become considerably more complex. In order to avoid these issues, trajectory reconstruction techniques are utilised. The profiles of the magnets' fields are measured and fitted, from which an inverse transfer map can be calculated. A detailed description of the field mapping and reconstruction is given in [41]. This map relates initial parameters at the target to those measured at the focal plane (i.e. positions x and y , and angles a and b in the dispersive and transverse planes), hence trajectories can be recreated and the high-resolution of an ideal device achieved [42]. This reconstruction also allows determination of the angles θ and ϕ of the nucleus at the target position when γ rays are emitted, and hence can be used to improve the Doppler reconstruction (see Section 4.4.2).

4.3.3 Particle identification with the S800 spectrograph

In order to identify reaction products at the focal plane, a number of calibration procedures must be carried out to relate the parameters measured with the focal plane detectors to real quantities.

CRDC Calibration

The first of these relates the signals from the CRDCs to real spatial coordinates by placing a calibration mask in the beam line before the CRDCs. A series of holes and slits cut in this mask at known positions transmit small beam spots into the CRDCs, the signals from which can be correlated with the corresponding hole. This allows the electron drift times to be calibrated such that they correspond to the real spatial y position. A short run of this kind was carried out at the beginning of the experiment however, as the electron drift time is sensitive to the gas composition, small changes can lead to significant shifts in the y position. In order to resolve this, a particular isotope is selected with software gates (as described later in section 4.3.3) and its position in the CRDCs is tracked throughout the experiment. As the $B\rho$ settings in the S800 magnets remain constant, a correction may be applied to the CRDC signals to maintain the correct y coordinate.

Since the cathode pads are at fixed positions within the detectors, they can readily be translated into the x coordinates. However, the signals from the pads can differ by as much as $\pm 6\%$ [40], hence a gain matching procedure is applied.

Ion Chamber Calibration

The signals from the sixteen segments of the ionisation chamber are gain matched, such that each segment records the same energy loss for a given event, then summed to provide the total energy loss in the detector. This method has the advantage over a single anode device as the electronic noise is proportional to capacitance, which is reduced by having smaller anode segments. The noise in the segments are not correlated, hence are summed in quadrature, reducing the total noise of the device.

The energy loss is known to vary as a function of x and y as a result of charge losses due to drift length. This too is corrected for using the positions measured with

the CRDCs. From consideration of the Bethe-Bloch formula we see that

$$\Delta E \propto \frac{Z^2 A}{E}, \quad (4.2)$$

hence, the calibrated energy loss (ΔE) can now be used for isotopic selection.

Scintillator Calibration

The time-of-flight (TOF) of ions are measure between the OBJ and E1 scintillators and used to identify the reaction products. As

$$B\rho = \frac{A}{Q}v, \quad (4.3)$$

where v is the velocity of the fragment, only ions with the correct momentum for the S800 settings will be transmitted to the focal plane and, for a given charge state (Q), their TOF will be proportional to mass (A). Small differences in momentum will cause ions to travel a different path through the spectrograph (ions with significantly different momenta will not reach the focal plane), hence arriving at a different spot at the focal plane. Applying linear corrections to the TOF, dependent on position and angle measured with the CRDCs, allows these variations in momentum to be accounted for.

As stated previously, the OBJ scintillator was the limiting factor in the beam current which could be used during the experiment as the optics required the beam to be focused onto a small area of this scintillator. This caused considerable damage to the detector such that the signal was significantly degraded. In order to compensate for this, the voltage applied to the photomultiplier tubes were increased every few hours over the course of the experiment. In addition to this, the position of the scintillator (and the scintillator itself) was changed several times during the experiment when a particular spot became too radiation damaged. These changes led to shifts in the timing signal from the OBJ scintillator which had to be tracked and corrected.

Particle Identification

Correctly calibrated time-of-flight and energy loss signals can now be combined in a two-dimensional spectrum which allows unique identification of all isotopes. Fig. 4.5

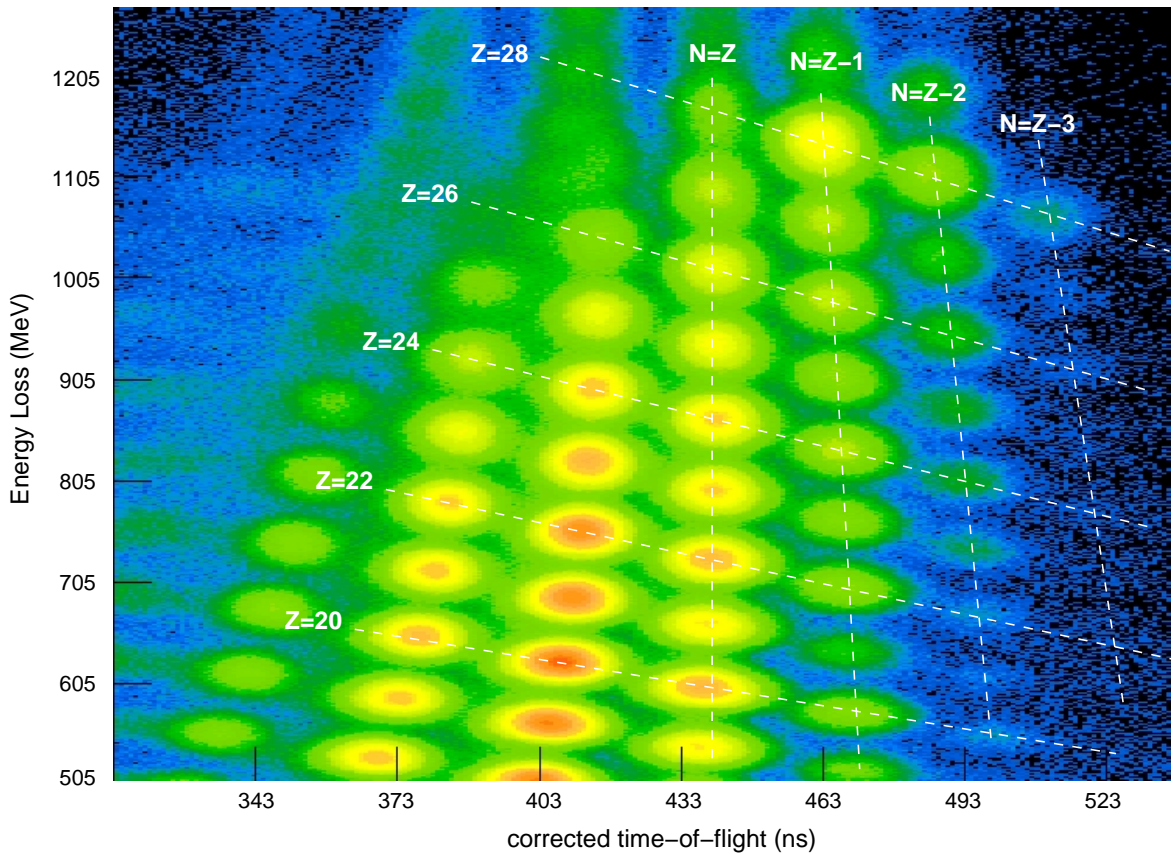


Figure 4.5: PID used to identify reaction products at the focal plane of the S800. Corrected time-of-flight measured from the OBJ to E1 scintillators is plotted on the x -axis, with energy loss (ΔE) in the ionisation chamber shown on the y -axis. (Original in colour.)

shows an example of a particle identification spectrum (PID) produced in this way. Each *blob* corresponds to a different isotope, which can clearly be distinguished from its neighbours. Software gates applied to this spectrum provided extremely selective identification of reaction products, allowing generation of gamma-ray spectra free from contamination from other reaction channels.

4.4 The SeGA array

The target position of the S800 is surrounded by an array of up to eighteen thirty-two fold segmented, high-purity germanium detectors called SeGA (SEgmented Germanium Array) [43]. This array has been designed primarily for use in intermediate-energy radioactive beam experiments but can be arranged in a number of additional configurations optimised for different experiments such as lifetime measurements or stopped beam spectroscopy. The standard configuration, when used in conjunction with the

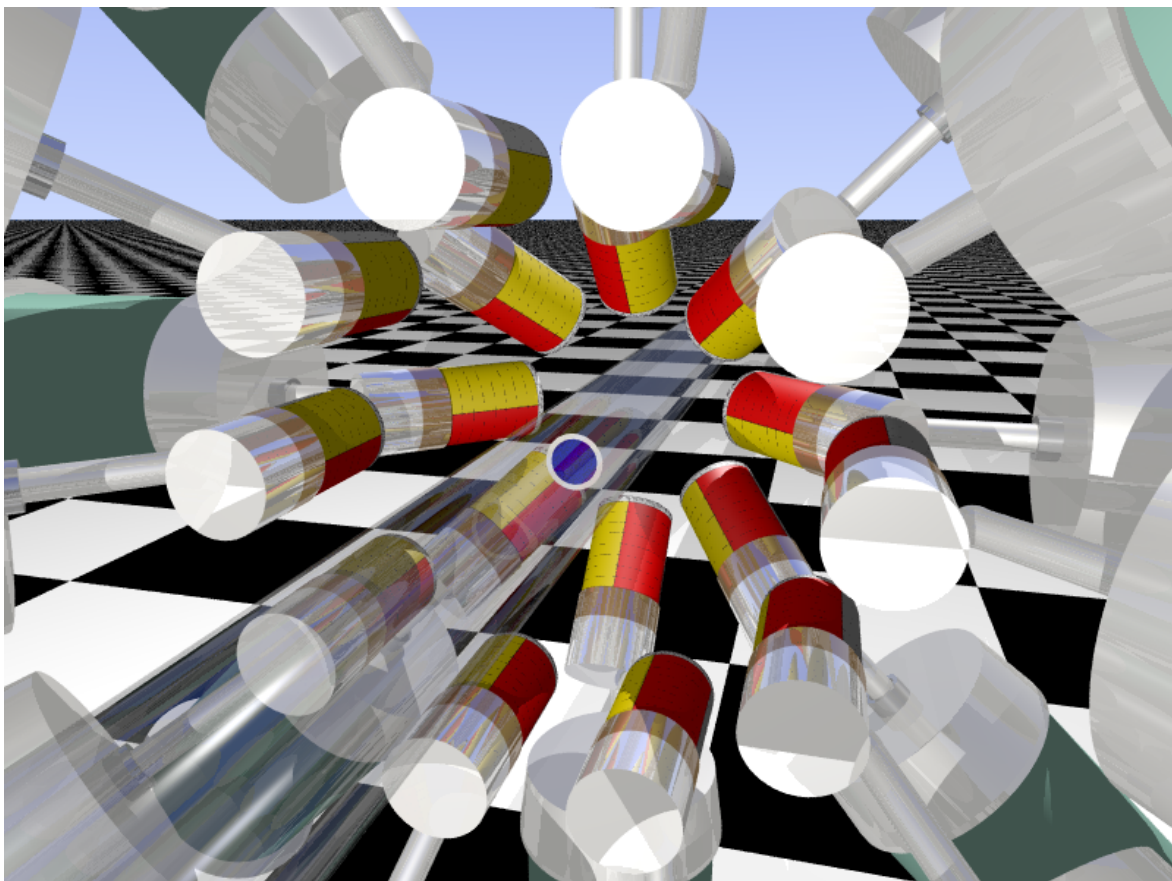


Figure 4.6: Schematic of the Segmented Germanium Array, viewed from upstream. The two detector rings at 37° and 90° are visible, along with the target position shown in blue. Note that, in his work, one detector was absent from each ring. Image taken from [40]. (Original in colour.)

S800, consists of 17 detectors, 24.2 cm from the target position, arranged in two rings at 37° and 90° with respect to the beam axis. The geometry of the array can be seen in Fig. 4.6. The forward ring contains 7 detectors (one has to be removed due to the presence of a large gate valve on the first quadrupole magnet of the S800) while the 90° ring has 10 (only 9 detectors were available for this ring during the experiment, making a total of 17 detectors). This arrangement is configured to optimise the efficiency of the array when used with heavily Doppler-boosted fast beams.

The array was designed with the three principle issues contributing to energy resolution in mind, i.e. the intrinsic resolution of the detectors, the uncertainty in the angle of detection due to the opening angle of the detector ($\Delta\theta$), and the uncertainty in the beam velocity ($\Delta\beta$). The last of these is a particular issue in fast-beam experiments. The intrinsic detector resolution is minimised through use of high-purity germanium detectors but due to the low relative efficiency of these devices they must typically

be placed close to the target, hence negating the improvements in resolution due to the increased angular size of the detectors. The development of segmented detectors has gone some way to addressing this dilemma and the design of the SeGA detectors utilises this technology.

The individual SeGA detector elements are based on closed-end cylindrically-symmetric coaxial germanium crystals with a 70 mm diameter and 80 mm in length [44]. The outer contacts of the crystals are electronically segmented into eight 1 cm disks along the axis-of-symmetry and four quadrants radially creating 32 segments in total (see Fig. 4.7). The novel aspect of the SeGA detectors is their orientation: rather than placing the detectors with their axis-of-symmetry pointing toward the target position, it is aligned perpendicular to this. This leaves the eight lateral segments facing the source, providing a 1 cm position resolution and minimising $\Delta\theta$. High-resolution energy information can then be read from the central contact, while the segments are used to determine the angle of the detected γ ray for use in the Doppler reconstruction.

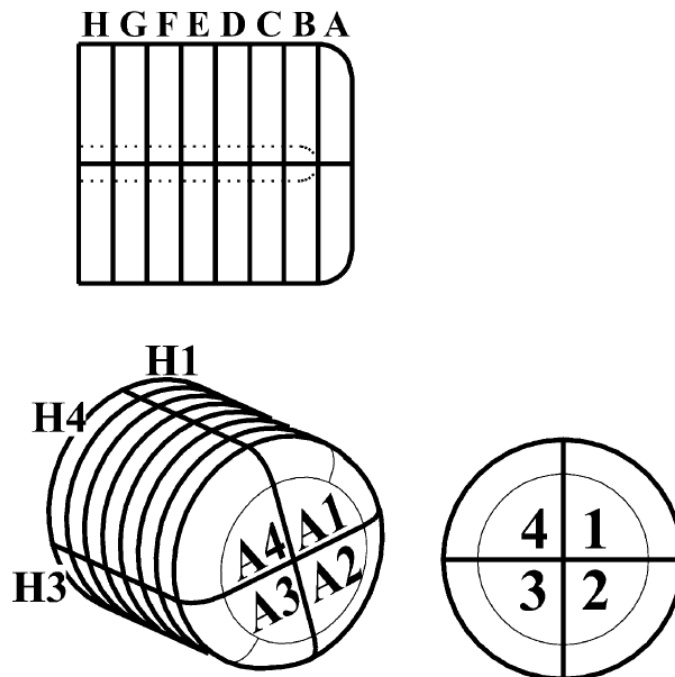


Figure 4.7: Schematic diagrams of a SeGA crystal. The radial and lateral segmentation is shown with the labelling convention used to identify them. The dotted line indicates the dimensions of the central contact. Image taken from [44].

4.4.1 Energy and efficiency calibration of SeGA

Calibration runs were undertaken before and after the main experiment using $^{56,60}\text{Co}$, ^{152}Eu and ^{226}Ra sources. Gamma-ray peaks at well defined energies allowed calibration of the signals from the detector cores to linearly transform channel number into energy in keV. In addition to this, two γ -ray peaks—at 511 keV (annihilation radiation) and 1809 keV (from ^{26}Al decay, present in the beam pipe, Ge encapsulation etc.)—were tracked during the in-beam experimental runs to allow correction for gain drift. This effect was found to be minimal during the experiment. These calibrations were carried out by Kyle Siwek, a PhD student at Michigan State University [45].

Gamma-ray energy is always read from the central contact of the Ge crystals, the segment readouts are only used for identification of which segment is hit for use in the Doppler reconstruction. The probability of a typical-energy γ ray interacting with a single segment is small so an algorithm is implemented to determine the most likely initial interaction point, this is described graphically in Fig. 4.8 [43]. The angle from the target to the segment determined to have interacted first is then used for the Doppler reconstruction. As the energy recorded in the segment is utilised in this process, the segments must also be accurately calibrated to facilitate the best possible Doppler reconstruction. This calibration is achieved by comparing the energy detected in the segment to the calibrated core energy. These values should, of course, be the same so by analysis of a large volume of data (i.e. from in-beam experimental runs), parameters can be determined to correct segment energy data to the core values.

Furthermore, the activity of the ^{152}Eu source was precisely measured on May, 1, 1978 [46]. By calculating the remaining activity of the source at the time the calibration runs were carried out, and combining this with the expected gamma-ray intensities per disintegration (taken from [47]), we can produce an efficiency curve for the detectors. The absolute photopeak efficiency is given by:

$$Eff. = \frac{Peak\ Area}{I \times A \times t \times (1 - t_D)} \quad (4.4)$$

where I is the intensity per radioactive decay for a given γ ray, A is the activity of the source, t is the duration of the calibration run, and t_D is the deadtime. By fitting the

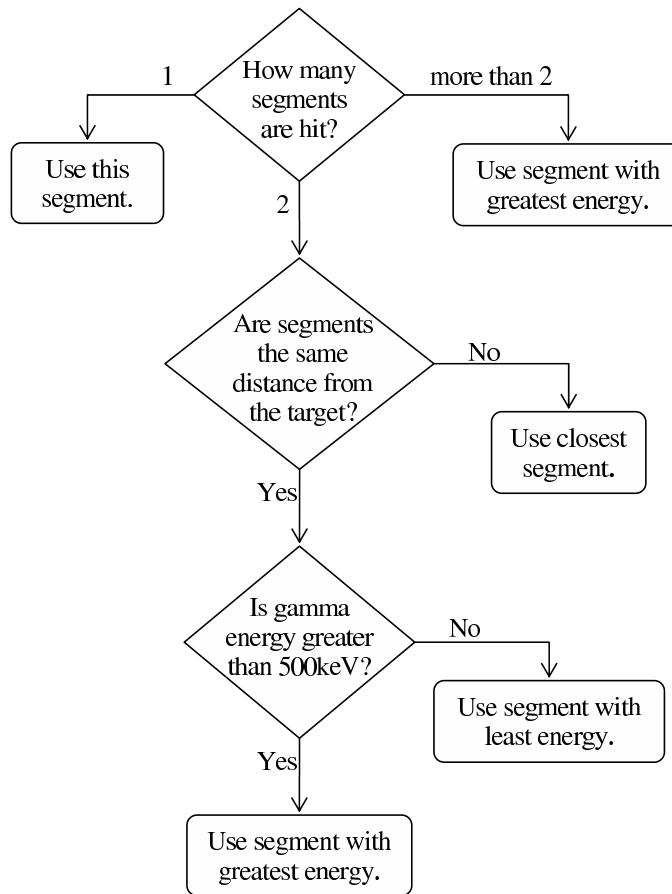


Figure 4.8: Flowchart depicting the process used to assign the first segment hit for use in the Doppler reconstruction.

data with a function of the form:

$$Eff. = a \cdot (E_{lab} - c)^{-b} \quad (4.5)$$

where E_{lab} is the γ -ray energy in the lab frame and a , b and c are coefficients obtained from the fit, we can determine the absolute photopeak efficiency of the detectors at any energy. The seven detectors in the forward ring have been grouped together and the measured efficiencies for the γ decays from the ^{152}Eu source are plotted in Fig. 4.9, along with the efficiency curve fitted to this. This is an idealised curve as the true efficiency should peak around 100 keV and drop sharply to zero at lower energies, however, the lowest energy γ ray available for calibration was at 122 keV. The lowest energy gamma ray observed during the experimental runs was at ~ 110 keV (in the lab frame, see Section 4.4.2), hence use of this curve is acceptable.

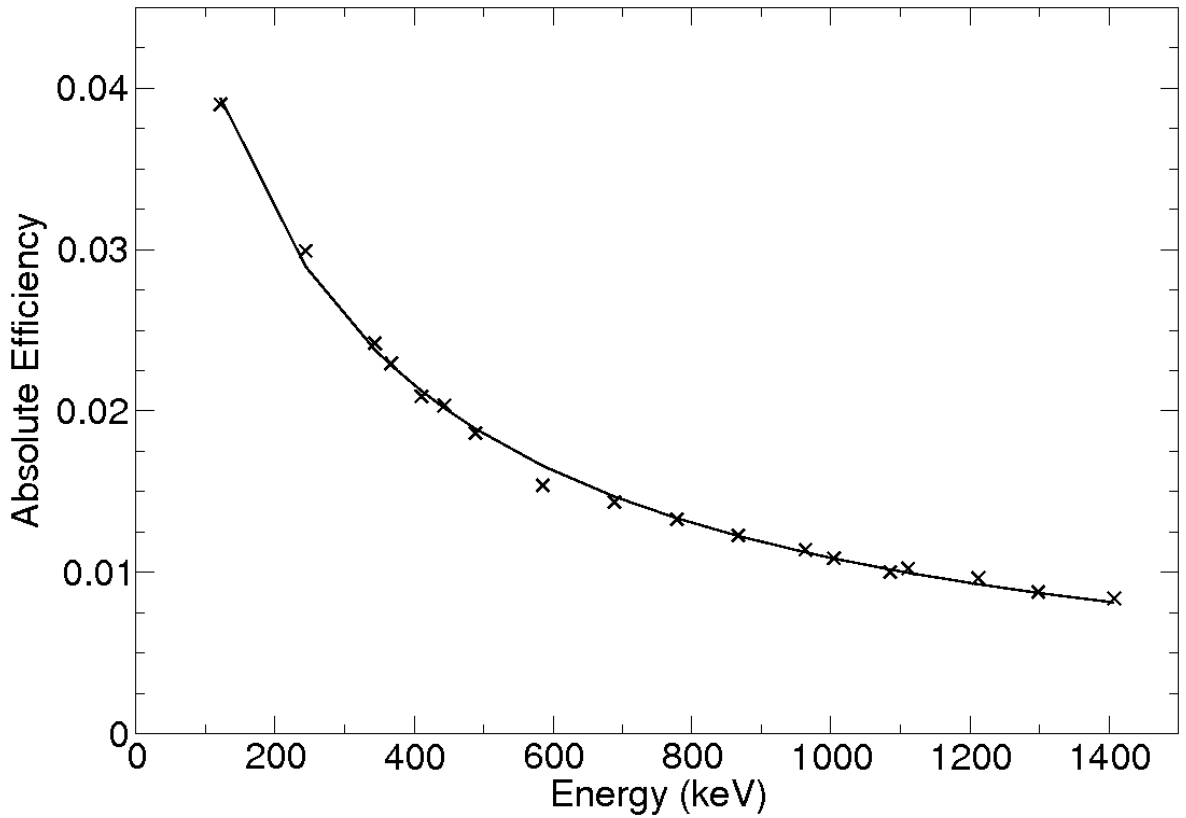


Figure 4.9: Efficiency curve for the forward ring of SeGA. Data points are measured with a ^{152}Eu source, the line is a fit to this data.

4.4.2 Doppler reconstruction of γ rays

As the nucleus gamma decays whilst in flight it is travelling with considerable velocity. This causes the γ -ray energy to be Doppler shifted considerably in the lab frame. The γ -ray energy in the rest frame of the nucleus (E_γ) can be reconstructed using:

$$E_\gamma = \frac{E_{lab}(1 - \beta \cos \theta)}{\sqrt{1 - \beta^2}} \quad (4.6)$$

where E_{lab} is the energy observed in the lab frame, θ is the angle of the γ ray relative to the beam axis (determined as described in Section 4.4.1), and β is the velocity of the beam (v/c). The angles of each segment of SeGA are precisely known relative to some reference point, however, the target is positioned by hand within the beam pipe, hence is only approximately in the centre of the array. The angle the γ ray is detected at is, of course, a function of the target position along the z axis, hence this leads to a slight reduction in resolution. This issue is resolved by studying known γ decays from strongly populated isotopes. As the energies of these γ decays are well known we can find the unique combination of β and z that shifts the γ -ray peaks to the correct energy

in both detector rings. In practice this can simply be achieved by adjusting β until peaks in both rings line up, then adjust z until the combined peak is at the correct energy. The two ring spectra will no doubt have now shifted so by iteratively repeating this process a correctly Doppler reconstructed spectrum can be generated for a given isotope. The value of z determined here can now be used for Doppler correction of other isotopes with unknown γ -ray energies, by adjusting β only to align the peaks in both rings.

For extremely weak channels it may not be possible to see γ -ray peaks in the individual ring spectra, hence another method for optimising the Doppler reconstruction must be used. This can be achieved for reaction products for which several other isotopes were produced in the experiment via a systematic process. In such cases, β was found to vary systematically across the isotopic chain, hence, by optimising β for several strongly produced isotopes we can extrapolate to the isotope of interest.

So far we have assumed that all γ rays are emitted from the same point, roughly in the centre of the target, however, at the relativistic beam velocities used in this experiment, the lifetimes of excited states become significant. For a typical, short-lived state, the excited nucleus will travel a short distance in the target before decaying which will depend on the lifetime of the state, and the states feeding it. This makes it impossible to align all of the γ -ray peaks at once so a compromise must be made that suits the majority of peaks. Some states may have lifetimes significantly longer than these typical values, hence will decay considerably downstream of the target. Applying the standard Doppler reconstruction to these states will not produce the correct γ energy, hence such states must be treated separately (see Section 5.2.3).

4.4.3 Production of clean γ -ray spectra

Gating on the incoming beam and the resulting PID plot allows extremely clean selection of the reaction channel of interest, without any contamination from neighbouring channels. Gamma-ray spectra can be produced in this way for the nuclei of interest, however, these spectra still contain significant sources of contamination. These result from the Compton continuum—present due to the lack of Compton suppression shields like those used on Gammasphere (see Section 2.2.2)—but more significantly, from *bremsstrahlung* radiation. As a beam particle traverses the target it decelerates in the nuclear electric field. Any charged particle which changes its velocity must lose

energy in the form of electromagnetic radiation, which, due to the considerable beam velocity, appears in the form of a γ -ray continuum.

One method considered for the reduction of this background was subtraction of a γ -ray spectrum in coincidence with the ^{56}Ni exit channel. It was hoped that this spectrum would be a pure *bremsstrahlung* spectrum, as the incoming and outgoing beams were both ^{56}Ni . However, three large peaks resulting from inelastic scattering are present in this spectrum, the energies of which correspond to the $6^+ \rightarrow 4^+ \rightarrow 2^+ \rightarrow 0^+$ *yrast* cascade of ^{56}Ni [48]. This spectrum can be seen in Fig. 4.10. The broad peak at 2700 keV may result from the 2638 keV, 8^+ to 6^+ transition, unresolved with the 2700 keV, 2^+ to 0^+ decay.

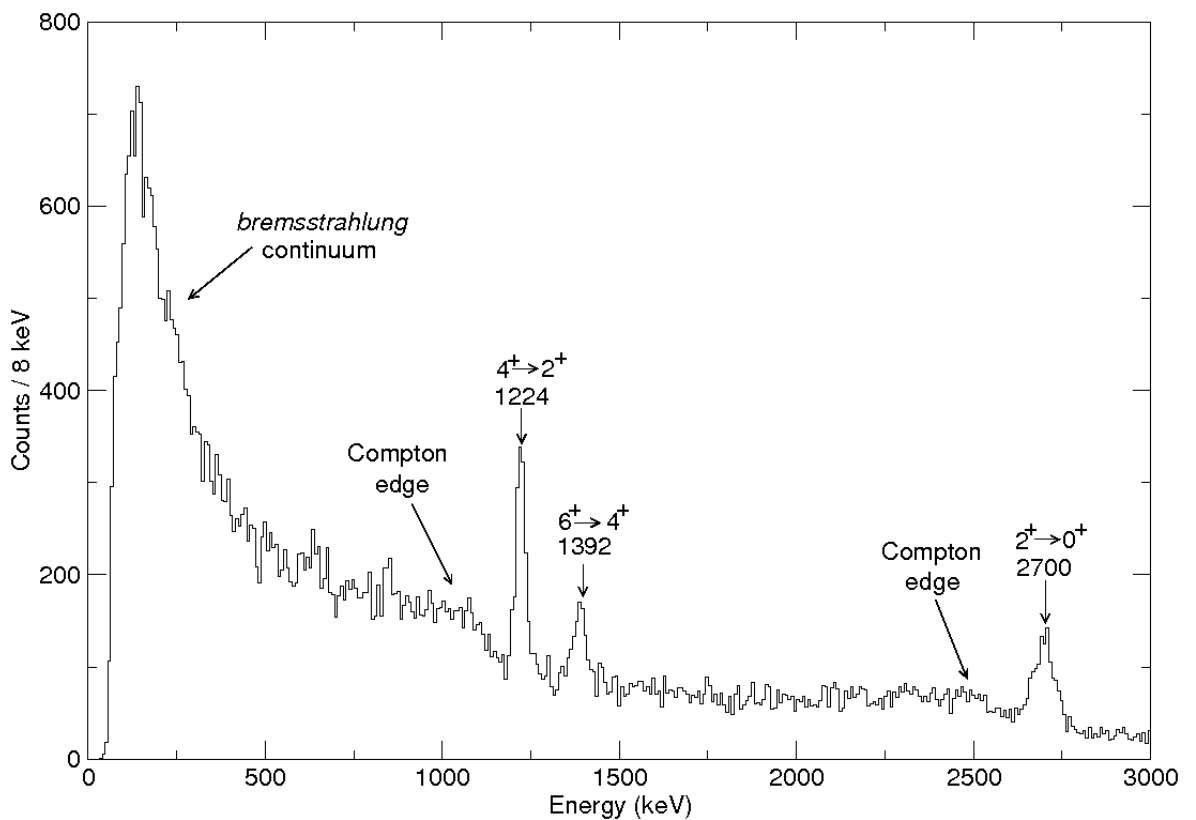


Figure 4.10: Gamma-ray spectrum created in coincidence with ^{56}Ni recoils. Decays from the $J^\pi = 6^+$, 4^+ and 2^+ states can be seen following inelastic scattering of the ^{56}Ni beam.

Timing conditions

An alternative method for the reduction of the *bremsstrahlung* background can be achieved by placing stringent timing conditions on detected γ rays. This eliminates γ rays not associated with the fragment detected at the focal plane, most of which will

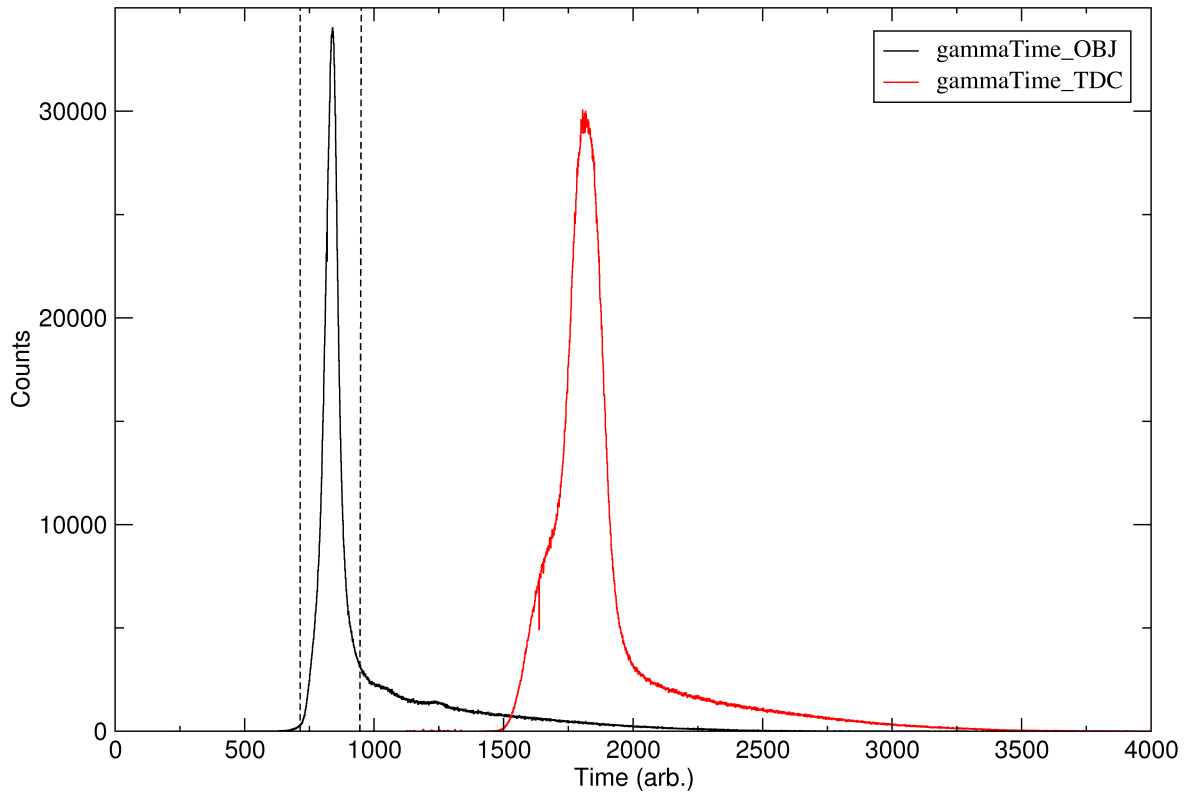


Figure 4.11: γ -ray timing spectra for the raw TDC values and relative to the OBJ scintillator. The timing window applied is indicated. (Original in colour.)

be from *bremsstrahlung* radiation. This is best achieved by measuring the timing signal from the Ge crystals relative to the OBJ scintillator, which is chosen rather than the E1 scintillator (i.e. the raw TDC values started by the trigger) as the beam has lost temporal coherence at the focal plane due to energy loss in the target. The difference in timing resolution between these two signals can be seen in Fig. 4.11, along with the timing window applied. The effect of this gating is to reduce the *bremsstrahlung* background at low energies ($\lesssim 1000$ keV), however, as the timing response of SeGA is poor at very low energies ($\lesssim 300$ keV), peaks in this region are also attenuated. At higher energies ($\gtrsim 1000$ keV) this gating has little effect, therefore the improvement in peak-to-background occurs between ~ 300 keV and ~ 1000 keV. We can see an example of this in Fig. 4.12. Note that in the un-gated spectrum the 531 keV peak is dwarfed by the *bremsstrahlung* background, whereas in the time-gated spectrum it is comparable in height.

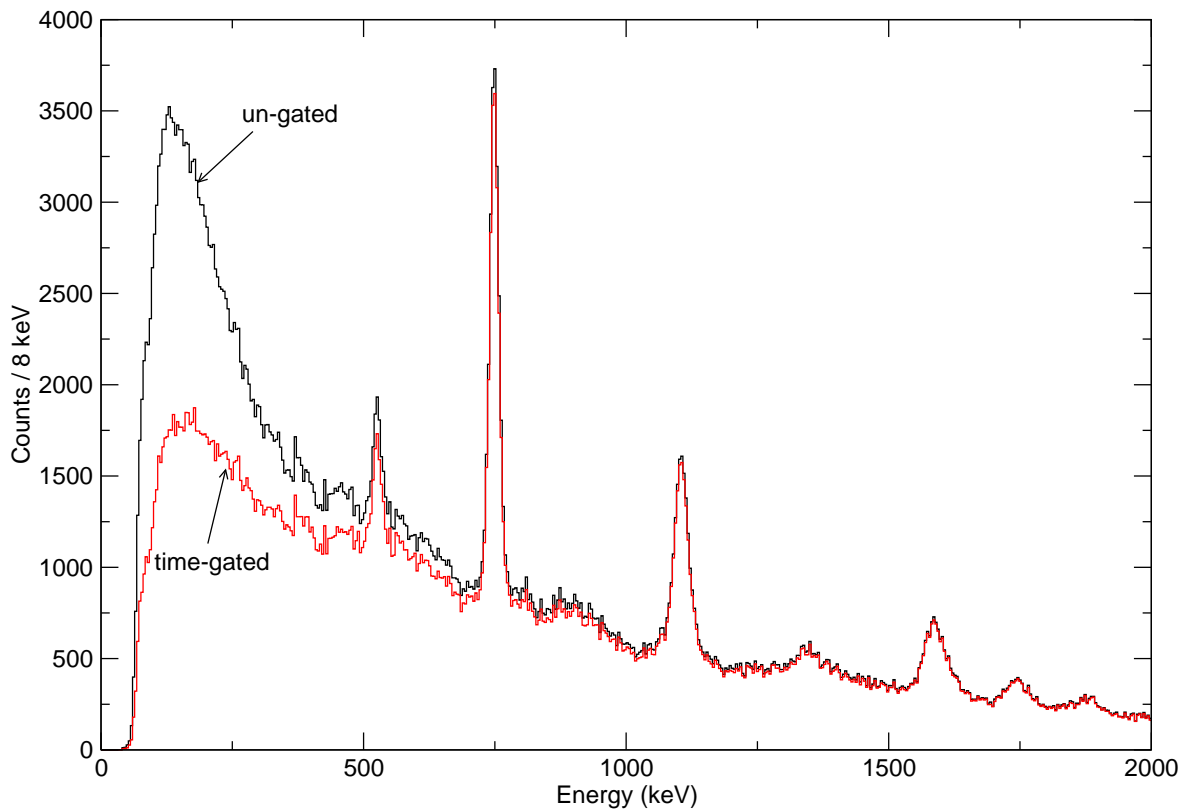


Figure 4.12: γ -ray spectra in coincidence with ^{48}Cr recoils, with and without time-gates. The reduction of the *bremsstrahlung* background is clear. (Original in colour.)

Multiplicity conditions

A further technique for background reduction relies on the reaction mechanism used in this experiment. As outlined in Section 4.1.2, fragmentation reactions that remove only a few nucleons can proceed via direct processes. This implies that a low γ -ray multiplicity should be expected, particularly given the low geometric efficiency of SeGA. We can therefore assume that if two or more γ rays are detected in coincidence, at least one of these is likely to be from background sources, i.e. *bremsstrahlung* radiation. By requiring that spectra are only incremented with γ rays from multiplicity-one events we can reduce the background in few-nucleon removal channels.

As we can see from the top panel of Fig. 4.13 (^{53}Mn spectra—the 3 proton removal channel), applying the multiplicity condition alone reduces the counts fairly uniformly across the energy range. However, when this gate is applied in conjunction with the timing conditions described above, the *bremsstrahlung* background is essentially removed completely, while the peak at 378 keV is left relatively unaffected (see Fig. 4.13, bottom panel). It is striking that the reduction far surpasses that achieved with either gate individually.

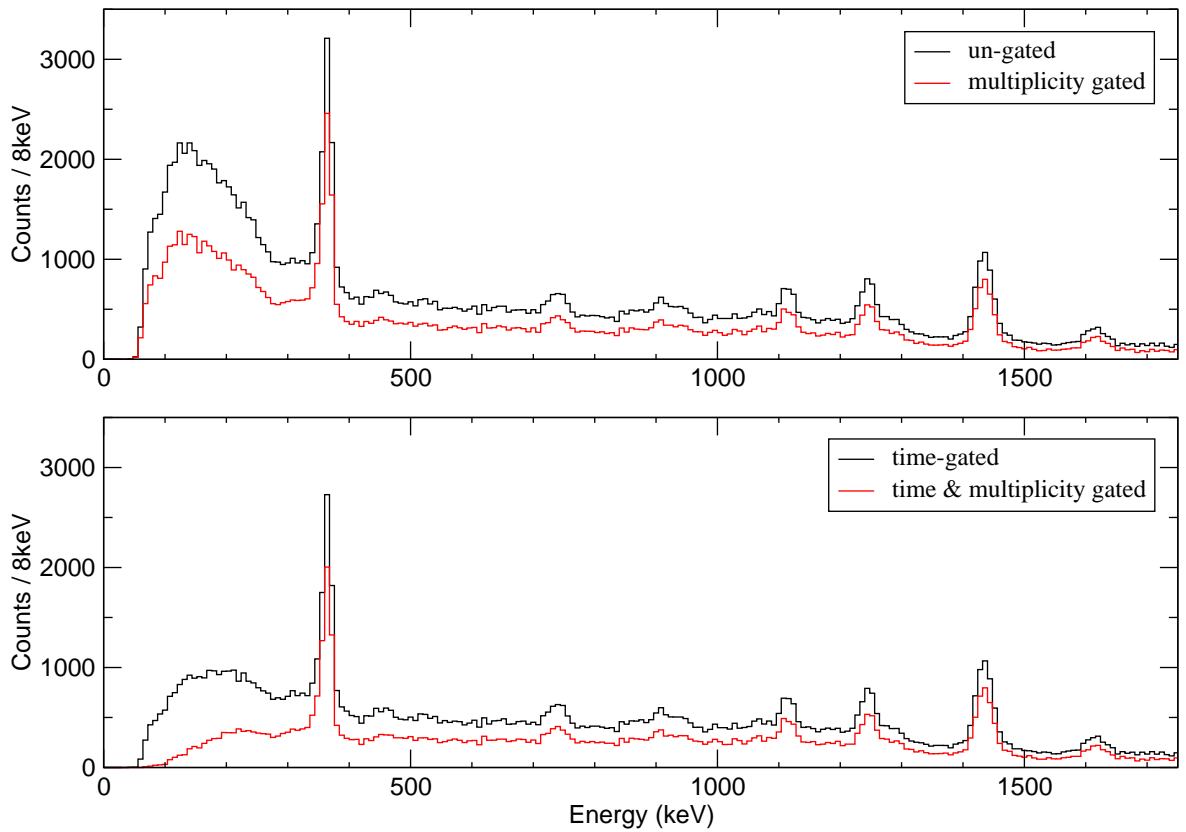


Figure 4.13: γ -ray spectra produced in coincidence with ^{53}Mn recoils, with various gating conditions applied. See text for details. (Original in colour.)

In many-nucleon removal channels, however, the improvement in peak-to-background is not so evident when these methods are combined, hence only the timing conditions are applied to such channels. This is believed to be because the nucleus is left in a higher spin state following the removal of a greater number of nucleons, hence yielding a higher γ -ray multiplicity.

Chapter 5

Results from fragmentation reactions

As was shown in Fig. 4.5, a great many isotopes were produced in this experiment. Experimental runs were undertaken with two magnetic rigidity settings centred on the $T_z = -\frac{3}{2}$ and $T_z = +\frac{3}{2}$ reactions products. These lasted for approximately 38, and 4 hours respectively, due to the considerable differences in production cross sections for the proton-rich and neutron-rich isotopes. The following chapter reports on the analysis of the $A = 49$ and $A = 53$, $T_z = \pm\frac{3}{2}$ mirror pairs, the first successful γ -ray spectroscopy of $T_z = \pm\frac{3}{2}$ nuclei above $A = 33$ [18]. This work has been published, in part, in ref. [49]. Additionally, the $A = 54$, $T_z = \pm 1$ mirror pair (in which several isobaric analogue states have previously been identified [9]) is studied in order to assess the extent to which isobaric analogue states are symmetrically populated in mirrored fragmentation reactions.

Gamma-ray spectra have been produced for a number of nuclei of interest following the calibrations and corrections described throughout Chapter 4, with various combinations of the gating conditions described in Section 4.4.3. All spectra were produced in coincidence with the ^{56}Ni component of the secondary beam, such that only mirror nuclei produced in mirrored fragmentation reactions are considered. This facilitated confident assignment of mirrored γ decays from isobaric analogue states based purely on mirror symmetry arguments. Hence, spins and parities can be assigned to states and new level schemes constructed, without the need for γ - γ analysis. Indeed, sufficient statistics were barely obtained for such analysis of the $T_z = +\frac{3}{2}$ nuclei, let alone the weakly populated $T_z = -\frac{3}{2}$ nuclei.

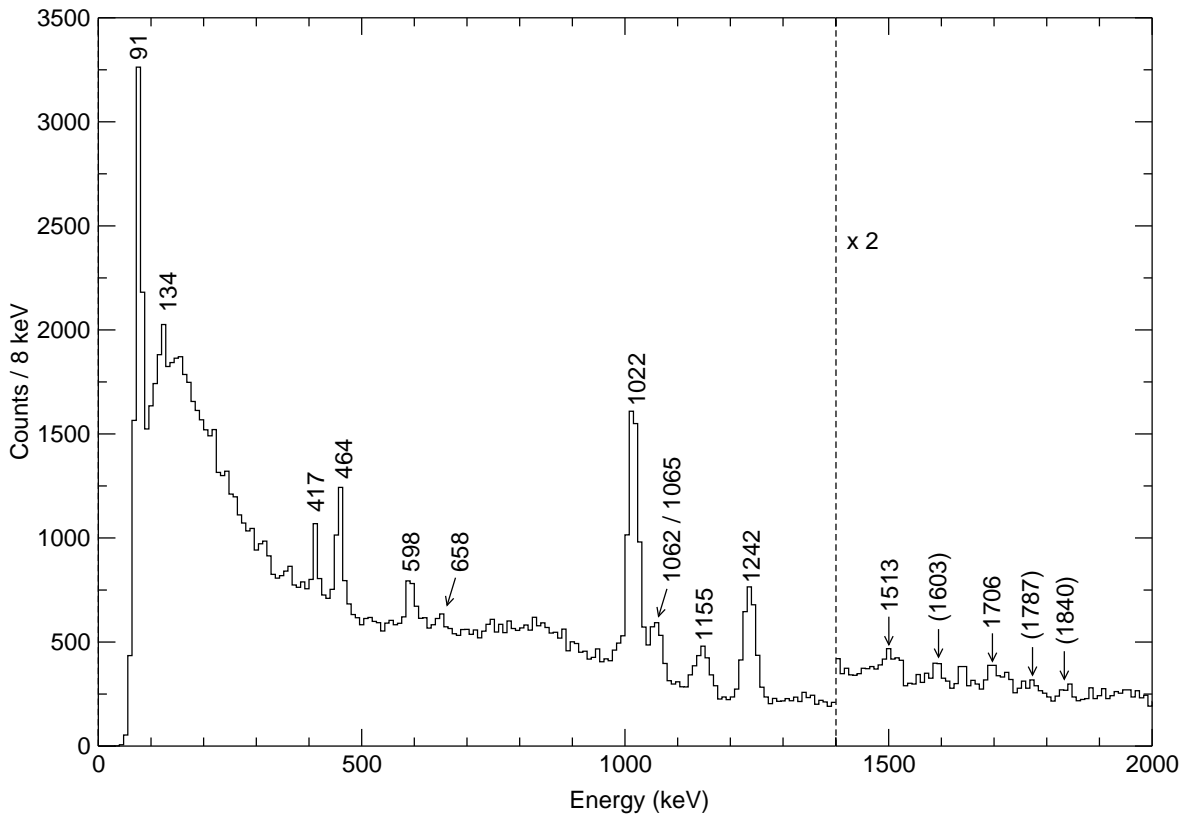


Figure 5.1: Gamma-ray spectrum produced in coincidence with ^{49}V recoils at the focal plane. The spectrum has been enhanced above 1.4 MeV to show the weak, high-energy peaks more clearly. Peaks labelled in parentheses are tentative but included for completeness.

5.1 The $A=49$, $T_z = \pm\frac{3}{2}$ mirror pair

5.1.1 Spectroscopy of ^{49}V

As the production cross section for the proton-rich member of each mirror pair is so much smaller than for the neutron-rich member, the later nucleus was analysed first in order to determine the optimum gating conditions. To this end, a preliminary ^{49}V spectrum has been produced which is shown in Fig. 5.1. Gamma-rays have been observed up to 1840 keV (tentatively) and can be identified with known γ decays [17]. Sufficient statistics were not obtained to perform a full γ - γ analysis and further confirm the ordering and spins of these excited states. Instead a partial level scheme has been constructed for the observed transitions following the ordering from [17] which extends up to the 5530 keV, $J^\pi = \frac{21}{2}^-$ *yrast* state and includes a number of unnatural parity states (see Fig. 5.2).

A number of the γ rays were observed by Cameron *et al.* [50] as multiplets, therefore,

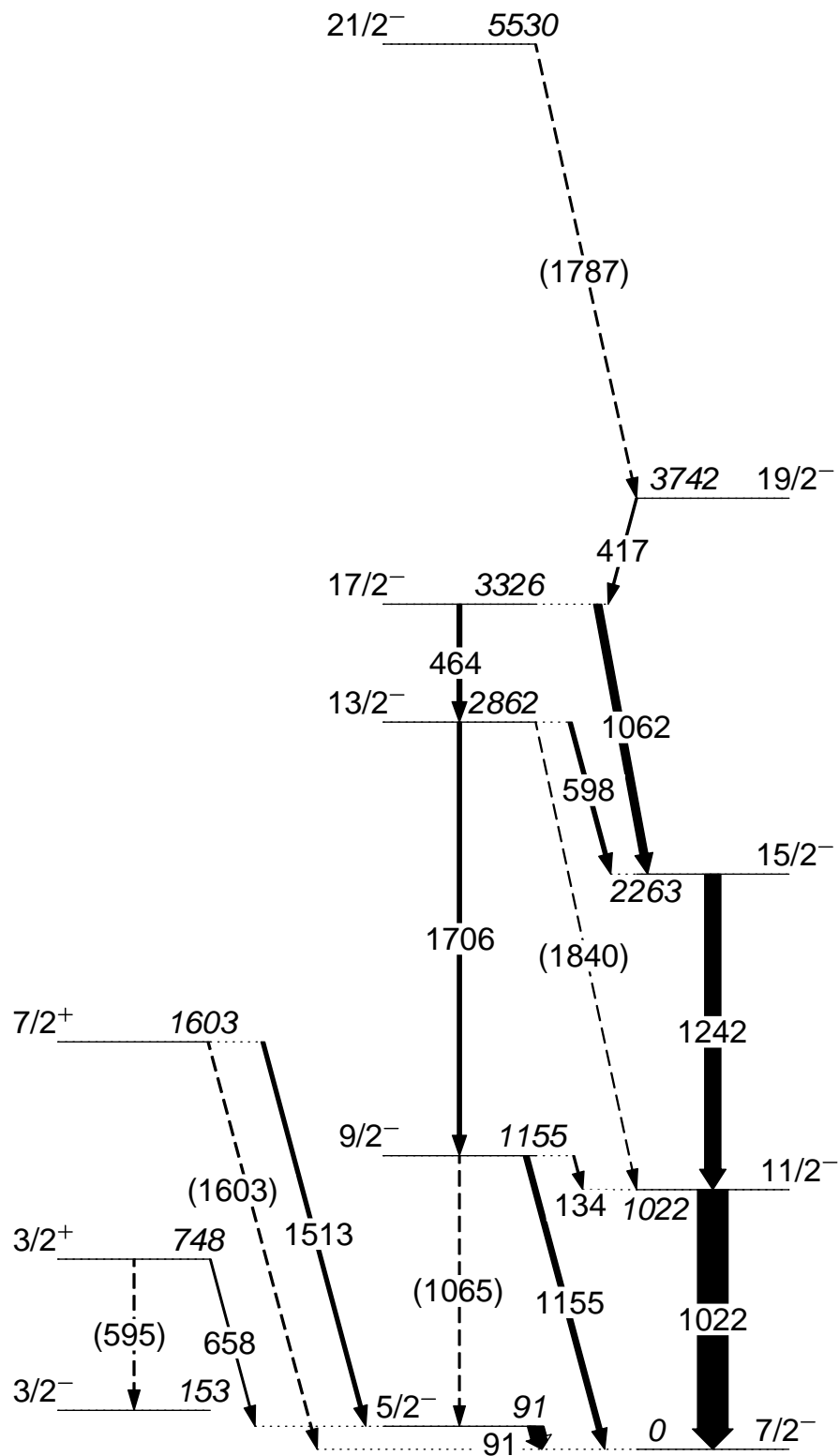


Figure 5.2: Level scheme of ^{49}V showing the γ rays observed in this work. Energies, ordering, and spins and parities are taken from [17]. Tentatively observed γ rays are labelled in parentheses. Transition widths are proportional to γ ray intensities measured in this work.

in the interests of simplicity, non-*yrast* states have been ignored. Coincidence analysis was performed for the 1062 / 1065 keV doublet which confirmed that the 1062 keV, $\frac{17}{2}^-$ to $\frac{15}{2}^-$ decay is dominant. This can be seen in Fig. 5.3 (a spectrum in coincidence with 1022 keV transition) in which the decays feeding the $\frac{11}{2}^-$ state are evident, whereas the 1022 itself and the 1155 keV decays are absent. The 1062 keV transition is still present in approximately the same ratio to the 1242 keV decay, indicating that little intensity has been lost from the removal of the 1065 keV decays. Nevertheless, this decay is included in the level scheme for completeness with an intensity derived from previous measurements [17] relative to the 1155 keV decay.

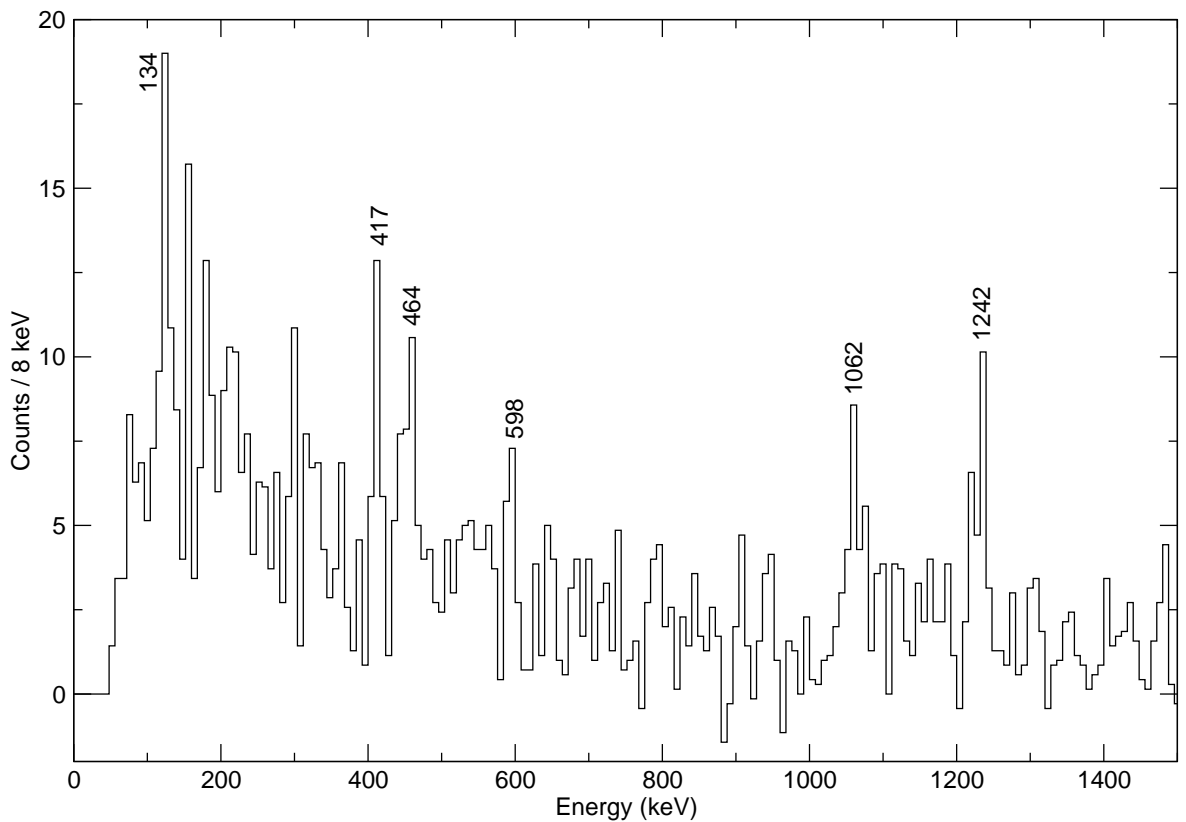


Figure 5.3: Gamma-ray spectrum produced in coincidence with ^{49}V recoils and the 1022 keV γ -ray transition.

This level scheme demonstrates the high spins of states which can be populated in fragmentation reactions in which many particles are removed (seven in this instance). The relative intensities (normalised to the 1022 keV transition) of the observed γ rays have been measured by fitting the peaks and dividing by the detector efficiency (calculated with Eqn. (4.5)). These are tabulated in Table 5.1.

In order to improve this spectrum, and determine the optimum gating conditions for the weak proton-rich mirror partner, the gating conditions discussed in Section

Table 5.1: Details of excited states of ^{49}V observed in this experiment. All values, except relative γ -ray intensities ($I_{\gamma(\text{rel})}$), are taken from [17].

E_x (keV)	J^π	$t_{\frac{1}{2}}$	E_γ (keV)	$I_{\gamma(\text{rel})}$	E_f (keV)	J^π
					Final State	
0.0	$\frac{7}{2}^-$	330 d				
90.6	$\frac{5}{2}^-$	228 ps	90.6	51.0(1)	0.0	$\frac{7}{2}^-$
152.9	$\frac{3}{2}^-$	19.90 ns				
748.3	$\frac{3}{2}^+$	5.3 ps	657.6	5(2)	152.9	$\frac{5}{2}^-$
			595.4 ^a	5.9	90.6	$\frac{3}{2}^-$
1021.6	$\frac{11}{2}^-$	3.4 ps	1021.6	100(3)	0.0	$\frac{7}{2}^-$
1155.3	$\frac{9}{2}^-$	1.1 ps	1155.3	18(2)	0.0	$\frac{7}{2}^-$
			1064.6 ^b	5.4	90.6	$\frac{5}{2}^-$
			133.8	6(1)	1021.6	$\frac{11}{2}^-$
1602.7	$\frac{7}{2}^+$	0.47 ps	1512.0	12(3)	90.6	$\frac{5}{2}^-$
			1602.6	6(2)	0.0	$\frac{7}{2}^-$
2263.3	$\frac{15}{2}^-$	0.65 ps	1241.7	53(2)	1021.6	$\frac{11}{2}^-$
2861.5	$\frac{13}{2}^-$	0.10 ps	598.3	13(2)	2263.3	$\frac{15}{2}^-$
			1706	13(3)	1155.3	$\frac{9}{2}^-$
			1840	3(2)	1021.6	$\frac{11}{2}^-$
3325.2	$\frac{17}{2}^-$		464	15(1)	2861.5	$\frac{13}{2}^-$
			1061.9	26(2)	2263.3	$\frac{15}{2}^-$
3742.4	$\frac{19}{2}^-$		416.9	7(1)	3325.2	$\frac{17}{2}^-$
5529.7	$\frac{21}{2}^-$		1787	5(2)	3742.4	$\frac{19}{2}^-$

^a This transition is not observed due to the presence of the stronger 598 keV transition. It is included for completeness, along with the $\frac{3}{2}^-$ state it decays into. The intensity is calculated from the relative intensity taken from [17].

^b This transition forms a doublet with 1062 keV decay which, from γ - γ analysis, we know to be dominant. Intensity calculated from [17].

4.4.3 were investigated. The γ -ray multiplicity for many-particle removal channels is expected to be too high to allow an effective reduction of the *bremsstrahlung* background by considering only single gamma-ray events. Hence, a further γ -ray spectrum has been produced for ^{49}V using the timing conditions only. This spectrum can be seen in Fig. 5.4, superimposed on the original spectrum for comparison.

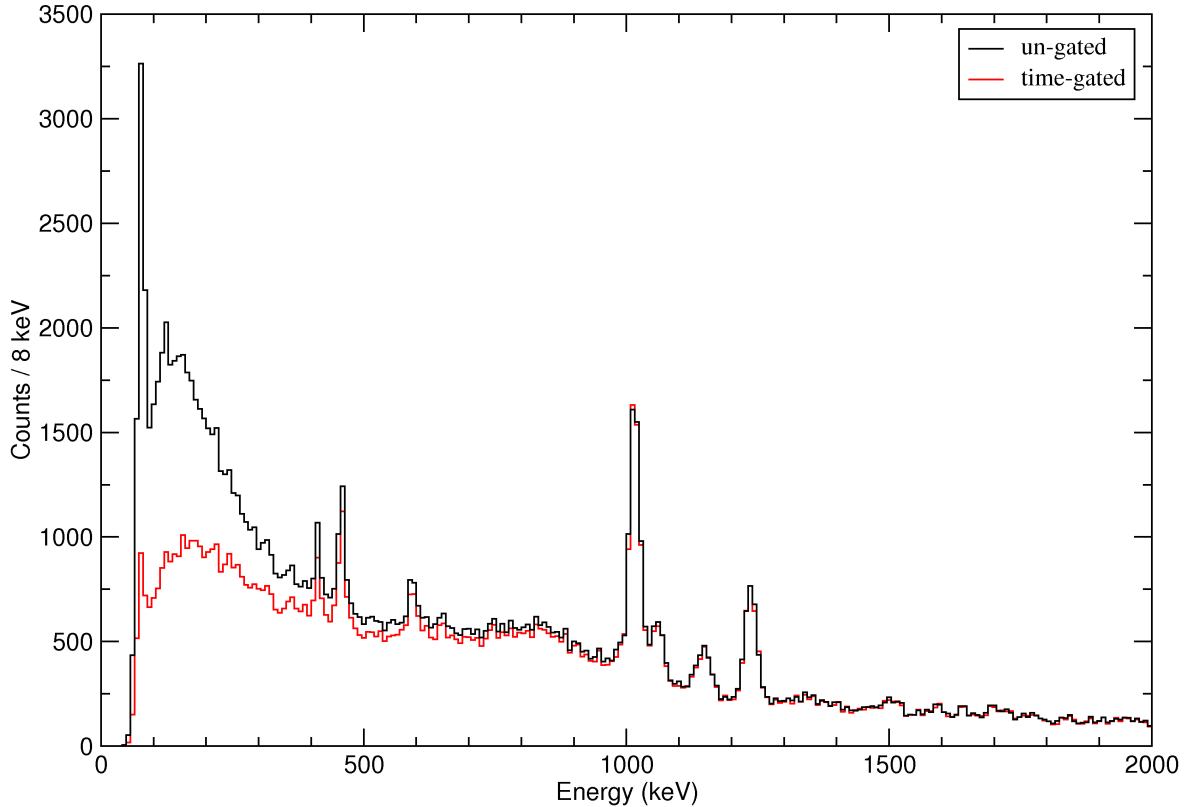


Figure 5.4: Gamma-ray spectrum in coincidence with ^{49}V recoils with additional timing conditions applied. (Original in colour.)

As demonstrated in Section 4.4.3, the effect of the timing conditions is to reduce the *bremsstrahlung* background at low energies, along with low energy peaks, while at higher energy there is little effect. This is what we see here, resulting in complete removal of the 134 keV peak and considerable reduction of the 91 keV transition. With regard to the observation of mirror transitions in ^{49}Fe , the reduction of this peak is acceptable as a small negative MED for the $J^\pi = \frac{5}{2}^-$ state would push such a γ ray to too low an energy to be detectable with SeGA, hence there is little chance of observing such a γ decay with or without these timing conditions. As we shall see in Section 6.3.1, negative MED values are predicted for both the $J^\pi = \frac{5}{2}^-$ and $\frac{3}{2}^-$ analogue states in ^{49}Fe . Furthermore, tentative observation of these states has been reported by Dossat *et al.* [51] through the observation of γ rays at 90 keV and 63 keV following the β -delayed

proton decay of ^{50}Ni .

The peaks at 417, 464 and 598 keV are more prominent relative to the *bremsstrahlung* background, which is particularly appealing as, after the peaks at around 1000 keV, the analogues of these transitions are the most likely candidates for observation in ^{49}Fe .

5.1.2 Spectroscopy of ^{49}Fe

The conditions used above would appear to be suitable to allow observation of mirror transitions in ^{49}Fe , hence these gating conditions are applied to ^{49}Fe residues detected at the focal plane of the S800 and the corresponding γ -ray spectrum produced. Although the statistics are poor, there are a number of candidate peaks in this spectrum. There are of course, insufficient statistics to perform γ - γ analysis, hence in order to identify the peaks this spectrum must be compared to that of ^{49}V . This is shown in Fig. 5.5.

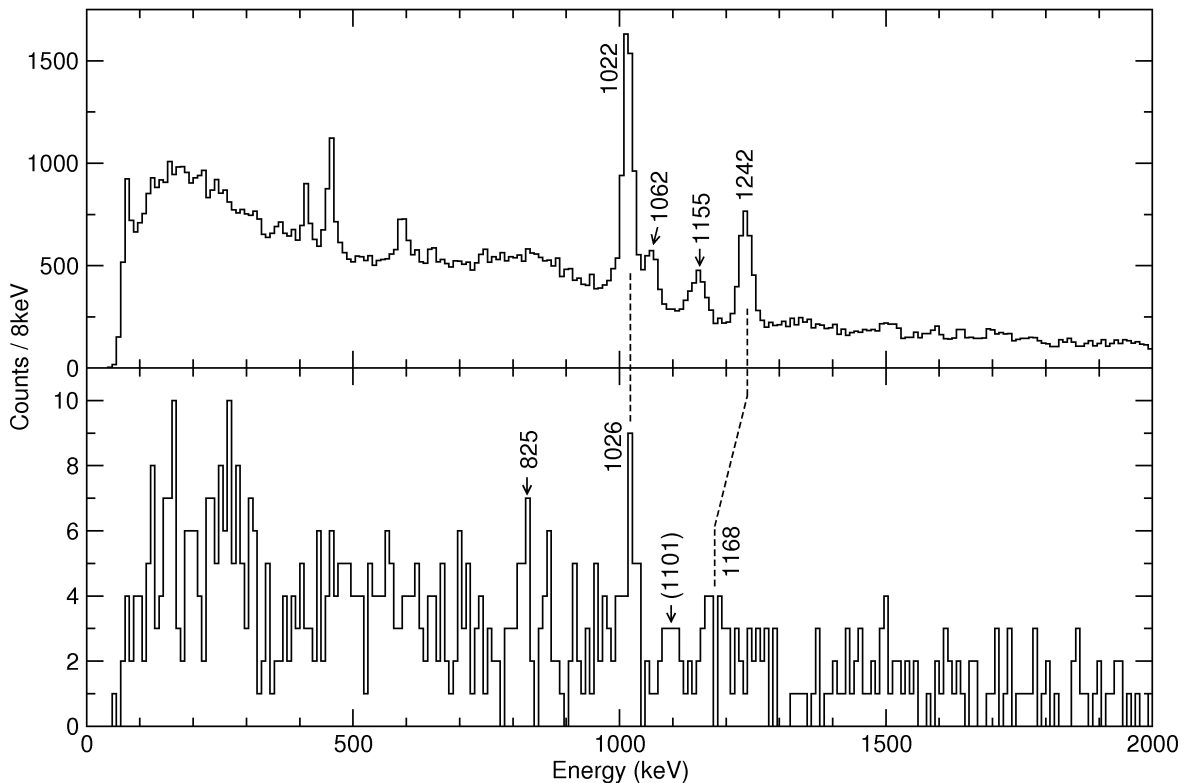


Figure 5.5: Gamma-ray spectra of ^{49}V (top) and ^{49}Fe (bottom) with timing conditions applied. Gamma-ray energies of peaks of interests are labelled and mirrored transitions are indicated.

Mirrored transitions of the two strongest γ decays in ^{49}V (1022 keV and 1242 keV) are evident in ^{49}Fe at 1026 keV and 1168 keV respectively. A third peak maybe present at 1101 keV which could be the mirror transition of either the 1062 or 1155 keV decays.

A further peak is visible at 825 keV with no clear counterpart in the ^{49}V spectrum. The possibility of contamination from strongly populated neighbouring isotopes in the PID must be considered, however, neither ^{48}Mn nor ^{50}Fe have known γ decays from low lying states with energies near 825 keV. Furthermore, there is no evidence of the most intense decays from ^{48}Mn or ^{50}Fe in the ^{49}Fe spectrum, therefore the 825 keV peak must be attributed to ^{49}Fe . The origin of this peak is discussed further in Section 6.3.1. There is some evidence for a peak around 150 keV, however, this lies upon the remnant *bremsstrahlung* background and does not deviate from it significantly.

Due to the extremely low statistics (less than 10 counts per channel) Poisson statistics are used to fit the peaks in order to accurately determine intensities. These are tabulated in Table 5.2, along with the relevant transitions in ^{49}V . The intensity of the 1168 keV transition (relative to the 1026 keV) is in good agreement with the mirrored transition, while the 1101 keV intensity is consistent with both the 1062 keV, 1155 keV or the combination of these, i.e. a doublet. Possible orderings of these γ decays are illustrated in a new level scheme in Fig. 5.6.

Table 5.2: Details of excited states observed in ^{49}Fe , with details of relevant isobaric analogue states in ^{49}V included for comparison. Ground state half-lives for ^{49}Fe and ^{49}V are taken from [51] and [17] respectively.

E_x (keV)	J^π	$t_{1/2}$	E_γ (keV)	$I_{\gamma(rel)}$	E_f (keV)	J^π
					Final State	
^{49}Fe						
0	$\frac{7}{2}^-$	64.7(3) ms				
?	?		825(5)	46(32)	?	?
1026(3)	$(\frac{11}{2}^-)$		1026(3)	100(44)	0	$\frac{7}{2}^-$
?	?		1101(14)	34(19)	?	?
2194(9)	$(\frac{15}{2}^-)$		1168(8)	69(39)	1026	$(\frac{11}{2}^-)$
^{49}V						
0.0	$\frac{7}{2}^-$	329 d				
1021.6	$\frac{11}{2}^-$	3.4 ps	1021.6	100(3)	0.0	$\frac{7}{2}^-$
1155.3	$\frac{9}{2}^-$	1.1 ps	1155.3	18(2)	0.0	$\frac{7}{2}^-$
2263.3	$\frac{15}{2}^-$	0.65 ps	1241.7	53(2)	1021.6	$\frac{11}{2}^-$
3325.2	$\frac{17}{2}^-$		1061.9	26(2)	2263.3	$\frac{15}{2}^-$

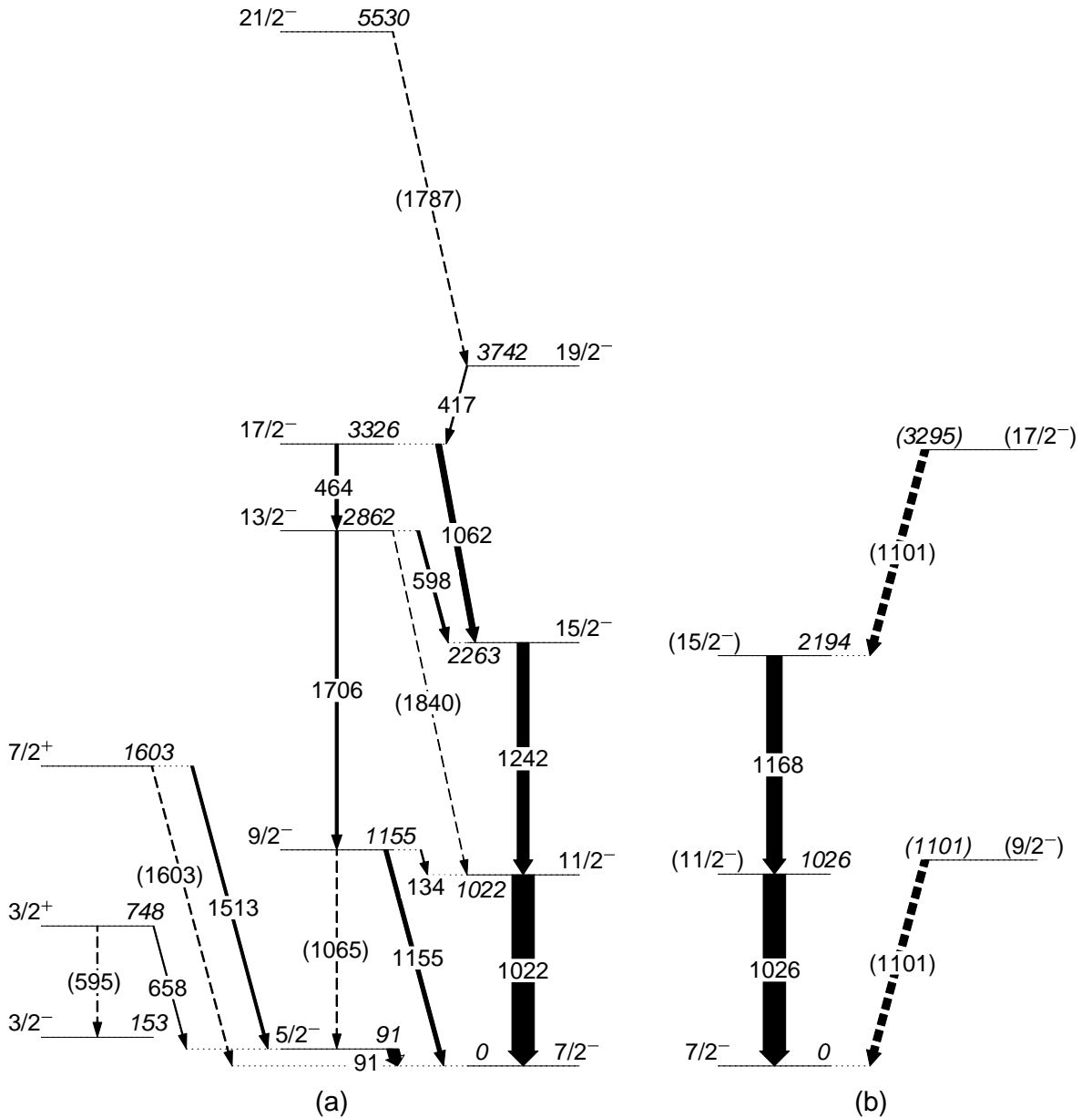


Figure 5.6: (a) Partial level scheme of ^{49}V as observed in this work. All values, except intensities, are taken from [17]. (b) Proposed level scheme for ^{49}Fe constructed based on mirror symmetry arguments. The 1101 keV γ ray could be attributed to decays from two possible states, both of which are displayed tentatively, see text for details. Transition widths are proportional to γ -ray intensities.

5.2 The $A=53$, $T_z = \pm\frac{3}{2}$ mirror pair

5.2.1 Spectroscopy of ^{53}Mn

As for the $A = 49$ mirror pair, the $T_z = +\frac{3}{2}$ member of the $A = 53$ pair shall be considered first in order to determine the optimum gating conditions and identify likely mirrored transitions to search for. Fig. 5.7 shows a γ -ray spectrum in coincidence with ^{53}Mn recoils detected at the focal plane of the S800. Gamma rays are visible up to 2274 keV, which can be attributed to decays from states up to 4384 keV in energy, far beyond the the *yrast* band terminating $J^\pi = \frac{15}{2}^-$ state at 2693 keV. The ordering of these transitions is shown in a level scheme in Fig. 5.8.

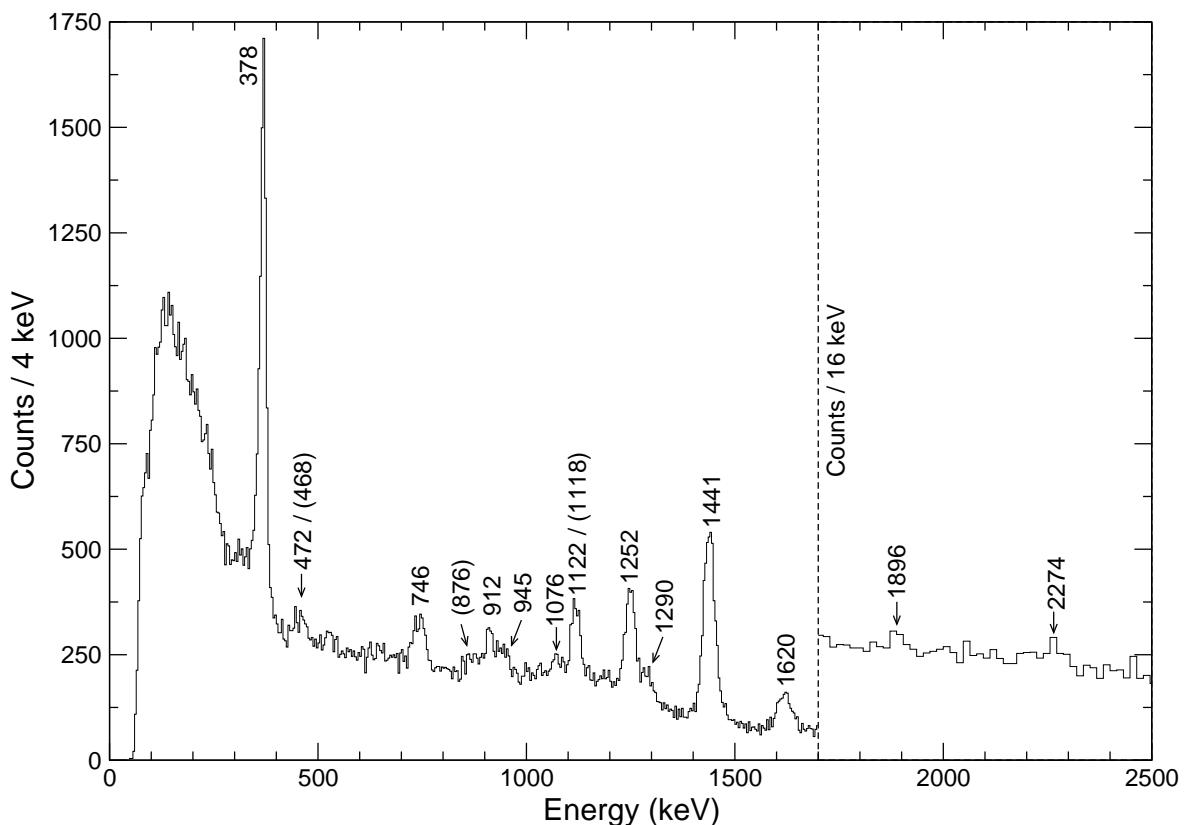


Figure 5.7: Gamma-ray spectrum produced in coincidence with ^{53}Mn recoils detected at the focal plane. Above 1.7 MeV the spectrum has been re-binned to 16 keV/channel to show the weak, high-energy transitions.

The peak at ~ 1120 keV could belong to the 1122 keV $\frac{13}{2}^- \rightarrow \frac{9}{2}^-$ transition or to the 1118 keV $\frac{3}{2}_{(2)}^- \rightarrow \frac{3}{2}_{(1)}^-$ transition, or a combination of both. γ - γ analysis, indicates that the former transition is dominant as can be seen from Fig. 5.9. This spectrum, created in coincidence with the ~ 1120 keV peak, lacks the intense 378 keV peak which we would expect to see in coincidence with the 1118 keV transition following the 912

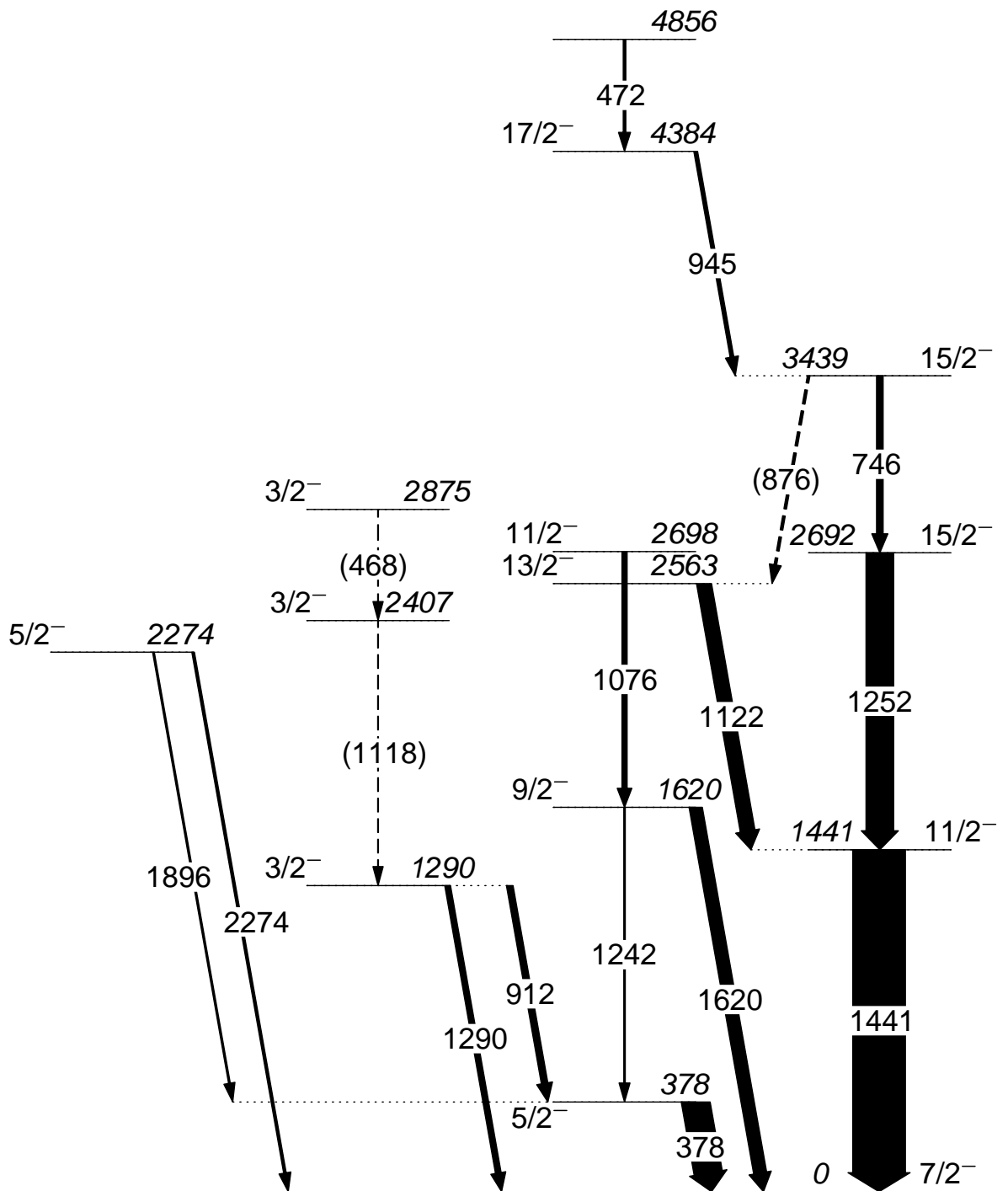


Figure 5.8: Partial level scheme of ^{53}Mn showing the γ -rays and states observed in this work. Transition widths are proportional to measured intensities. Energies, ordering, and spins and parities of states are taken from [52].

keV $\frac{3}{2}^- \rightarrow \frac{5}{2}^-$ decay. Essentially the only remaining peak is the 1441 keV $\frac{11}{2}^- \rightarrow \frac{7}{2}^-$ transition, all we would realistically expect to see in coincidence with the 1122 keV transition given the low intensity of the transitions feeding the $\frac{13}{2}^-$ state in the total spectrum. Considering this, in conjunction with the level scheme in Fig. 5.8, it is clear that the 1122 keV transition is dominant. Furthermore, this implies the peak at ~ 470 keV is mainly the 472 keV decay from a state of unknown spin and parity at 4856 keV which feeds the *yrast* $\frac{17}{2}^-$ state. The 468 and 1118 keV decays are included in Fig. 5.8 for completeness but, for clarity, labelled tentatively. Similarly, a spectrum created in coincidence with the 378 keV decay indicates the presence of the 1242 keV $\frac{9}{2}^- \rightarrow \frac{5}{2}^-$ transition, which in the spectrum of Fig. 5.7, is overwhelmed by the 1252 keV $\frac{15}{2}^-$ to $\frac{11}{2}^-$ decay.

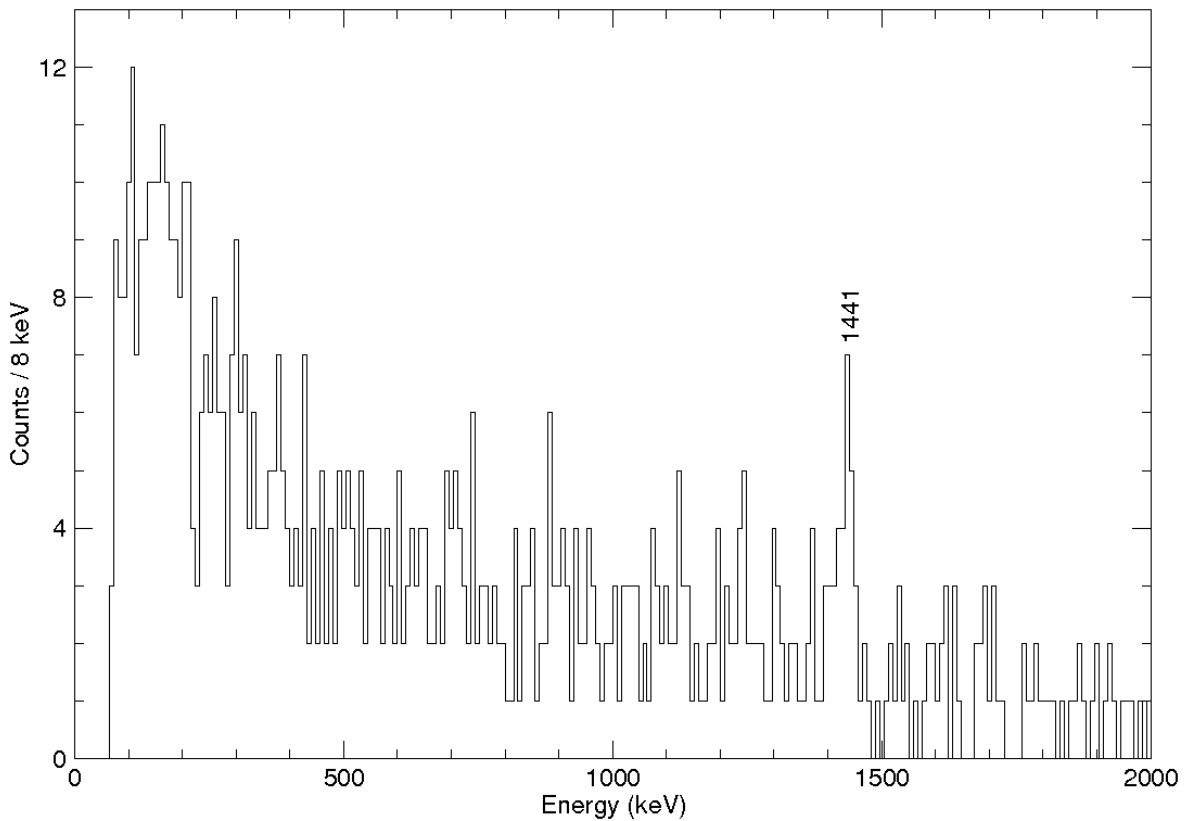


Figure 5.9: Gamma-ray spectrum produced in coincidence with ^{53}Mn recoils and the ~ 1120 keV γ ray. Presence of the 1441 keV peak and absence of the 378 keV peak indicates the ~ 1120 keV peak belongs mainly to the 1122 keV $\frac{13}{2}^-$ to $\frac{11}{2}^-$ transition.

Gaussian fits have been performed on the observed peaks in order to determine the relative intensities of transitions. The results of this fitting, along with other information about the states taken from [52], is tabulated in Table 5.3.

The γ -ray spectrum of ^{53}Mn has a considerable *bremsstrahlung* background. This

Table 5.3: Details of excited states of ^{53}Mn observed in this experiment. All values, except relative γ -ray intensities ($I_{\gamma(rel)}$), are taken from [52].

E_x (keV)	J^π	$t_{\frac{1}{2}}$	E_γ (keV)	$I_{\gamma(rel)}$	E_f (keV)	J^π	Final State
0.0	$\frac{7}{2}^-$	3.74×10^6 yrs					
377.9	$\frac{5}{2}^-$	117 ps	377.9	100(2)	0.0	$\frac{7}{2}^-$	
1289.7	$\frac{3}{2}^-$	0.55 ps	912.0	23(3)	377.9	$\frac{5}{2}^-$	
			1289.7	20(4)	0.0	$\frac{7}{2}^-$	
1441.2	$\frac{11}{2}^-$	0.60 ps	1441.2	184(5)	0.0	$\frac{7}{2}^-$	
1620.1	$\frac{9}{2}^-$	0.48 ps	1241.7	5 ^a	377.9	$\frac{5}{2}^-$	
			1619.9	46(3)	0.0	$\frac{7}{2}^-$	
2273.8	$\frac{5}{2}^-$	0.25 ps	1896.3	6(3)	377.9	$\frac{5}{2}^-$	
			2273.5	9(3)	0.0	$\frac{7}{2}^-$	
2406.9	$\frac{3}{2}^-$	0.11 ps	1117.5	? ^b	1289.7	$\frac{3}{2}^-$	
2562.9	$\frac{13}{2}^-$	10.7 ps	1121.7	52(3) ^b	1441.2	$\frac{11}{2}^-$	
2692.7	$\frac{15}{2}^-$	2.7 ps	1251.5	97(4) ^a	1441.2	$\frac{11}{2}^-$	
2697.7	$\frac{11}{2}^-$?	1076.2	18(3)	1620.1	$\frac{9}{2}^-$	
2875.8	$\frac{3}{2}^-$	41 ps	468.4	? ^c	2406.9	$\frac{3}{2}^-$	
3439.0	$\frac{15}{2}^-$	0.14 ps	746.1	23(2)	2692.7	$\frac{15}{2}^-$	
			875.8	9(2)	2562.9	$\frac{13}{2}^-$	
4384.0	$\frac{17}{2}^-$	0.16 ps	944.7	13(3)	3439.0	$\frac{15}{2}^-$	
4856.0	?	?	472	9(1) ^c	4384.0	$\frac{17}{2}^-$	

^a Doublet. Intensity of the 1242 keV transition taken from [52], relative to the 1620 keV transition.

^b Doublet. 1118 keV transition included for completeness with a nominal intensity.

^c Doublet. 468 keV transition included for completeness with a nominal intensity.

can be reduced by combining the timing conditions and multiplicity requirements described in Section 4.4.3. The resultant spectrum is shown in Fig. 5.10(a), along with a ^{53}Ni spectrum created with identical conditions in (b). The *bremsstrahlung* background in ^{53}Mn has been considerably reduced, greatly enhancing the prominence of low-energy peaks.

5.2.2 Spectroscopy of ^{53}Ni

A number of γ -ray peaks are evident in the ^{53}Ni spectrum in Fig. 5.10(b), the most prominent of which can readily be identified as the analogues of the 378 keV and 1441 keV decays in ^{53}Mn . These correspond to decays from the $\frac{5}{2}^-$ and $\frac{11}{2}^-$ states to the ground state. There is evidence for several smaller peaks, however, due to poor statistics these cannot be confidently identified. Furthermore, given the low intensity of the 1453 keV peak, we would not expect to see any weaker transitions.

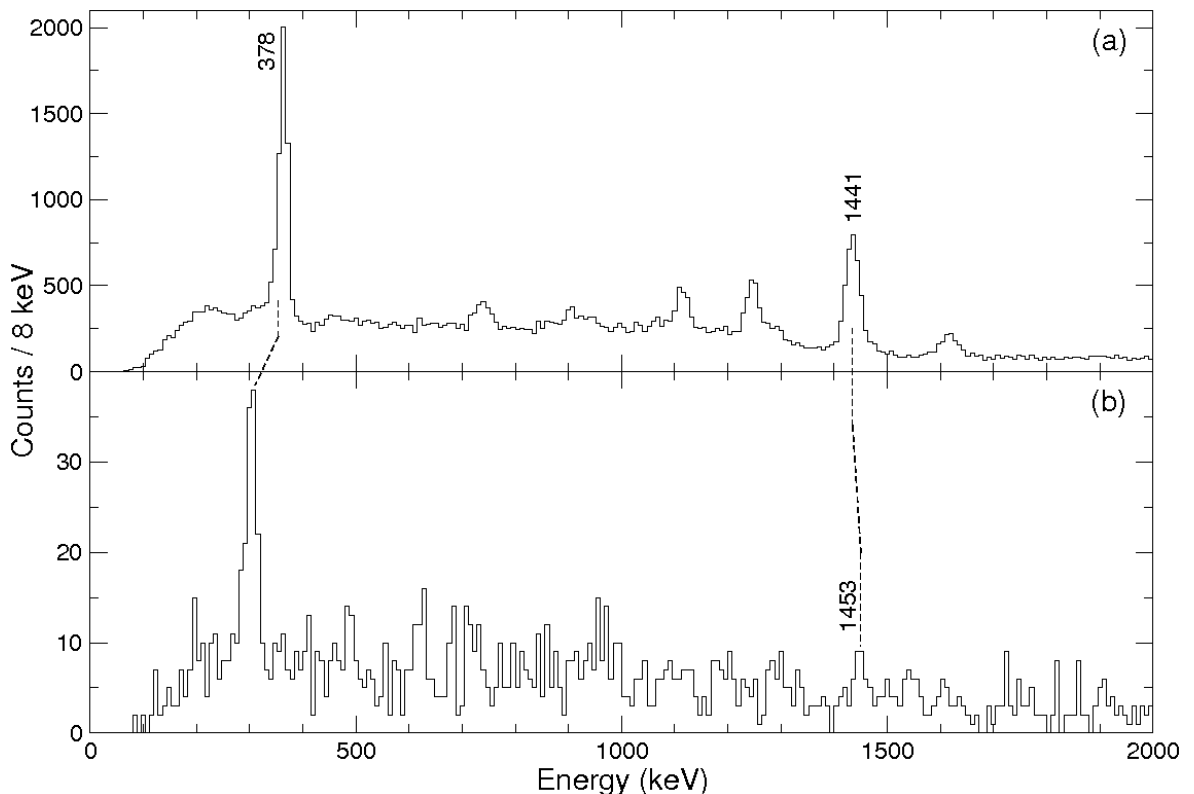


Figure 5.10: (a) ^{53}Mn spectrum created with timing and multiplicity conditions. (b) Gamma-ray spectrum created in coincidence with ^{53}Ni recoils with identical timing and multiplicity conditions as applied to ^{53}Mn . Mirrored transitions are indicated. The energy of the low energy peak is discussed in Section 5.2.3.

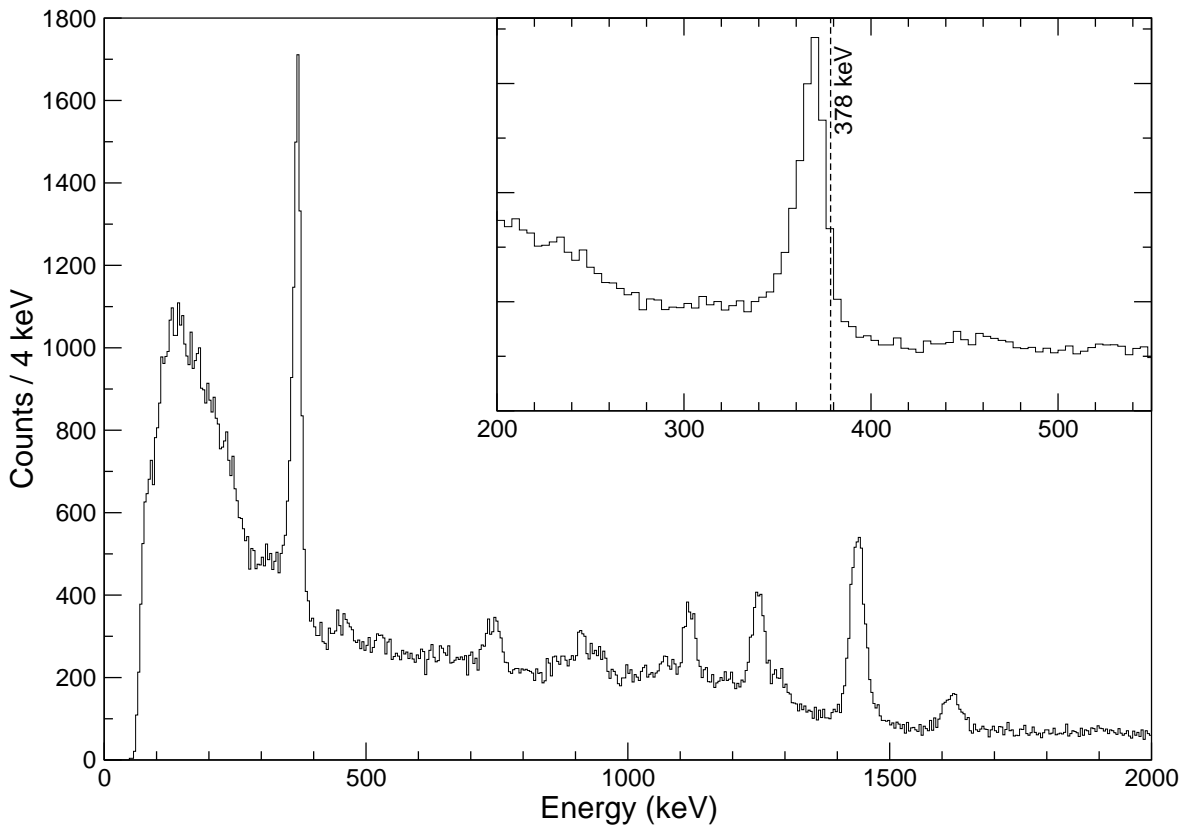


Figure 5.11: ^{53}Mn γ -ray spectrum showing the shift of the 378 keV peak resulting from its 117 ps lifetime.

5.2.3 The $J^\pi = \frac{5}{2}^-$ state

As can be seen from Table 5.3, the $J^\pi = \frac{5}{2}^-$ state at 378 keV in ^{53}Mn has a lifetime of 117 ps. At the relativistic beam velocities used in this experiment ($\sim 0.4c$), this causes the nucleus to decay approximately 2 cm downstream of the target. This results in a change to the effective angles of the two rings of Ge detectors, hence the Doppler correction used for the other γ -ray transitions will shift this peak below its true value to 370 keV, as can be seen in Fig. 5.11. This can be corrected for as the lifetime of the state is well known and the beam velocity after the target can be calculated from that used to optimise the Doppler correction for other states using energy loss codes such as SRIM [53]. The expected position of decay (and the resulting detector angles) can then be calculated simply and adjusted in the Doppler reconstruction calculation (at the expense of the other peaks). Isospin symmetry dictates that the isobaric analogue of this state in ^{53}Ni will have a similarly long lifetime. The decay from this state is evident in Fig. 5.10(b), hence a method must be found to determine the correct energy of the γ decay.

The half-life ($t_{1/2}$) of a state is related to the transition probability (λ) by:

$$t_{1/2} = \frac{\ln 2}{\lambda} \quad (5.1)$$

and the transition probability is given by Fermi's Golden Rule for electromagnetic transitions, i.e.

$$\lambda(\sigma L) = \frac{2(L+1)}{\hbar\epsilon_0[(2L+1)!!]^2} \left(\frac{E_\gamma}{\hbar c}\right)^{2L+1} B(\sigma L) \quad (5.2)$$

This can be expressed in a reduced form as:

$$\lambda(M1) = 1.779 \times 10^{13} E_\gamma^3 B(M1) \quad (5.3)$$

and

$$\lambda(E2) = 1.223 \times 10^9 E_\gamma^5 B(E2) \quad (5.4)$$

for magnetic dipole ($M1$) and electric quadrupole ($E2$) transitions respectively, where $B(M1)$ and $B(E2)$ are reduced transition matrix elements. If we assume that isobaric analogue states have identical reduced transition matrix elements (shell model calculations (see Chapter 6) carried out including isospin breaking effects on the $A = 53$, $T_z = \pm\frac{3}{2}$ system confirm this is a reasonable assumption) then equations (5.1) and (5.3) (or (5.4)) can be combined to express the half-life of a state in ^{53}Ni in terms of its energy and the half-life and energy of the analogue state in ^{53}Mn , i.e.

$$t_{1/2}(^{53}\text{Ni})_{5/2^-} = \left[\frac{E_{\gamma,5/2^-}(^{53}\text{Mn})}{E_{\gamma,5/2^-}(^{53}\text{Ni})}\right]^3 t_{1/2}(^{53}\text{Mn})_{5/2^-} \quad (5.5)$$

for an $M1$ transition, while for an $E2$ transition:

$$t_{1/2}(^{53}\text{Ni})_{5/2^-} = \left[\frac{E_{\gamma,5/2^-}(^{53}\text{Mn})}{E_{\gamma,5/2^-}(^{53}\text{Ni})}\right]^5 t_{1/2}(^{53}\text{Mn})_{5/2^-}. \quad (5.6)$$

Using the half-life of the ^{53}Mn state, a Doppler reconstruction can be calculated to obtain an initial estimate of the energy of the state in ^{53}Ni . This value can then be used to determine two half-lives (for a pure $M1$ or pure $E2$ transition) using equations (5.5) and (5.6). Assuming the analogue states have identical mixing ratios, a weighted average half-life can be calculated using the known mixing ratio for the ^{53}Mn transition (i.e. $\delta(E2/M1) = -0.27$) [54]) and remembering that the proportion of $M1$ and $E2$

radiation is given by $1/(1 + \delta^2)$ and $\delta^2/(1 + \delta^2)$ respectively. This average half-life can now be used to redo the Doppler reconstruction and produce a further estimate of the energy of the $\frac{5}{2}^-$ to $\frac{7}{2}^-$ transition. By iteratively repeating this process the lifetime was found to converge at 199 ps, corresponding to an energy of 320 keV, with a conservative estimate of ± 5 keV. This is illustrated in Fig. 5.12.

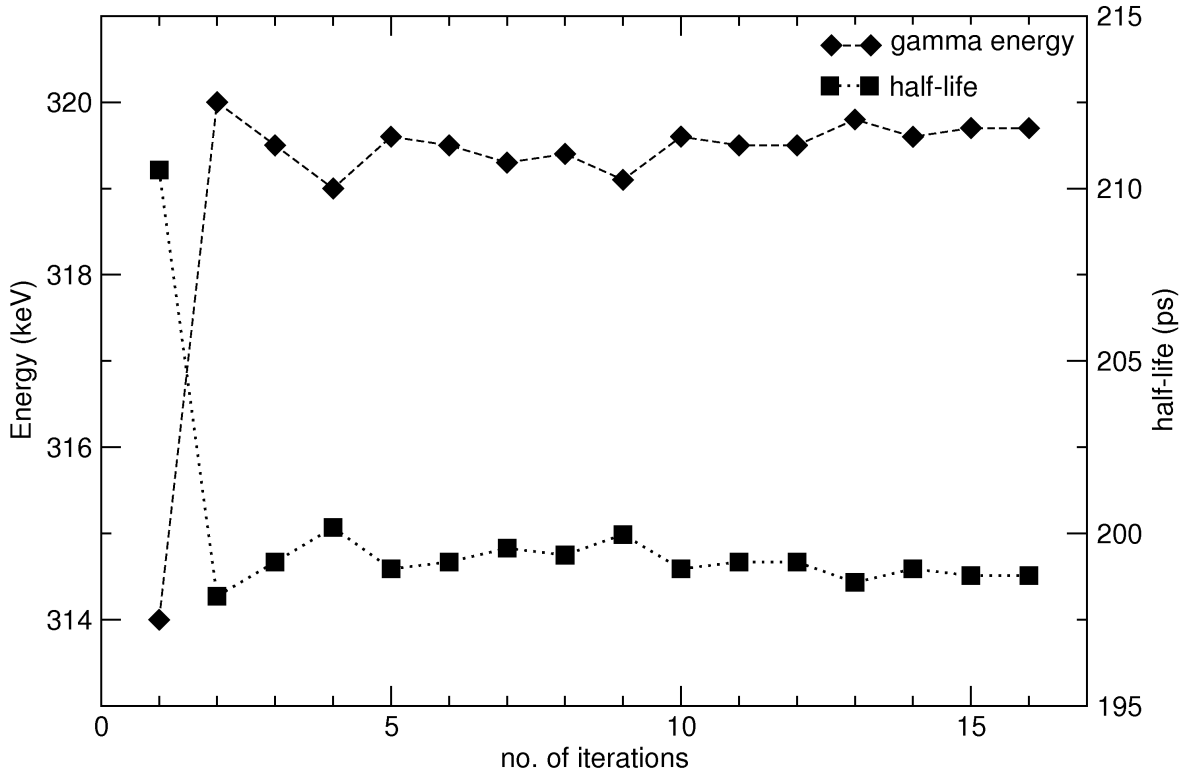


Figure 5.12: Plot demonstrating the iterative process used to determine the energy and half-life of the $J^\pi = \frac{5}{2}^-$ state in ^{53}Ni . With successive iterations the large fluctuations quickly converge, see text for details.

A new level scheme can now be constructed for ^{53}Ni , assigning spins and parities based on mirror symmetry arguments (Fig. 5.13): the details of these transitions are tabulated in Table 5.4 along with isobaric analogue states in ^{53}Mn . Contrary to the expected symmetry, the intensities of the $\frac{11}{2}^-$ to $\frac{7}{2}^-$ transitions differ by a factor of ~ 4 .

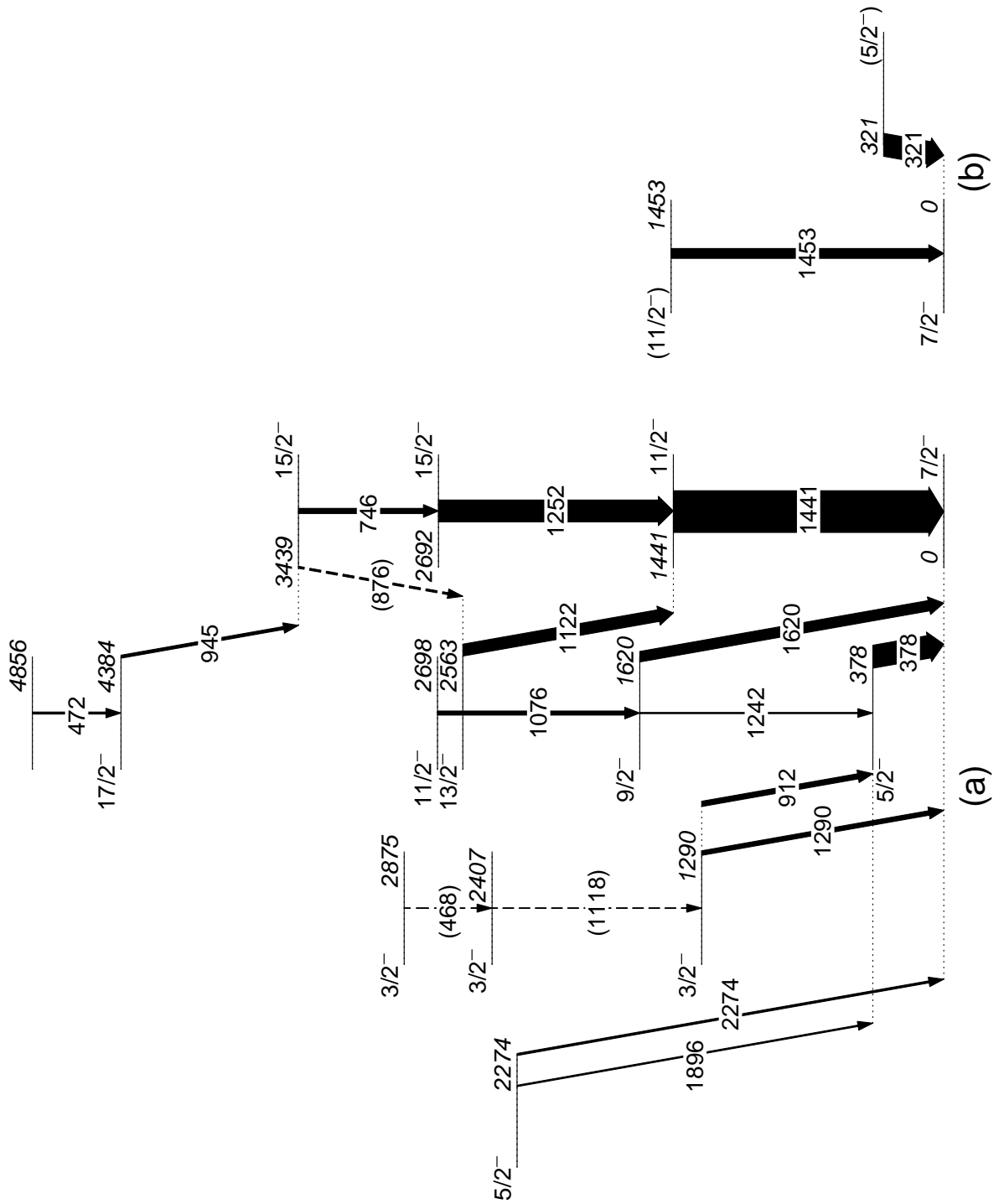


Figure 5.13: (a) Partial level scheme of ^{53}Mn , created as in Fig. 5.8. (b) New level scheme of ^{53}Ni created in this work. Spins and parities are tentative as they are assigned based purely on mirror symmetry arguments. Transition widths are proportional to relative intensities measured in this work.

Table 5.4: Details of new excited states observed in ^{53}Ni , with details of relevant isobaric analogue states in ^{53}Mn included for comparison. Ground state half-life for ^{53}Ni and ^{53}Mn are taken from [51] and [52] respectively.

E_x (keV)	J^π	$t_{1/2}$	E_γ (keV)	$I_{\gamma(rel)}$	E_f (keV)	J^π
					Final State	
^{53}Ni						
0	$\frac{7}{2}^-$	55.2(7) ms				
320(5)	$(\frac{5}{2}^-)$	199 ps	320(5)	100(16)	0	$\frac{7}{2}^-$
1453(6)	$(\frac{11}{2}^-)$?	1453(6)	44(21)	0	$\frac{7}{2}^-$
^{53}Mn						
0	$\frac{7}{2}^-$	3.74×10^6 yrs				
377.9	$\frac{5}{2}^-$	117 ps	377.9	100(2)	0	$\frac{7}{2}^-$
1441.2	$\frac{11}{2}^-$	0.6 ps	1441.2	184(5)	0	$\frac{7}{2}^-$

5.3 Population anisotropies following mirrored fragmentation reactions

As mentioned in Section 4.2, one would naively expect mirrored fragmentation reactions (e.g. removal of two protons or two neutrons from an $N = Z$ beam) to populate isobaric analogue states in mirror nuclei with identical proportions. However, as we have already seen, this may not always be the case—*cf.* 825 keV peak in ^{49}Fe spectrum in Section 5.1.2, and the intensities of the $\frac{11}{2}^-$ to $\frac{7}{2}^-$ transitions in the $A = 53$ mirror pair (see Section 5.2). A further example of this is evident in the case of the $A = 54$, $T_z = \pm 1$ mirror pair, i.e. ^{54}Fe and ^{54}Ni . Gamma-ray spectra of these isotopes have been made as in Sections 5.1 and 5.2, but without additional gating conditions (i.e. multiplicity or timing) to ensure the population of states is not biased in anyway. These spectra can be seen in Fig. 5.14.

In both nuclei, the known [9, 55] $6^+ \rightarrow 4^+ \rightarrow 2^+ \rightarrow 0^+$ *yrast* cascade is dominant, but in the case of ^{54}Fe decays from several non-*yrast* states are also present. The observed states have been collated into level schemes following the ordering of [55] and [9] (see Fig. 5.15). The γ -ray peak observed at ~ 807 keV may originate from the 807 keV $3^+ \rightarrow 4^+$ decay, or the 805 keV $4_3^+ \rightarrow 4_2^+$, or some admixture of these two. Due

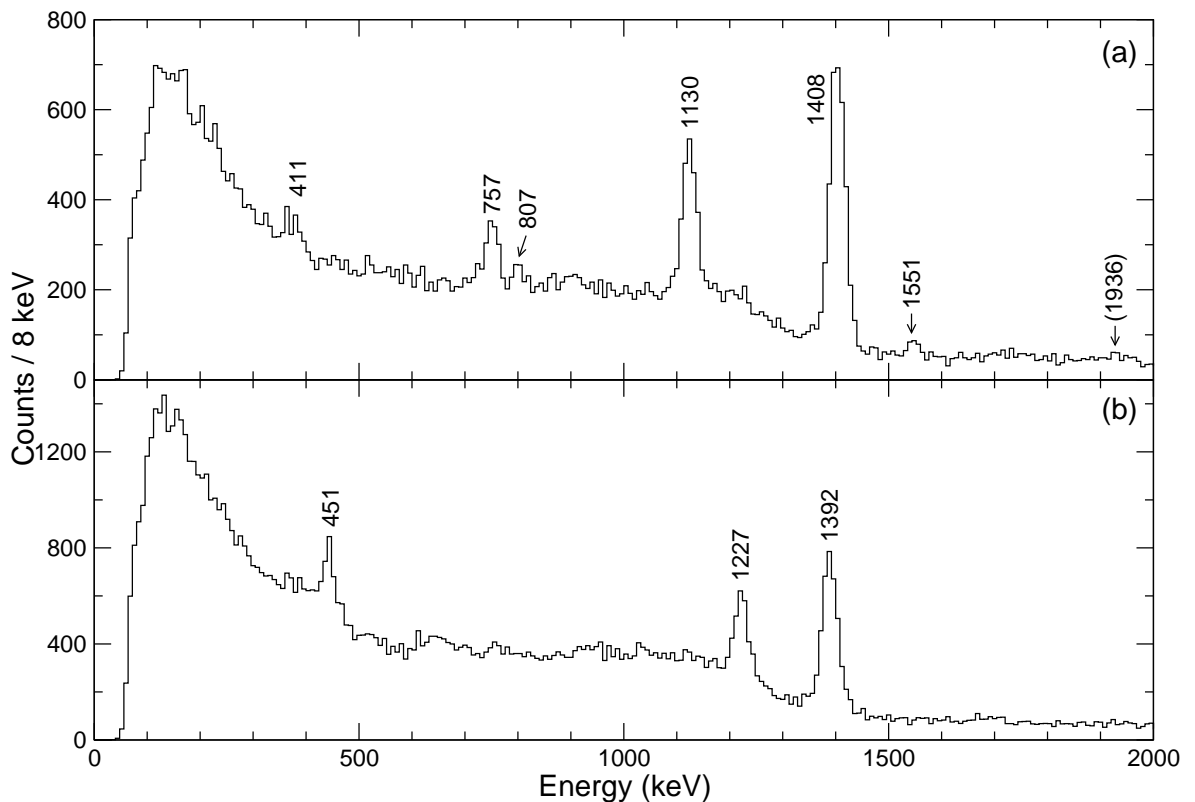


Figure 5.14: (a) Gamma-ray spectrum in coincidence with ^{54}Fe recoils. (b) ^{54}Ni γ -ray spectrum. Both spectra are made without additional gating conditions. The peaks labelled 411 and 451 keV are shifted, as discussed in Sec. 5.3.2.

to the presence of the 1936 keV decay from the 3^+ state, albeit extremely weak, the 807 keV peak has been attributed primarily to the former decay, whilst the latter is included in the level scheme for completeness.

Beyond the simple observation of different states, the most striking asymmetry in this mirror pair lies in the relative intensities of the *yrast* cascade. While the relative intensities of the $4^+ \rightarrow 2^+$ and $2^+ \rightarrow 0^+$ transitions are similar, the $6^+ \rightarrow 4^+$ intensity, in the case of ^{54}Fe , appears to have been transferred to the $4_2^+ \rightarrow 4_1^+$ 757 keV transition. These differences in intensity are quantified in Table 5.5.

Assuming a pure $f_{7/2}$ configuration, a first approximation suggests that the population of states should be proportional to the number of m_J sub-states of the removed pair of nucleons, i.e. $2J + 1$, suggesting the 0^+ , 2^+ , 4^+ and 6^+ states are populated with the ratios $1 : 5 : 9 : 13$. These ratios are significantly modified by the spatial correlations of the nucleons removed [56], essentially resulting in an enhancement of the population of low-spin states and a reduction for higher spins. Furthermore, inclusion of the upper fp shell in the calculations (performed by Jeff Tostevin of the University of Surrey) produces further small corrections to these values resulting in the ratios

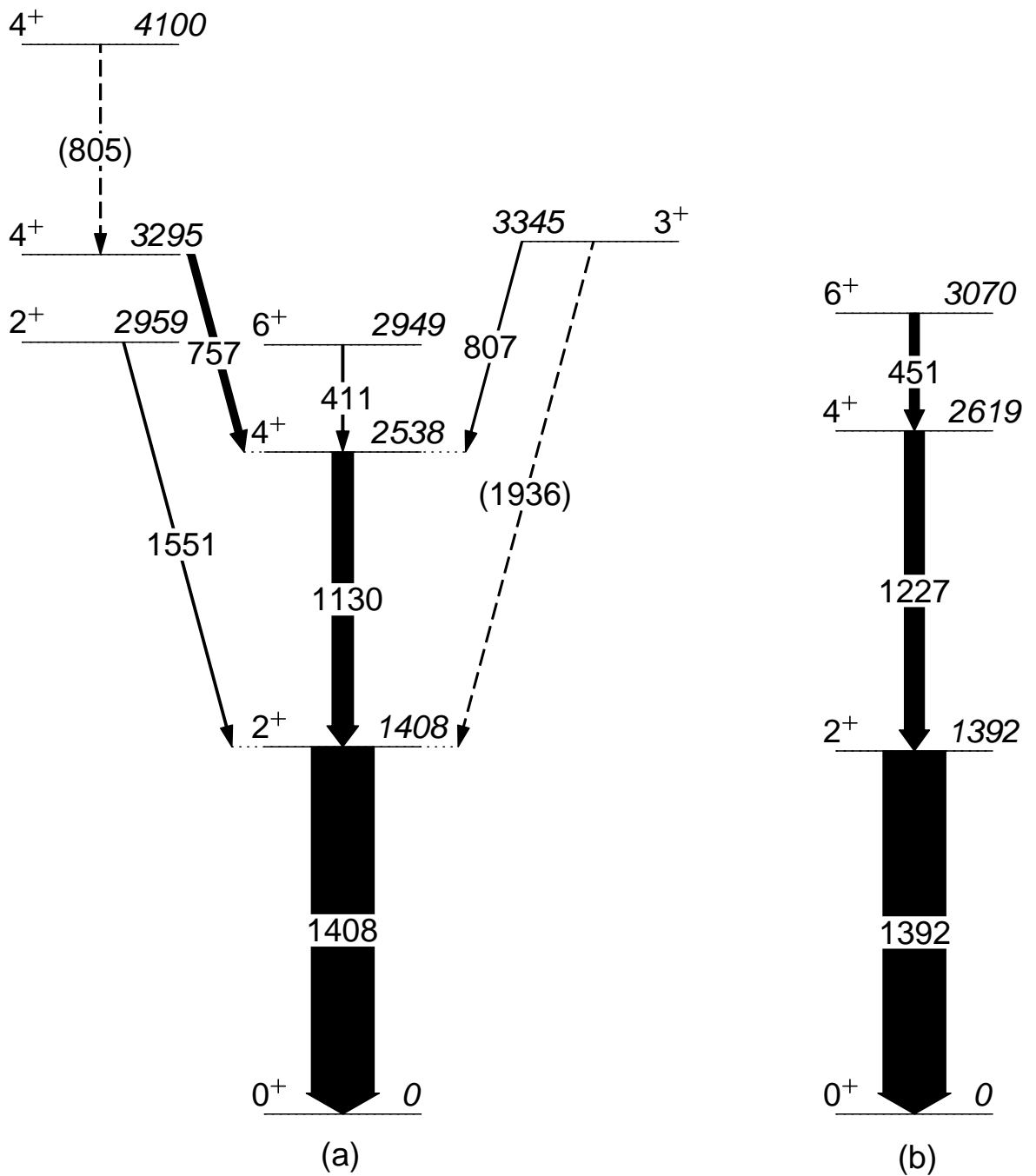


Figure 5.15: Partial level schemes of (a) ^{54}Fe and (b) ^{54}Ni states observed in this work. Energies of γ rays, and the ordering, energies, spins, and parities of states are taken from [55] and [9] for (a) and (b) respectively. Transition widths are proportional to relative γ -ray intensities, measured in this work.

Table 5.5: Details of excited states observed in ^{54}Fe and ^{54}Ni . All values except relative γ -ray intensities are taken from [55] for ^{54}Fe and [9] and [55] for ^{54}Ni .

E_x (keV)	J^π	$t_{1/2}$	E_γ (keV)	$I_{\gamma(rel)}$	E_f (keV)	J^π
					Final State	
^{54}Fe						
0.0	0^+	Stable				
1408.2	2^+	0.8 ps	1408.1	100(3)	0.0	0^+
2538.1	4^+	4.0 ps	1129.9	33.9(2.3)	1408.2	2^+
2949.2	6^+	1.215 ns	411.4	3.4(1.0)	2538.1	4^+
2959.0	2^+	0.052 ps	1550.7	3.1(1.3)	1408.2	2^+
3294.8	4^+		756.6	11.4(1.3)	2538.1	4^+
3344.8	3^+		806.5	2.4(1.1)	2538.1	4^+
			1936.5	2.1(0.8)	1408.2	2^+
4099.7	4^+		804.9 ^a		3294.8	4^+
^{54}Ni						
0.0	0^+	104 ms				
1392	2^+	0.85 ps	1392	100(3)	0.0	0^+
2620	4^+		1227	58.1(3.0)	1392	2^+
3071	6^+		451	15.5(1.5)	2620	4^+

^a This transition cannot be resolved from the 806.5 keV decay which we assume to be dominate due to the presence of the 1936.5 keV transition. This transition is included for completeness with a nominal intensity.

1 : 2.13 : 2.39 : 3.67 [57]. If each of these states decay solely into the state below, the γ -ray peaks associated with these decays should be in the ratios 45 : 74 : 100 for the $6^+ \rightarrow 4^+ : 4^+ \rightarrow 2^+ : 2^+ \rightarrow 0^+$ transitions. Comparison of these values with the relative intensities in Table 5.5 immediately reveals that for both members of the mirror pair, decays from the 4^+ and 6^+ states are weaker than expected. Put another way, the relative intensities of decays from the 4^+ and 2^+ states are stronger than expected, indicating that these states are being additionally fed from elsewhere. This is evident for ^{54}Fe (*cf.* Fig. 5.15 (a)), and closer scrutiny of Fig. 5.14 (b) indicates that other γ rays may be present in the ^{54}Ni spectrum but cannot be clearly identified. Nevertheless, the differences in intensities of these non-*yrast* states are of interest.

5.3.1 Direct vs. indirect reactions

A further consideration relating to the apparent asymmetry in the population of states is the interplay between direct and indirect reactions. Two nucleon removal can proceed via the direct removal of a pair of nucleons, or the knockout of a single nucleon, leaving the residual nucleus in an excited state which then particle decays [58]. The implications of this can be understood with the aid of Fig. 5.16a (supplied by Jeff Tostevin [59]). Energy windows for one- and two-proton removal are shown, constrained by the proton and neutron separation energies, labelled π and ν respectively. The region in blue denotes the window available for one-proton knockout to states above the proton threshold in ^{55}Co , but below the neutron and two-proton thresholds. These states can proton decay to states in ^{54}Fe .

If we now consider Fig. 5.16b, the threshold diagram for neutron removal from ^{56}Ni , we see that the energy region in ^{55}Ni capable of neutron decay to ^{54}Ni is almost 10 MeV above the proton separation energy. This implies proton decay to ^{54}Co is more probable, hence only direct, two-nucleon removal will occur. These rare cases occur in very asymmetric nuclei approaching the proton and neutron driplines and in recent years have become a powerful direct probe of nuclear structure [60, 33, 34]. It is now clear that for ^{54}Ni , only direct two-nucleon removal is energetically favourable, whereas for ^{54}Fe , two reaction methods will compete. The population of states following the indirect reaction are not known in this case (though such calculations are feasible [61]), however, it is likely that this will contribute to the observed asymmetry.

More detailed consideration of the energetics of these reactions yields yet another

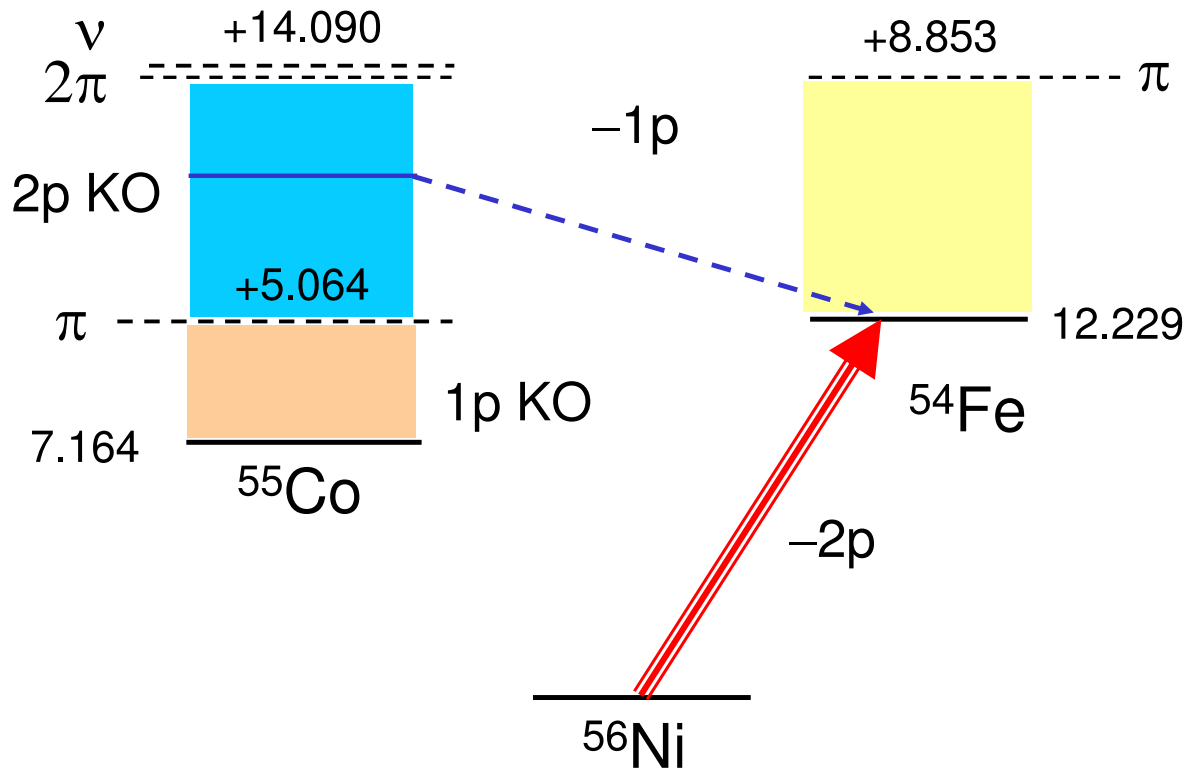
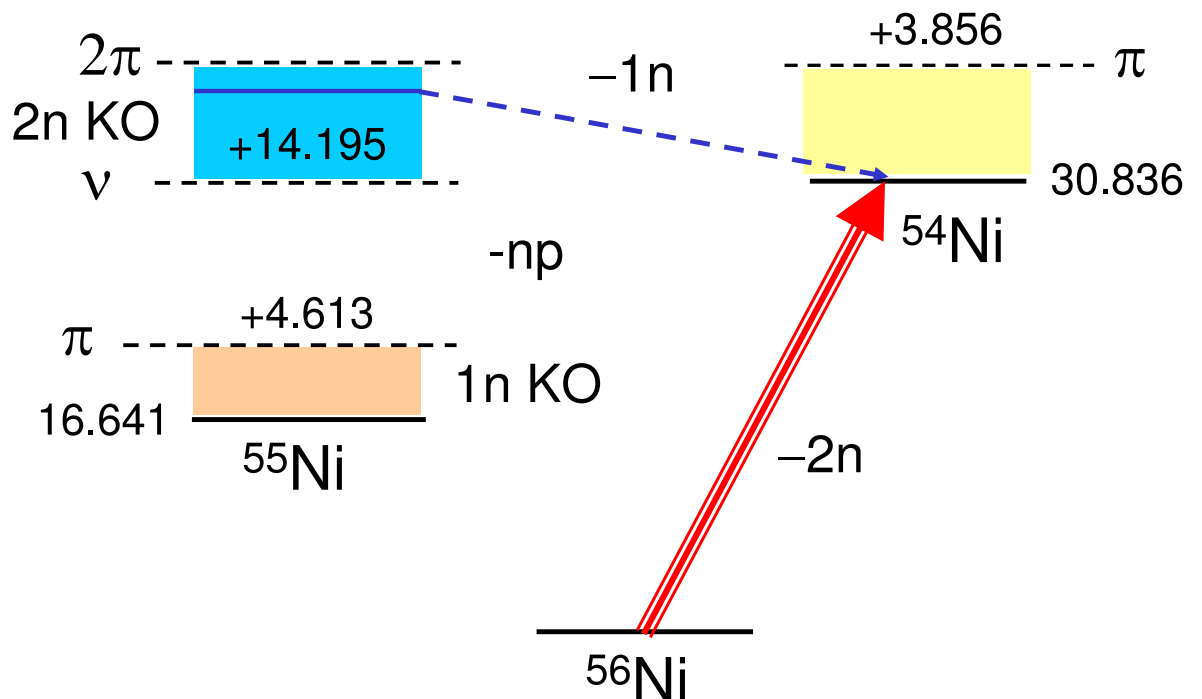
(a) Threshold diagram for proton removal from ^{56}Ni .(b) Threshold diagram for neutron removal from ^{56}Ni .

Figure 5.16: Nucleon removal threshold diagrams for ^{56}Ni , supplied by Jeff Tostevin [59]. The yellow regions represent the energy window for two nucleon knockout, orange regions denote single nucleon removal to bound states, while blue regions show the window for single nucleon removal to unbound states. (Original in colour.)

Table 5.6: Proton (S_π) and neutron (S_ν) separation energies produced in Hartree-Fock calculations for the sub-shells in ^{56}Ni , taken from [59], along with the maximum occupation of each sub-shell (occ.).

	S_π (MeV)	S_ν (MeV)	occ.
$1f_{7/2}$	-6.025	-15.531	8
$2s_{1/2}$	-11.478	-21.280	2
$1d_{3/2}$	-11.114	-20.869	4
$1d_{5/2}$	-15.345	-25.040	6
$1p_{1/2}$	-22.565	-32.480	2

possible contribution to this asymmetry. The results of Hartree-Fock calculations (performed by Jeff Tostevin) of the separation energies for protons and neutrons in the sub-shells of ^{56}Ni are shown in Table 5.6. In ^{56}Ni , these sub-shells (as well as the $1s_{1/2}$ and $1p_{3/2}$ shells below them) are maximally filled with both protons and neutrons. The removal of two protons from the $f_{7/2}$ shell to produce ^{54}Fe will require 12.05 MeV while removal of one $f_{7/2}$ proton and one from either the $s_{1/2}$ or $d_{3/2}$ will require ~ 5 MeV more energy than this. Such a removal will populate negative parity states which we infer, from the separation energies, will be at excitation energies around 5 MeV, and will likely decay through the *yrast* states. Indeed, the lowest-lying negative parity state in ^{54}Fe (i.e. the 3^- state at 4782 keV) is known to decay into the *yrast* states, with the exception of the 6^+ state. The 3^- state also feeds the 3^+ and 4_2^+ states at 3345 and 3295 keV respectively, which in turn decay to the *yrast* 4^+ state, again bypassing the 6^+ . Although the decays from these negative parity states are not observed directly, as the strength is fragmented between a number of possible decay paths and the energies of these transitions are large (typically $\gtrsim 1500$ MeV), such decays will be very hard to observe.

For neutrons, though the binding is considerably greater, removal of one $f_{7/2}$ neutron and one from the $2s_{1/2}$ or $1d_{3/2}$ shells rather than two $1f_{7/2}$ neutrons still requires ~ 5 MeV more energy leading to states around 5 MeV in energy, somewhat above the proton separation energy of 3.86 MeV in ^{54}Ni (see Fig. 5.16b). Despite this, some of these negative parity states may remain bound which could account for some of the other possible γ rays present (but not identified) in Fig. 5.14b, however, it is likely

that most such states will be unbound. This, therefore, provides a second reaction mechanism contributing to the population of ^{54}Fe but not significantly to ^{54}Ni and further explaining the observed population anisotropy.

This work is being continued by Iain Patterson, a new PhD student at York, in collaboration with Jeff Tostevin.

5.3.2 Lifetime of the 6^+ states

It should be noted that the 6^+ state in ^{54}Fe has a half-life of 1.2 ns, as shown in Table 5.5, and hence (as for the $\frac{5}{2}^-$ states in ^{53}Mn and ^{53}Ni) will decay considerably downstream of the target, ~ 15 cm in this case. In this instance, the lifetime is so great that the 411 keV peak is only visible in the forward ring of detectors, even then shifted to 380 keV when a Doppler reconstruction optimised for the other ^{54}Fe *yrast* transitions is used. This may explain some of the missing intensity in the 6^+ to 4^+ transition.

Furthermore, as a first approximation, mirror symmetry would suggest that the 6^+ state of ^{54}Ni should have a lifetime comparable to that of its analogue in ^{54}Fe . However, closer scrutiny of the peaks (as can be seen in Fig. 5.17) reveals that while the 411 keV ^{54}Fe peak is shifted to 380 keV, the 451 keV peak of ^{54}Ni is observed at 447 keV (following Doppler reconstructions optimised for the other *yrast* decays in ^{54}Fe and ^{54}Ni respectively). This implies that the mean lifetime of the ^{54}Ni state is considerably shorter than that of ^{54}Fe . As the *yrast* cascade of ^{54}Ni has been observed, not only by Gadea *et al.* [9], but also by Rudolph *et al.* [62] in a *stopped beam* experiment following the γ decay of the 10^+ isomeric state, we can be confident of the energy of the 451 keV, $6^+ \rightarrow 4^+$ transition in ^{54}Ni . This therefore implies that the half-life of the 6^+ state in ^{54}Ni is an order of magnitude less than that of its isobaric analogue state in ^{54}Fe .

Further to this, by applying analysis techniques similar to that used in Section 5.2.3 we can obtain an estimate of the lifetime of the 6^+ state in ^{54}Ni . By iteratively repeating the Doppler reconstruction with different values for β and z (the assumed average position of the nucleus along the beam axis when the γ ray is emitted), a unique solution can be found which shifts the $6^+ \rightarrow 4^+$ peak to the accepted energy in spectra from both the 37° and 90° rings. These values can then be used to calculate the mean lifetime of the state, relative to the $\frac{5}{2}^-$ state in ^{53}Mn (this state is used rather than the 6^+ state of ^{54}Fe as it is not visible in both ring spectra so the correct values of β and

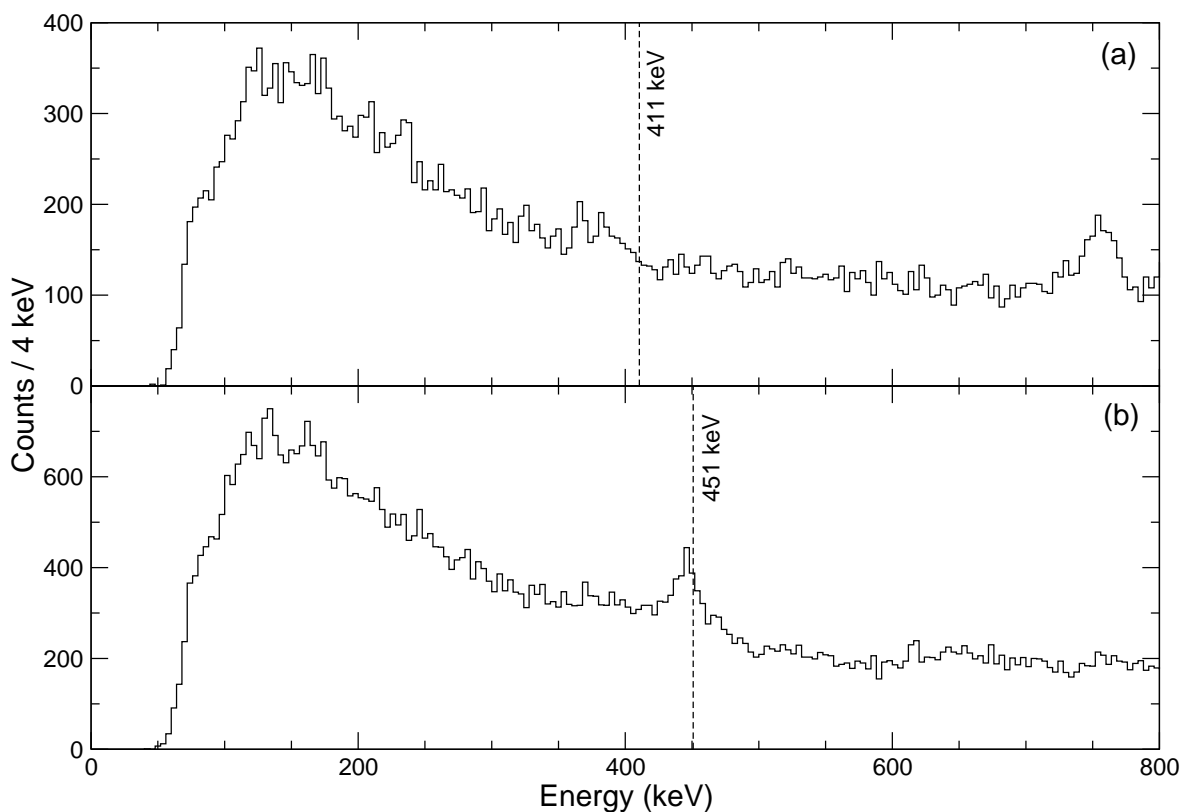


Figure 5.17: Spectra showing the shifts in energy of the γ decays from the 6^+ states of (a) ^{54}Fe and (b) ^{54}Ni .

z cannot be determined, whereas this process has already been performed successfully for the ^{53}Mn state). The result of this process is a half-life of $41 (\pm 18)$ ps for the 6^+ state of ^{54}Ni . Though this error is large (based on extremely conservative estimates of the accuracy to which β and z can be determined), in no way does it account for the factor of almost thirty difference in half-lives of the ^{54}Ni and ^{54}Fe 6^+ states.

As we saw in Eqn. (5.6), if the reduced transition matrix elements for isobaric analogue states are equal, the half-lives of the states and the energies of the γ decays are related by:

$$\frac{t_{1/2}(^{54}\text{Ni})}{t_{1/2}(^{54}\text{Fe})} = \left[\frac{E_{\gamma}(^{54}\text{Fe})}{E_{\gamma}(^{54}\text{Ni})} \right]^5 \quad (5.7)$$

for pure $E2$ transitions. From this we would expect the half-life of the 6^+ state in ^{54}Ni to be approximately $3/5$ that of the ^{54}Fe state, as opposed to $1/30$, as observed above.

One complication to this observation is evident when we consider the ^{54}Ni spectra before the Doppler correction is applied (see Fig. 5.18). In these spectra we can see the broad origins of the ^{54}Ni peaks of interest, along with several sharp peaks from stationary sources. From Eqn. 4.6, we can calculate the energy of the 451 keV peak in the laboratory frame, as it was detected in the 37° ring. This is approximately 602 keV

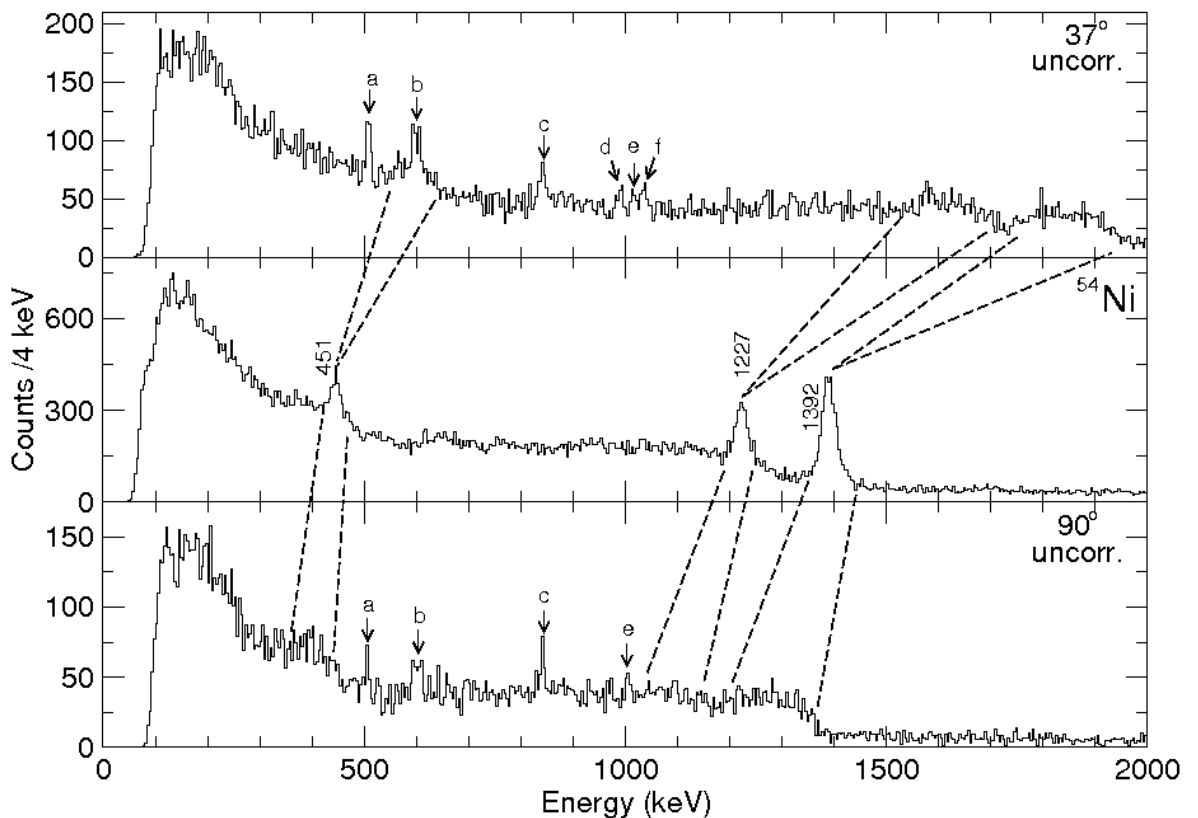


Figure 5.18: ^{54}Ni spectra before the Doppler correction is applied for the 37° (top) and 90° (bottom) detector rings, with the Doppler corrected spectra from all detectors (middle). The ^{54}Ni transitions of interest are labelled, and the origins of these peaks in the uncorrected spectra are indicated. Several additional peaks are evident in the uncorrected spectra which must originate from stationary sources, see text for details.

and corresponds to a prominent peak in the 37° ring spectrum. Due to the considerable angular size of the detector we would expect this uncorrected peak to be extremely broad, as observed for the high energy peaks (1227 and 1392 keV). Furthermore, this ~ 602 keV peak is visible in the 90° ring spectrum also, indicating that it must originate from a stationary source.

Further inspection of the uncorrected spectra reveals a variety of peaks which can be attributed to γ decays following inelastic neutron scattering and radiative neutron capture reactions (i.e. $(n, n'\gamma)$ and (n, γ)) with Ge and Al isotopes present in the detectors and surrounding material. These peaks are more prevalent in the 37° ring than the 90° , indicating the forward focussed nature of the neutrons produced in the reactions. The ~ 602 keV γ -ray peak is in fact a doublet of the 596 and 608 keV decays from the first two 2^+ states in ^{74}Ge ; the relative abundances of Ge isotopes are tabulated in Table 5.7. The former γ -ray is produced in the $^{74}\text{Ge}(n, n'\gamma)$ reaction, with some contribution from the $^{73}\text{Ge}(n, \gamma)$ reaction. This γ -ray is often used as an

indicator to the presence of neutrons as the ${}^{74}\text{Ge}(n, n'\gamma)$ cross section is the largest amongst stable Ge isotopes (for $1.75 < E_n < 2.55$ MeV neutrons) [63]. The origin of other observed neutron-induced γ rays are listed in Table 5.8 (taken from [64]). These transitions are also observed in the uncorrected spectra of many other isotopes, but are absent (or very much reduced relative to the 511 keV transition) in the spectra of isotopes produced without the emission of any neutrons (i.e. the $N = 28$ isotones) suggesting they come directly from the reaction. Furthermore, application of stringent timing conditions does not reduce the intensity of these peaks, as would be expected if they originated from scattered neutrons not time-correlated with the reaction fragments detected at the focal plane.

Table 5.7: Relative isotopic abundances in natural Ge.

Isotope	Abundance (%)
${}^{70}\text{Ge}$	20.37(18)
${}^{72}\text{Ge}$	27.31(26)
${}^{73}\text{Ge}$	7.76(8)
${}^{74}\text{Ge}$	36.73(15)
${}^{76}\text{Ge}$	7.83(7)

The presence of the background peaks at 596 and 608 keV will contaminate the 451 keV peak in the Doppler corrected ${}^{54}\text{Ni}$ spectrum, leading to an overestimate of the intensity. This additional intensity could be estimated from the height of the uncorrected peak and subtracted from the intensities quoted previously, however a greater concern is the effect on the lifetime measurements. There is no doubt that this background will contaminate the attempted lifetime measurement, however it is not clear exactly how this will be manifested. Nevertheless, a sharp, stationary peak (or pair of peaks) in the uncorrected spectrum will be spread out when the Doppler correction is applied (due to the different segment angles in the detectors), whereas γ rays from a moving source, detected at a range of energies due to the different segment angles, will be brought together into a sharp peak. The extent of this broadening/narrowing can be seen by considering the 511 keV peak in Fig. 5.18 which, upon Doppler correction, is completely removed. Applying small variations in β and the detector angles (as was

Table 5.8: Table identifying the origin of various γ -ray background peaks observed in this work, taken from [64]. Letters refer to peaks labelled in Fig. 5.18.

Peak	Energy (keV)	Process
a	511	e^-e^+ annihil.
b	595.9	${}^{74}\text{Ge}(n, n'\gamma)$
		${}^{73}\text{Ge}(n, \gamma)$
	608.3	${}^{73}\text{Ge}(n, \gamma)$
c	843.8	${}^{27}\text{Al}(n, n'\gamma)$
		${}^{76}\text{Ge}(n, n'\gamma)$
	846.9	${}^{76}\text{Ge}(n, n'\gamma)$
d	993.7	${}^{74}\text{Ge}(n, n'\gamma)$
e	1014.5	${}^{27}\text{Al}(n, n'\gamma)$
f	1040.1	${}^{70}\text{Ge}(n, n'\gamma)$

done in determining the lifetime of the 6^+ state) is unlikely to alter this situation. Furthermore, it may be that the intrinsic width of the ~ 602 keV doublet will result in a somewhat sharper peak after Doppler correction than the 511 keV peak. Nevertheless, although the absolute value of the ${}^{54}\text{Ni}$, $J^\pi = 6^+$ state half-life must be treated with some scepticism, the implication that it is significantly shorter than that of the analogue state in ${}^{54}\text{Fe}$ remains valid, and of great interest. This surprising result shall be discussed further in Section 6.3.3 with the aid of shell model calculations.

Chapter 6

Shell-model calculations in the $f_{7/2}$ shell

The new excited states presented in Chapter 5 allow the calculation of mirror energy differences for $T = \frac{3}{2}$ states in the $f_{7/2}$ shell for the first time. In the following chapter, these MED are compared to shell-model calculations, incorporating Coulomb and nuclear isospin-breaking forces, performed as part of this thesis work. In preparation for this, the methods of performing these calculations are described.

6.1 Principles of shell-model calculations

In order to perform realistic shell-model calculations a good valence space must first be selected (with a corresponding inert core). We then construct a series of basis states with pure configurations (e.g. $\pi(f_{7/2})^4 \otimes \nu(f_{7/2})^4$) which will ultimately mix to produce the real states. The wavefunctions of these states must then be expressed as linear combinations of Slater determinants for protons and neutrons independently. These linear combinations are determined by diagonalising a Hamiltonian matrix with dimensions the same as the number of basis states. It is this diagonalisation which is the core task of shell-model codes.

The code ANTOINE [65, 66, 67] is an m -scheme shell-model code which utilises the Lanczos algorithm [67, and references therein] for diagonalisation. This enables it to deal with extremely large matrices, as required for an accurate description of fp -shell nuclei.

6.1.1 Effective interactions

As described in Section 1.2, the key to shell-model calculations is selection of an appropriate model space and corresponding interaction, which forms the Hamiltonian described above. This Hamiltonian consists of kinetic energy operators and two-body interactions, i.e. single-particle energies and two-body matrix elements. For nuclei in the $f_{7/2}$ shell, the doubly-magic nucleus ^{40}Ca is an appropriate core with the full fp model space. (The exception to this is for light nuclei at the bottom of the shell with $A \lesssim 46$, where excitations from the sd -shells can play an important role.) Several interactions are available in this space such as KB3G [68], GXPF1 [69, 70] and FPD6 [71]. In the following calculations the KB3G interaction is used throughout, though calculations carried out with the GXPF1 interaction were found to be consistent with equivalent KB3G calculations.

6.1.2 Truncations

Practical shell-model calculations are limited by the size of the matrices which can be handled, hence in order to deal with large configuration spaces, truncations must be applied to limit the size of the valence space to a manageable size. This is achieved primarily by limiting the number of nucleons allowed into each sub-shell. For nuclei in the $40 \leq A \leq 56$ mass range we could limit our valence space to a pure $f_{7/2}$ configuration, however calculations carried out in this way do not produce results consistent with experimental observations. Some particles must therefore be allowed to be excited into the upper fp orbitals in order to accurately reproduce the real wave functions. The minimum number of excitations (t) required to give realistic results can be determined by plotting the evolution of relevant parameters (such as excitation energy) versus t and observing where convergence occurs. An example of this is seen in Fig. 6.1, which demonstrates that in the $A = 53$ case, good agreement is achieved by $t = 5$.

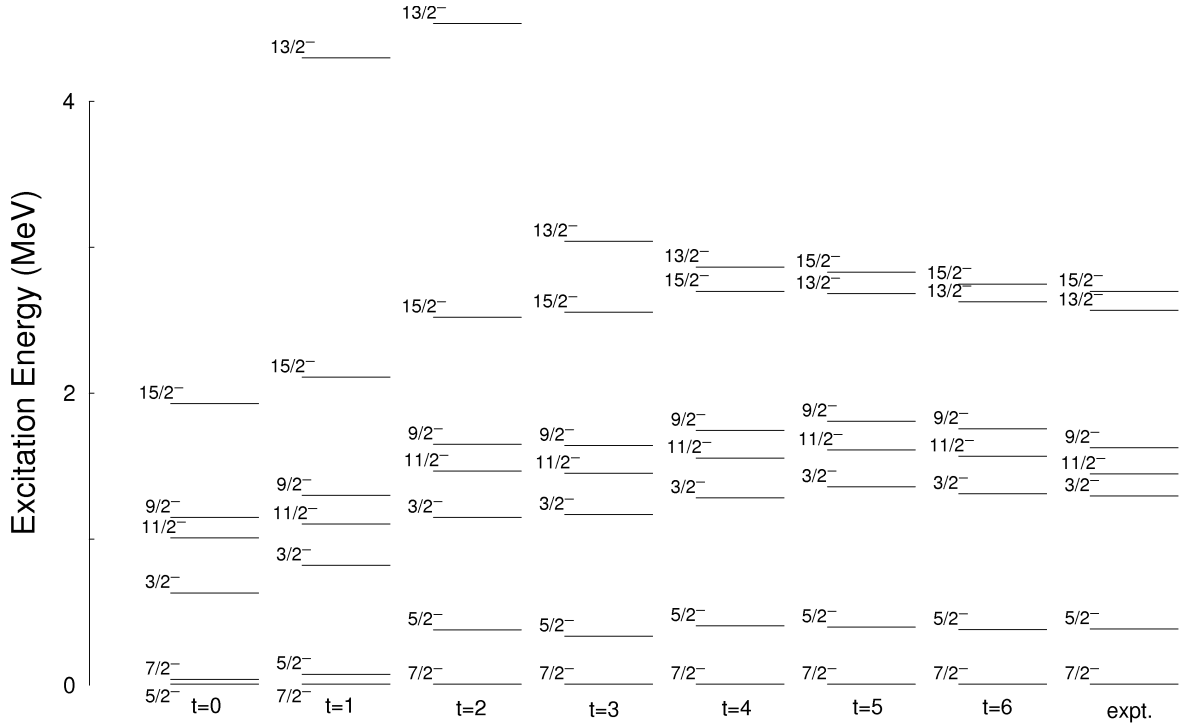


Figure 6.1: Theoretical and experimental energy levels for ^{53}Mn , showing the evolution of theoretical levels with t , i.e. the number of excitations allowed to the upper fp shell. Note that a $J^\pi = 13/2^-$ state cannot be made from a pure $\pi(f_{7/2})^{-3}$ configuration, hence is not present in the $t = 0$ scheme. Theoretical energies converge towards experimental values, reaching good agreement by $t = 5$.

6.2 Calculations of isospin-breaking terms

Several of the isospin-breaking phenomena discussed in Section 1.3.3 can be readily amalgamated into standard shell model calculations. In the case of the monopole single-particle effects, this is achieved simply by adding the shifts in single-particle energies calculated with Eqs. (1.14) and (1.15), to the single-particle energies in an existing interaction. The Coulomb multipole term is incorporated similarly through inclusion of Coulomb matrix elements calculated using a harmonic oscillator potential (as described in Section 1.3.3), which are added to existing two-body matrix elements to produce a Coulomb dependent interaction. Calculations undertaken with such an interaction are labelled V_{CM} . By undertaking two such calculations with reversed numbers of protons and neutrons and subtracting one from the other, we can determine the Coulomb multipole and single-particle contributions to the MED, i.e.

$$\Delta V_{CM}(J) = E_{CM}(J)_{T_z=-T} - E_{CM}(J)_{T_z=+T}. \quad (6.1)$$

Other isospin breaking contributions require more specific additions to the normal shell-model calculation process and are described below.

Coulomb monopole calculations: The radial term

In the $f_{7/2}$ shell, it has been observed that occupation of the $p_{3/2}$ shell varies with spin, whereas the $p_{1/2}$ occupation is comparatively small and fairly constant (see Fig. 6.2). As the radius depends only on l (small l orbitals have larger radii [8], see Section 1.3.3), the $f_{5/2}$ occupancy can also be ignored, hence it is reasonable to consider only the total occupation (protons *and* neutrons) of the $p_{3/2}$ shell. As calculations are performed in the fp valence space, with no consideration of the core, the monopole effects of this radial change must be dealt with explicitly to account for the interaction with the charged core.

This is achieved simply by calculating the total occupation of the $p_{3/2}$ orbital (a quantity which is directly calculated in shell-model codes) for the states of interest. The change in occupation relative to the ground state is then calculated and the contribution to the MED from the radial Coulomb monopole term (ΔV_{Cr}) is determined by multiplying by the appropriate coefficients, i.e.

$$\Delta V_{Cr}(J) = \alpha_r |T_z| \left[m_{p_{3/2}}(g.s.) - m_{p_{3/2}}(J) \right], \quad (6.2)$$

where $m_{p_{3/2}}$ is the total occupation number of the $p_{3/2}$ orbital (obtained directly from the shell-model calculation) and α_r is the strength of the interaction. In ref. [11], a value of 200 keV was found to reproduce experimental energy differences across the $f_{7/2}$ shell, hence this value is used in the following calculations.

Nuclear isospin breaking: The ‘ $J = 2$ ’ anomaly

As we saw in Section 1.3.3, nuclear isospin breaking components can have as significant a contribution to MED as Coulomb effects. Zuker *et al.* [8] found that this can be dealt with most simply by only considering the largest ($J = 2$) contribution, with surprising efficacy. This is achieved through a perturbative approach, i.e. calculating the states of interest with a standard interaction (with or without the addition of Coulomb matrix elements and single-particle effects), then running a single iteration with a *dummy* interaction to determine the expectation value of the $J = 2$, $f_{7/2}$ two-

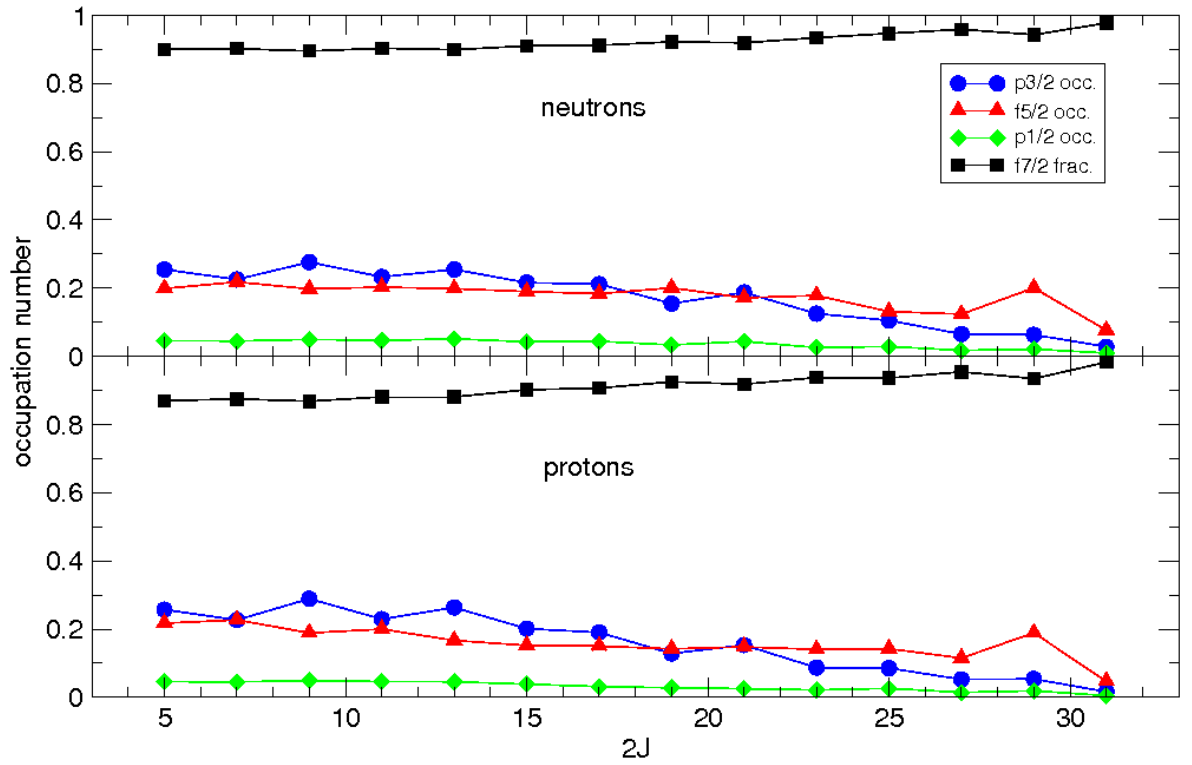


Figure 6.2: Proton and neutron occupation numbers in ^{49}Cr for the $p_{3/2}$, $f_{5/2}$, and $p_{1/2}$ orbitals, with the fractional occupation of the $f_{7/2}$ shell, e.g. $m_{\pi f_{7/2}}/4$. Note that the $p_{1/2}$ occupation is negligible and the $f_{7/2}$ occupation increases, with a corresponding decrease in $p_{3/2}$, as the band termination at $J^\pi = \frac{31}{2}^-$ is approached. (Original in colour.)

proton coupling for each state (this interaction consists of a value of 1 for the $J = 2$, $T = 1$, $T_z = -1$ matrix element, with null values for all other matrix elements and single particle energies). The nuclear isospin breaking contribution to the MED can then be calculated as

$$\Delta V_B(J) = \alpha_B \times \left[(\varepsilon_{\pi f_{7/2}}^{J=2}(J)_{T_z=-T} - \varepsilon_{\pi f_{7/2}}^{J=2}(J)_{T_z=+T}) - (\varepsilon_{\pi f_{7/2}}^{J=2}(g.s)_{T_z=-T} - \varepsilon_{\pi f_{7/2}}^{J=2}(g.s)_{T_z=+T}) \right] \quad (6.3)$$

where $\varepsilon_{\pi f_{7/2}}^{J=2}$ is the expectation value of a pair of $f_{7/2}$ protons coupled to $J = 2$ for a state of given J , T and T_z , and α_B is the strength of the nuclear isospin breaking interaction for $J = 2$. Here we follow the approach of Zuker *et al.* in using an approximate value of 100 keV. In doing this we are taking the step of attempting to account for an interaction in the fp shell purely in terms of $f_{7/2}$ matrix elements, however, as our information on the strength of V_B is taken from the $A = 42$ and 54 mirror pairs this is unavoidable, and turns out to be quite effective.

6.3 Results of shell-model calculations

The contributions to the MED described above are summed for each state of interest in a mirror pair and plotted as a function of spin. Comparison of these calculations with experimentally determined MED can allow insight into the evolution of the structure of excited states, as well as providing a test of the shell model and the isospin-breaking calculations performed with it.

6.3.1 The $A=49$ mirror pair

Figure 6.3 shows the results of isospin-breaking components calculated for the *yrast* states of the $A=49$, $T_z = \pm\frac{3}{2}$ mirror pair, as described in Sec. 6.2. These calculations were performed in the full *fp* space (i.e. $t=9$), though it was found that virtually indistinguishable results can be obtained with a truncation of $t=7$.

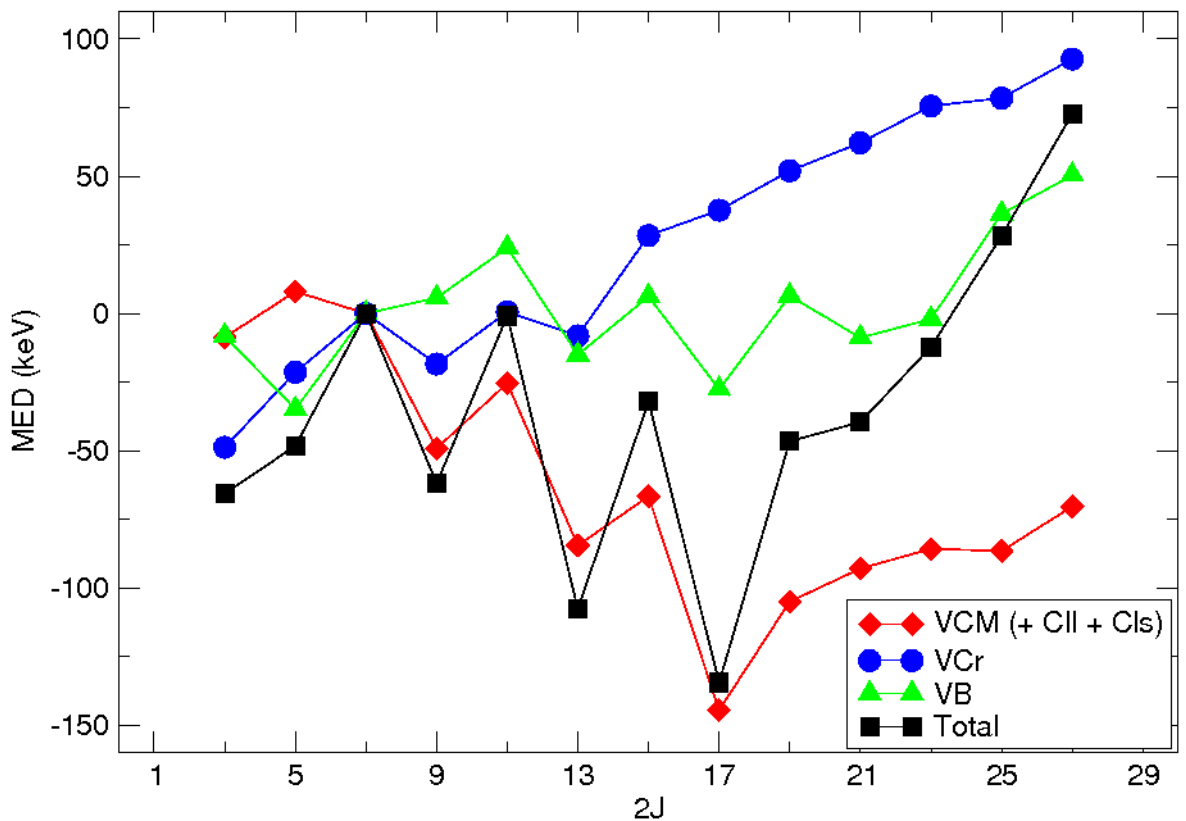


Figure 6.3: Contributions to the $A = 49$, $T_z = \pm\frac{3}{2}$ MED from individual isospin-breaking terms, along with the resultant predicted MED curve. See text for details. (Original in colour.)

The monopole radial term

The monopole radial component is seen to increase smoothly with spin, similar to that of the $A=49$, $T_z = \pm\frac{1}{2}$ mirror pair [11], with the addition of a slight staggering between $J^\pi = \frac{7}{2}^-$ and $\frac{15}{2}^-$. The maximum value reached is somewhat greater here than for the $T_z = \pm\frac{1}{2}$ pair as a result of the $|T_z|$ dependence of this term (*cf.* Eqn. 6.2). This results from a gradual reduction in the occupation of the $p_{3/2}$ orbital in both members of the mirror pair, which produces a reduction in radius and a corresponding increase in Coulomb energy. However, due to the greater number of protons in the $T_z = -\frac{3}{2}$ member of the pair, a more rapid increase in Coulomb energy results in a positive energy difference. Similarly, for the $J^\pi = \frac{5}{2}^-$ and $\frac{3}{2}^-$ states, an increase in $p_{3/2}$ occupation yields a negative energy difference.

Previous authors have demonstrated macroscopically that this is a real effect through calculations based on a cranked Nilsson potential. This demonstrated that deformation reduces towards a spherical shape as the band termination is approached, and the deformation corrected Coulomb energy for a liquid drop is shown to reproduce the experimental MED for the $T_z = \pm\frac{1}{2}$, $A = 47$ and $A = 49$ mirror pairs [5, 72]. This effect was treated in terms of radii rather than deformation in ref. [6].

The Coulomb multipole term

The Coulomb multipole term can also be interpreted through comparison with the $A=49$, $T_z = \pm\frac{1}{2}$ mirror pair, where an initial gradual increase in V_{CM} followed by a decrease back towards zero was interpreted in terms of particle alignments and blocking effects. In the proton rich member of the mirror pair (^{49}Mn) the single unpaired proton initially prevents the alignment of a proton pair, hence neutrons are first to align in order to produce states of greater angular momentum. The opposite takes place in ^{49}Cr , hence the alignment of protons produces a decrease in Coulomb energy. As the energy differences are calculated as $E^*(^{49}\text{Mn}) - E^*(^{49}\text{Cr})$, this leads to a positive energy difference. Once the neutrons in ^{49}Mn are fully aligned the protons must align in order to produce greater angular momentum, hence the energy difference reduces back toward zero.

In the $^{49}\text{Fe}/^{49}\text{V}$ case, the unpaired proton is in ^{49}V hence we would expect the opposite trend, i.e. an initial decrease to negative energy differences, which then increases

back towards zero. This is essentially what we observe in Fig. 6.3, with the addition of a pronounced staggering effect at low spins. This staggering is likely a result of signature splitting, which is evident in Fig. 5.2 through the enhanced E2 transitions between favoured states up to around $J^\pi = \frac{17}{2}^-$, where M1/E2 transitions become dominant. The V_{Cu} and V_{Cls} terms are included in this component of the calculation for completeness, however their influence is minimal in this instance.

Nuclear isospin-breaking term

The nuclear isospin-breaking contribution to the MED is somewhat smaller than the other components, though is still significant as we shall see below. Similar to the other terms, V_B exhibits a staggering which implies a differing amount of $J = 2$ coupling between the favoured and unfavoured states.

The $A = 49$ MED

The resultant MED curve exhibits an exaggerated staggering at low spin due to the combined effect of the staggering of each individual term. At higher spin the MED increases dramatically, principally due to the radial term.

The experimental MED obtained in this work is plotted in Fig. 6.4, along with the combined results of shell-model calculations described above. The energy differences for both the tentative $J^\pi = \frac{9}{2}^-$ and $\frac{17}{2}^-$ states are included. Excluding these for the time being, the experimental results are well reproduced by the shell-model calculations for the $J^\pi = \frac{11}{2}^-$ and $\frac{15}{2}^-$ states. Although the latter is underestimated by 41 keV, given the limitations of the shell model, this is still reasonable agreement. The predicted small MED value for the $\frac{11}{2}^-$ state is of particular interest as it results from the cancellation of the Coulomb multipole term (negative) and the nuclear isospin-breaking term (positive), with a very small monopole contribution. The agreement between this calculated value and experiment indicates that the empirical method of calculating the nuclear isospin-breaking term, previously only applied to $T_z = \pm\frac{1}{2}$ and ± 1 mirror pairs is still valid for more exotic mirror pairs with greater proton/neutron excess.

Regarding the $J^\pi = \frac{9}{2}^-$ and $\frac{17}{2}^-$ states, the shell model predictions imply that the observed 1101 keV γ ray corresponds to decays from the former (*cf.* Fig. 5.6), while the latter state has not been observed. This can be explained as the $J^\pi = \frac{17}{2}^-$ state

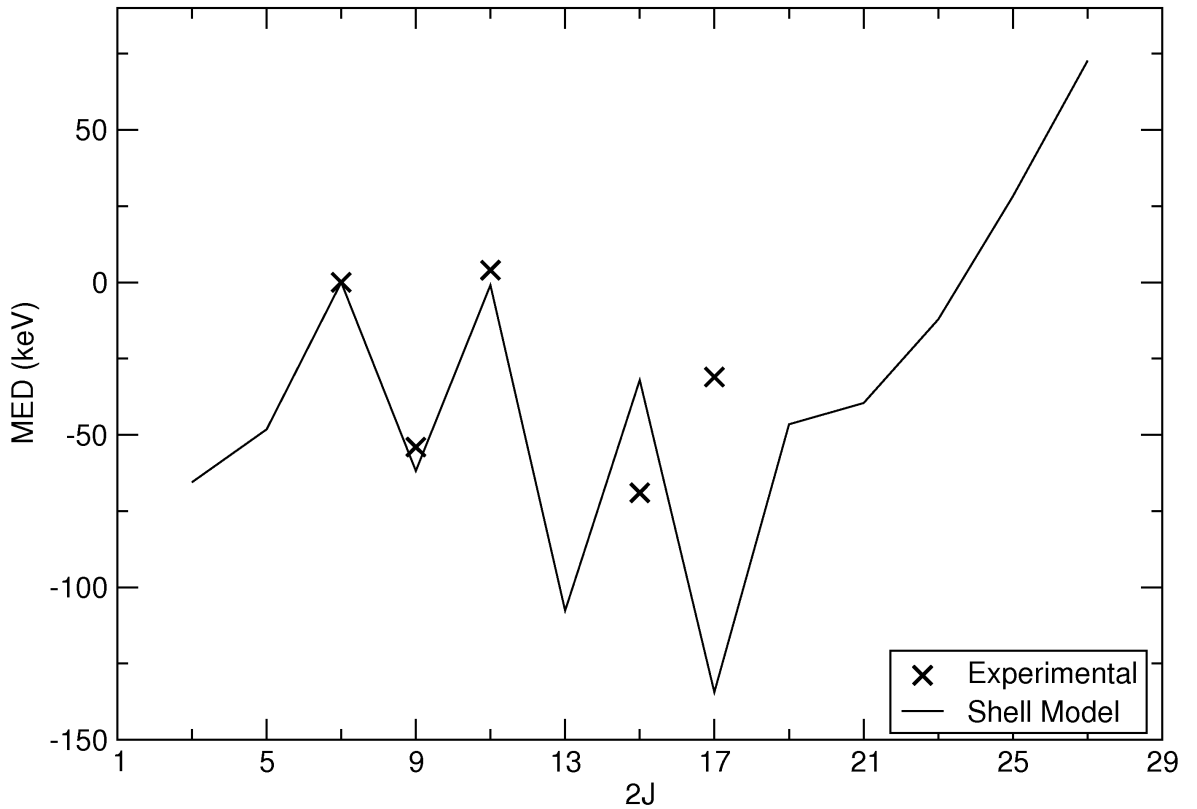


Figure 6.4: Experimental and theoretical mirror energy differences for the $A = 49$, $T_z = \pm\frac{3}{2}$ mirror pair.

is predicted to reside at 3.2 MeV, over 500 keV above the proton separation energy of 2.64 MeV (determined from systematic trends [73]).

Unnatural parity states

As stated in Section 5.1.2, a peak is observed in the γ -ray spectrum of ^{49}Fe at 825 keV with no clear counterpart in ^{49}V (*cf.* Fig. 5.5). Furthermore, shell-model calculations in the fp model space do not predict any states that would decay with the observed energy. Conversely, positive parity states have previously been reported in ^{49}V and attributed to a $K^\pi = \frac{3}{2}^+$ band built upon a particle-hole excitation from the $d_{3/2}$ sub-shell [74]. The decay from the $J^\pi = \frac{3}{2}^+$ band-head to the $J^\pi = \frac{5}{2}^-$ state is observed in this work via a 658 keV γ ray labelled in the spectrum in Fig. 5.1.

Rigorous shell-model calculations of these core-excited states are beyond the scope of this work, however, as has previously been reported [7], the electromagnetic spin-orbit interaction becomes important for states involving excitations from orbitals with $j = l - s$ to one with $j = l + s$, e.g. excitations from $d_{3/2}$ to $f_{7/2}$. This effect can be calculated (as described in Section 1.3.3) using Eqn. 1.13. Using the free values of the

gyromagnetic factors, this leads to an additional difference in single-particle energies of ~ 220 keV between neutrons and protons excited from the $d_{3/2}$ to the $f_{7/2}$ shell. If we assume the $J^\pi = \frac{3}{2}^+$ states are primarily the result of an excitation of the unpaired valence particle (i.e. a proton excitation in ^{49}V , neutron in ^{49}Fe) this would place the isobaric analogue of the ^{49}V , $J^\pi = \frac{3}{2}^+$ state, at ~ 970 keV in ^{49}Fe . Decays from this to the unobserved $J^\pi = \frac{5}{2}^-$ state (i.e. the mirror of the 658 keV transition) would be approximately 880 keV in energy (assuming the observation of this state at 90 keV by Dossat *et al.* is correct [51]). Though this is somewhat higher in energy than the observed 825 keV peak, given that the $J^\pi = \frac{3}{2}^+$ states may not result from a pure $d_{3/2}$ one-particle, one-hole excitation, and that other Coulomb effects have not been considered, this remains a plausible explanation for the observed 825 keV peak.

The striking asymmetry between the intensities of decays from the $J^\pi = \frac{3}{2}^+$ states may be a result of different decay patterns between the two members of the mirror pair, as has previously been observed for parity changing transitions [7, 75, 76]. However, if we were to combine the relative intensities of the two decay paths from the $J^\pi = \frac{3}{2}^+$ state in ^{49}V (see Table 5.1) this would still fall far short of the observed intensity of the 825 keV peak in ^{49}Fe . It should be noted that the 825 keV peak lies upon the expected position of the Compton edge from the 1026 keV decay (*cf.* Fig. 5.5), which may account for some of the intensity of this peak. Nevertheless, some degree of asymmetry seems likely in the population of these analogue states following mirrored fragmentation reactions, as has been observed in the $A=54$ mirror pair. In this case however, due to the larger number of particles removed, a more statistical population of states is expected hence this observation cannot easily be understood.

A final ^{49}Fe level scheme is presented in Fig. 6.5, incorporating the issues discussed above. The 1101 keV γ ray has now been exclusively assigned to the decay from the $\frac{9}{2}^-$ state while the $\frac{17}{2}^-$ state has been removed. $J^\pi = \frac{3}{2}^-$ and $\frac{5}{2}^-$ states have been included, as observed by Dossat, though the ordering of these levels is ambiguous. Despite the absence of intensity measurements, scrutiny of the γ -ray spectrum presented in [51] indicates that the 63 keV transition was slightly stronger, implying it lies lower in the level scheme. Furthermore, these states are degenerate with the analogue states in ^{49}V , hence in disagreement with the negative MED values predicted in Fig. 6.4. Reversal of the ordering however, does little to rectify this situation as, while the $\frac{5}{2}^-$ states would yield an MED of -28 keV, the $\frac{3}{2}^-$ states would remain unchanged. Nevertheless, the

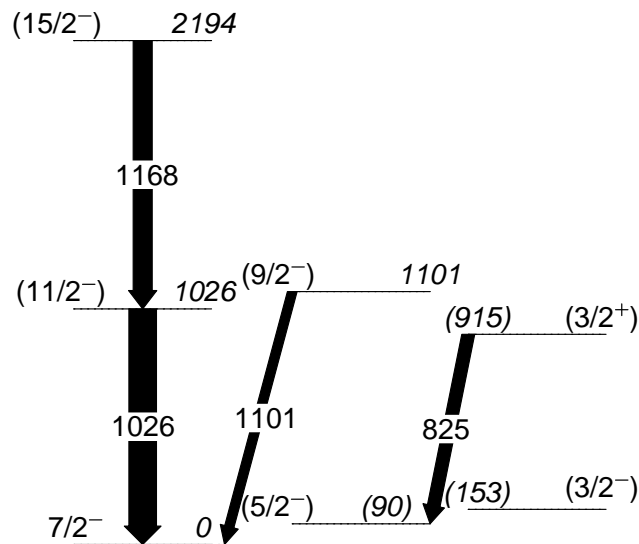


Figure 6.5: Final ^{49}Fe level scheme, taking into account shell-model calculations and incorporating the states observed by Dossat *et al.* [51]. See text for details.

ordering suggested in ref. [51] has been maintained in Fig. 6.5. The 825 keV γ ray is attributed to a decay between a new $J^\pi = \frac{3}{2}^+$ state at 915 keV and the $\frac{5}{2}^-$ state observed by Dossat. Due to the uncertainties described above, the energy of the $\frac{3}{2}^+$ state is assigned tentatively.

6.3.2 The $A=53$ mirror pair

Fig. 6.6 shows the results of calculations of isospin-breaking components for the *yrast* states of the $A=53$, $T_z = \pm\frac{3}{2}$ mirror pair. These calculations were carried out with a truncation of $t=6$ (*cf.* Fig. 6.1).

The range of values displayed in this figure is much greater than that of the $A=49$ mirror pair. This is principally due to the $J^\pi = \frac{13}{2}^-$ state for which all three components plotted are large (either positive or negative). This can be understood when we consider the origin of this state. In a pure $(f_{7/2})^{-3}$ configuration, a $J^\pi = \frac{13}{2}^-$ state cannot be made with three like-particles (holes) due to the limited combinations of m_J states. In order to make such a state, a particle must be excited to the upper *fp* shell. Shell-model calculations indicate that this excitation is principally a particle from the filled $f_{7/2}$ space (i.e. a neutron (proton) in ^{53}Mn (^{53}Ni)) to the $p_{3/2}$ orbital. This excitation represents a significant structural change, hence a significant energy difference may be expected for all isospin-breaking terms.

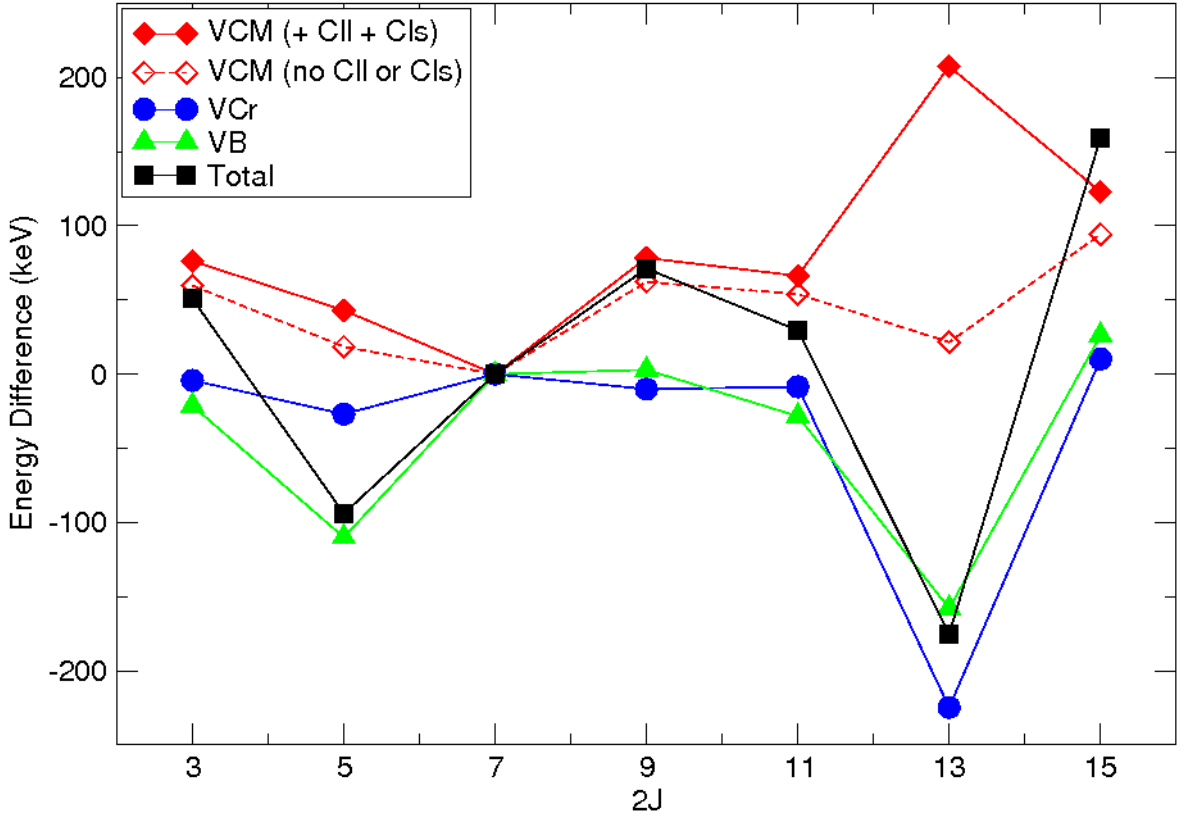


Figure 6.6: Individual isospin breaking contributions to the MED of the $A=53$, $T_z = \pm\frac{3}{2}$ mirror pair, along with the total calculated MED. The V_{CM} term is included with and without the V_{CII} and V_{CIs} terms to indicate the influence of these single-particle effects. (Original in colour.)

The Coulomb multipole term

The Coulomb multipole term can be understood simply in terms particle alignments, as for the $A=49$ mirror pair. In this case, however, as the $f_{7/2}$ shell is full for one particle type there are no blocking effects to consider, hence the V_{CM} term simply increases steadily as angular momentum increases (or decreases) away from the ground state, up to a maximum of ~ 120 keV. The exception to this trend occurs at the $\frac{13}{2}^-$ state where the particle excitation described above causes an additional energy difference due to the V_{CII} and V_{CIs} terms. Aside from this, these single-particle effects have little influence on the overall mirror energy differences.

The monopole radial term

The monopole radial term is generally small for the $A=53$ mirror pair, as we would expect this close to the doubly magic ^{56}Ni shell closure. Again, the exception to this is the $\frac{13}{2}^-$ state where a strikingly large negative energy difference occurs. As described in

Section 6.2, this term is calculated from the occupation of the $p_{3/2}$ orbital. The particle excitation described above will produce a sudden increase in the occupancy of this orbital, hence a sudden jump in the V_{Cr} term. This term is schematically calculated in the hypothesis of rather constant occupation of the f orbits and only changes of the occupation of the $p_{3/2}$ orbit is considered. This is not the case for the $\frac{13}{2}^-$ state, hence application of the usual prescription may not be appropriate here. If we consider the radial monopole term as a deformation effect, rather than a radial one (as has been done by some authors [77]), this result makes even less sense as significant deformation is not expected this close to the shell closure. Nevertheless, the $J^\pi = \frac{13}{2}^-$ state has not been experimentally observed in this work so further discussion of this issue must await such an observation.

Nuclear isospin-breaking term

The nuclear isospin-breaking term shows no particular trend, though is significant for the $J^\pi = \frac{5}{2}^-$, $\frac{11}{2}^-$ and $\frac{13}{2}^-$ states, the latter no doubt a result of the particle excitation.

The $A = 53$ MED

The experimental MED curve for the $A=53$, $T_z = \pm\frac{3}{2}$ mirror pair obtained in this work is plotted in Fig. 6.7, along with the results of calculations of isospin breaking components. The agreement between experiment and theory is good for the observed states, as was observed for the $A=49$ mirror pair.

From Fig. 6.6 we see that the isospin-breaking contribution, V_B , is significant for the observed states, particularly the $J^\pi = \frac{5}{2}^-$ state. In fact, without this term, predictions for this state would fail completely with an MED of the wrong sign.

The large positive MED predicted for the $J^\pi = \frac{15}{2}^-$ state is of interest as the proton separation energy for ^{53}Ni is predicted to be 2.74 MeV [73], implying this state may be unbound to proton decay, though only by ~ 100 keV. Although the Coulomb barrier would likely inhibit any such decay branch, this could provided a possible explanation as to why this state is not observed, and reduced feeding to the $\frac{11}{2}^-$ state may also account for the discrepancies in the observed intensities in Table 5.4. Alternatively, the population mechanism could be a factor contributing to the different decay intensities observed from the $\frac{11}{2}^-$ states as only direct $3n$ removal is energetically favourable for ^{53}Ni , whereas ^{53}Mn can be produced via several additional indirect processes, *cf.* Fig.

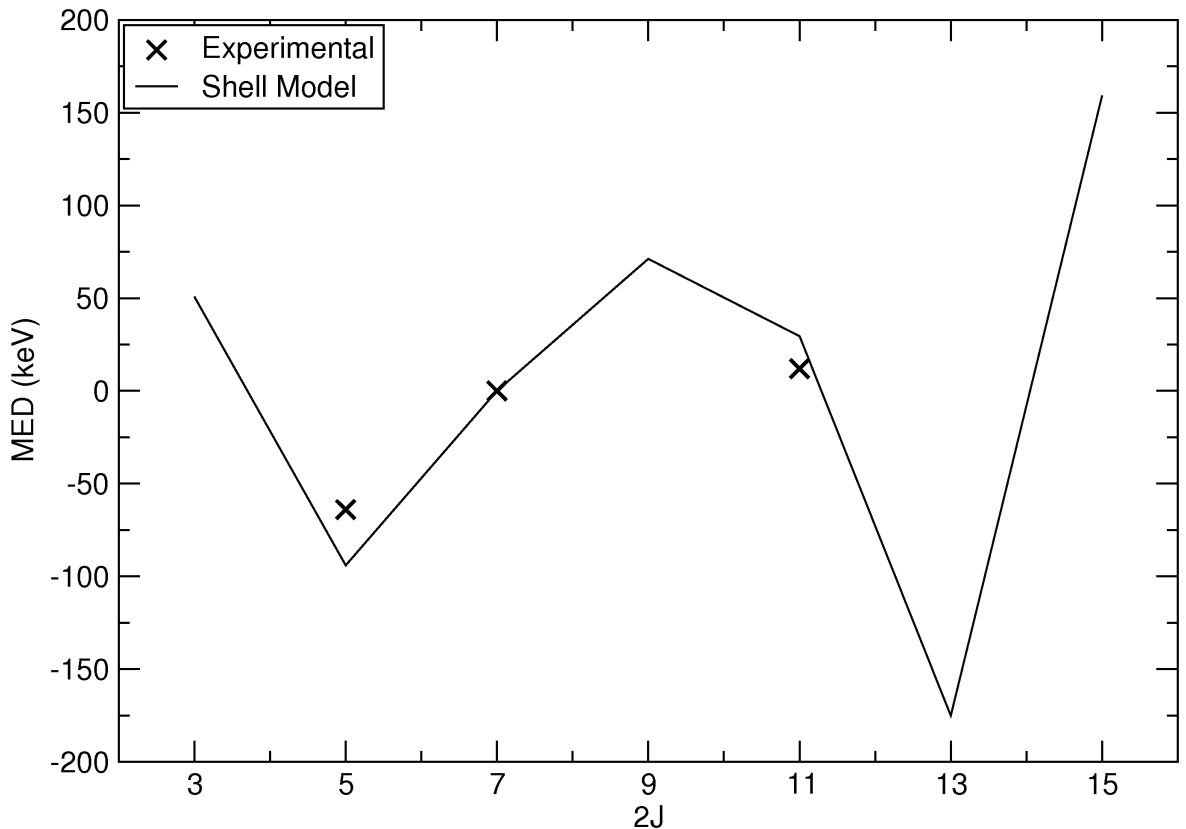


Figure 6.7: The experimental and theoretical MED curves for the $A=53$, $T_z = \pm\frac{3}{2}$ mirror pair.

5.16.

6.3.3 The $A=54$ mirror pair

The MED curve of the $A=54$, $T_z = \pm 1$ mirror pair has been studied previously by Gadea *et al.* [9] and Rudolph *et al.* [62], hence will not be discussed further here. Nonetheless, shell-model calculations were performed to investigate the apparent large differences in the half-lives of the $J^\pi = 6^+$ states. To this end, calculations were performed in the fp model space with a $t=6$ truncation. This was chosen as a compromise between satisfactory convergence of the parameters of interest and practical computational requirements, and has previously been demonstrated to be a suitable truncation [62]. As for the $A=49$ and 53 mirror pairs, calculations were performed using the KB3G interaction with the addition of Coulomb two-body matrix elements and modified effective single-particle energies to account for the V_{Cu} and V_{Cls} interactions. Reduced transition matrix elements ($B(E2)$) were calculated using effective charges of 1.15 and 0.8 for protons and neutrons respectively [78]. The results of these calculations are

Table 6.1: Calculated $B(E2)$ values for $6^+ \rightarrow 4^+$ transitions and half-lives ($t_{1/2}$) for the 6^+ states of ^{54}Fe and ^{54}Ni . Half-lives are calculated using experimental γ -ray energies, see text for details. Experimental values for ^{54}Fe (taken from ref. [55]) are also presented.

	$B(E2)$ (W.u.)	$t_{1/2}$ (ns)
^{54}Fe (exp.)	3.25(5)	1.215(15)
^{54}Fe (calc.)	2.81	1.42
^{54}Ni (calc.)	2.08	1.21

shown in Table 6.1 along with half-lives derived from these results, and experimental values for ^{54}Fe , taken from [55]. $B(E2)$ values are expressed in terms of Weisskopf estimates calculated as:

$$B(E2) = 5.940 \times 10^{-2} \times A^{4/3} = 12.12 e^2 fm^4. \quad (6.4)$$

The calculated $B(E2)$ value for the $6^+ \rightarrow 4^+$ decay in ^{54}Fe is in reasonable agreement with the experimental value and indicates that this transition can be reasonably approximated by a single-particle transition. The $B(E2)$ value for the ^{54}Ni transition is very similar to this, as is the half-life derived from it; a result of the near cancellation of the reduction in $B(E2)$ and increase in γ -ray energy (*c.f.* Eqn. 5.4). The half-life of the ^{54}Ni , $J^\pi = 6^+$ state reported in Section 5.3.2 (41 ps) differs dramatically from the calculated values. Furthermore, using this value with Eqns. 5.1 and 5.4, a $B(E2)$ value of 61 W.u. is obtain. This value is not only at odds with the calculated values, but it suggests an extremely collective $6^+ \rightarrow 4^+$ transition in ^{54}Ni . This value is unrealistically large as $B(E2)$ values in the most deformed states of ^{48}Cr (which lies at the very centre of the $f_{7/2}$ shell and is considered the best rotor in the region) are typically 30 W.u. [79], hence a value double this near the doubly magic ^{56}Ni shell closure seems extremely unlikely.

A further consideration for this anomalous observation is that shell-model calculations predict a very large negative MED value for the *rare* $J^\pi = 4^+$ states in the $A = 54$ mirror pair. These calculations (carried out without the V_{Cu} interaction, as was done in [62] in order to reproduce the MED of the $J^\pi = 8^+$ and 10^+ states) place the second 4^+ state in ^{54}Ni at 3.104 MeV, implying a decay from this to the *grast* 4^+

state—i.e. the analogue of the 757 keV transition prominent in the ^{54}Fe spectra (see Fig. 5.14(a))—would require the emission of a 484 keV γ ray. This value (within the accuracy which can be expected from shell-model calculations of this kind) indicates that the γ -ray peak attributed to decays from the 6^+ state in ^{54}Ni may originate from the *yrare* 4^+ state. A revised level scheme is presented in Fig. 6.8 (b) which shows this possible new state, whilst the $6^+ \rightarrow 4^+$ decay has been reduced to a nominal intensity. The ^{54}Fe level scheme is included for comparison. This new assignment could not only explain the lifetime discrepancies but also the lower than expected intensity of this peak, not to mention recovering the expected symmetry of the γ -ray spectra in Fig. 5.14. The true 6^+ state may have a lifetime so large that it is not observed at all, or is overwhelmed by the 4_2^+ to 4_1^+ transition.

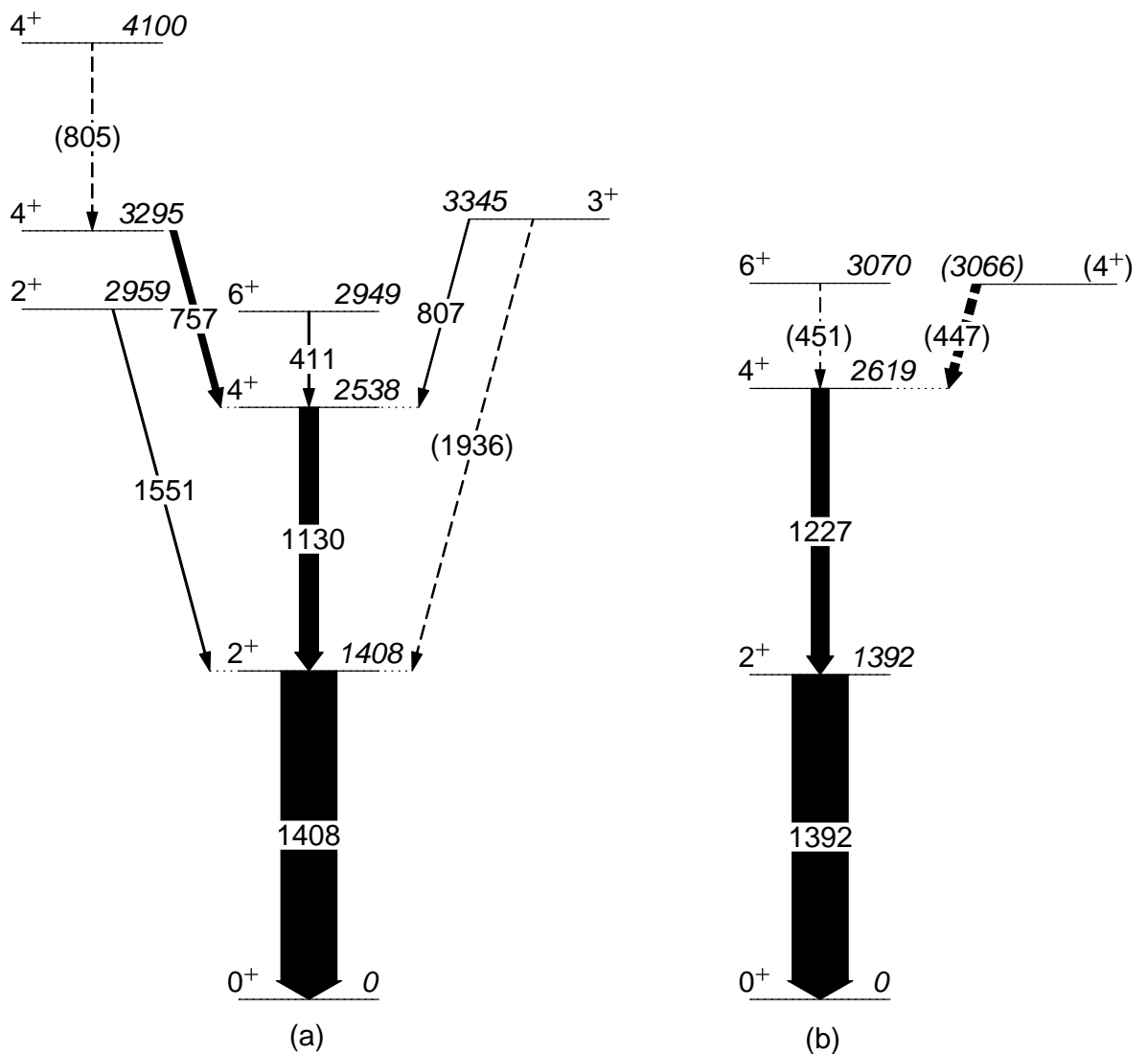


Figure 6.8: (b) Revised ^{54}Ni level scheme following the considerations discussed in the text. (a) ^{54}Fe level scheme for comparison.

It may be expected that such a transition would have been observed in one of the previous studies of ^{54}Ni . However, in the case of Gadea *et al.* [9], ^{54}Ni was produced in a fusion-evaporation reaction which preferentially populates the *yrast* states. In the case of Rudolph *et al.* [62], spectra were produced following the decays of the 10^+ isomer. The isobaric analogue of this state has long been known in ^{54}Fe [55] with no known decay path to the *yrare* 4^+ state, hence this decay would not be observed in this delayed γ -ray spectroscopy experiment.

Given the above considerations, the highly tentative nature of the ^{54}Ni $J^\pi = 6^+$ lifetime measurement (more an indication of a short lifetime, than a true measurement itself), and the further complications of contamination from the stationary 596/608 keV doublet, we must conclude that it is the 4_2^+ state which has been observed. Were it the 6^+ state, the possibility that such unprecedented differences in the nature of a pair of isobaric analogue states (one single-particle like, one collective) has been observed, remains a tantalising prospect which deserves further investigation.

Chapter 7

Conclusions

7.1 The future of fusion-evaporation experiments for the study of proton-rich nuclei

Despite the failure to observe excited states in ^{49}Fe following a fusion-evaporation reaction, such experiments still have a great deal to contribute to modern nuclear structure studies. Though experiments to produce very proton-rich systems are extremely challenging, they allow unrivalled access to high-spin states and when performed with high-granularity Ge array such as Gammasphere, the wealth of information which can be extracted from high-fold γ -ray coincidence analysis is extremely appealing. Though γ decays from excited states of ^{49}Fe were not observed in this work, the possibility to observe extremely weak reaction channels amongst a host of far stronger channels was demonstrated, along with the importance of performing excitation functions to determine the optimum beam energy for many-neutron evaporation channels. Furthermore, significant progress has been made in recent years in performing recoil-decay tagging experiments following fusion-evaporation reactions [29, 80]. Though the suitability of such methods is limited to specific cases, these techniques have allowed access to the smallest of cross sections and present many new possibilities for the study of exotic nuclei approaching the proton dripline.

7.2 Further fragmentation experiments

In contrast to the difficulties experienced with fusion-evaporation reactions, the fragmentation reactions to populate proton-rich nuclei in the $f_{7/2}$ shell, performed at the NSCL, have been shown to be a great success. This experiment, designed as a test of the technique of performing high-luminosity γ -ray spectroscopy following mirrored fragmentation reactions, allowed observation of excited states in both ^{49}Fe and ^{53}Ni : the first *direct* observation of excited states in $T_z = -\frac{3}{2}$ nuclei above $A = 33$ [18]. In addition to these, several other $T_z = -\frac{3}{2}$ nuclei (namely ^{51}Co and ^{47}Mn) were populated at a reasonable level, a full analysis of which has yet to be performed. All of these exotic nuclei were produced in one short experiment, along with all of the $T_z = -\frac{1}{2}$ and -1 nuclei studied since the pioneering work of Cameron *et al.* nearly two decades ago, thus demonstrating the remarkable power of this technique.

Following the success of this test experiment, a full experimental run has been approved at NSCL with the primary aim of performing γ -ray spectroscopy on the $T_z = -2$ nucleus, ^{52}Ni . This shall be achieved by performing an experiment similar to that described in Chapter 4, but running for one week rather than two days. This increased run time, coupled to the increase in beam rate afforded by the utilisation of new, highly-durable diamond timing detectors in place of the plastic scintillators [81] and an upgraded DAQ for SeGA, shall not only allow the first observation of $T_z = -2$ nuclei in the $f_{7/2}$ shell, but will also provide much improved statistics for the $T_z = -\frac{3}{2}$ isotopes, perhaps allowing determination of MED up to the band termination.

Another interesting experiment that presents itself following this work is an accurate measurement of the lifetime of the 6^+ state of ^{54}Ni . This could be achieved using the plunger set-up at NSCL [82] which is suitable for the measurement of lifetimes between 5 and 500 ps. As the S800 could be optimised for ^{54}Ni , rather than the more exotic species studied in the present work, sufficient statistics could be achieved in a very short experiment ($\lesssim 24$ hours) with similar beam currents. Alternatively, a secondary beam of ^{55}Ni could be developed allowing population of ^{54}Ni in a one-neutron knockout reaction. Though this would likely lead to a less intense secondary beam (from the same primary beam), the reaction cross section to ^{54}Ni would increase while the total rate in SeGA would reduce. This will allow an increase in primary beam intensity, potentially reducing the time required for such an experiment.

Even with such a measurement, decays from the $J^\pi = 6^+$ and *rare* 4^+ state must be disambiguated, a task which will require γ -ray spectroscopy with a significant increase in statistics and energy resolution from that achieved in this work. If sufficient high-fold statistics were obtained to observe the 3241 keV decay from the 8^+ state, comparison of a spectrum in coincidence with this transition, with an ungated spectrum should reveal any change in intensity indicating the presence of a 4_2^+ to 4_1^+ decay at an energy comparable to the 451 keV 6^+ to 4_1^+ decay. However, due to the extremely low efficiency of SeGA at high energy, such a measurement may be more suited to experiments with large arrays such as Gammasphere or one of the new generation of 4π arrays currently in development. This again indicates the complementarity of different experimental methods for achieving different experimental goals.

7.3 The status of isospin-breaking phenomena

The experimental observations of new excited states in ^{49}Fe and ^{53}Ni in this work have allowed the calculation of MED curves for $T_z = \pm\frac{3}{2}$ mirror pairs for the first time in the $f_{7/2}$ shell. These MED have been interpreted with the aid of large-scale shell-model calculations with the inclusion of both Coulomb and nuclear isospin-breaking phenomena. These calculations have been shown to be consistent with experimental results, as they have been previously for $T_z = \pm\frac{1}{2}$ and ± 1 mirror pairs. Although this demonstrates our strong understanding of Coulomb isospin breaking effects and the universality of nuclear isospin-breaking forces across the $f_{7/2}$ shell, we are no closer to understanding the nature of this latter phenomenon.

Whichever experimental methods are chosen for future work, observation of $T = 2$ isobaric analogue states, along with additional $T = \frac{3}{2}$ states, is sure to yield further observations of nuclear isospin-breaking phenomena. However, the $J=2$ anomaly remains unexplained and ceaseless collection of data alone shall not rectify this situation. The task is now for theorists to decipher this phenomenon, or to ask more of experimentalists such that the measurements needed for further understanding can be made.

It is striking that the inclusion of nuclear isospin-breaking forces has only been necessary to explain MED in the $f_{7/2}$ shell. This is no doubt a result of the unique nature of this region of the nuclear chart, where a single orbital dominates the wave functions of nuclei. In other regions, nuclear isospin-breaking forces may be masked

by the complexities resulting from multiple sub-shells. However, there exists one other region where a single sub-shell can dominate the wave function of the residing nuclei, namely the $g_{9/2}$ shell. This orbital is less well separated from its neighbours than the $f_{7/2}$ shell, but due to its positive parity (compared to the negative parity of the nearby fp shell), it may be possible to observe states with pure $g_{9/2}$ wave functions and extract detailed isospin-breaking information. The observation of excited states in proton-rich nuclei in this region is beyond the capabilities of current experiments but perhaps with the construction of the new radioactive beam facilities (FAIR, EURISOL and FRIB) and use of the new generation of Ge arrays (AGATA [83] and GRETA [84]), such experiments may be feasible and shed light on a more widespread spin-dependent charge-symmetry breaking component to the nuclear force.

List of Abbreviations

A1900	—	the projectile fragmentation separator at NSCL
ANTOINE	—	an m -scheme shell-model code
ATLAS	—	the Argonne Tandem Linac Accelerator System
BGO	—	bismuth germanate
CCF	—	Coupled Cyclotron Facility
CDE	—	Coulomb Displacement Energy
CME	—	Coulomb Matrix Element
CRDC	—	Cathode Readout Drift Counter
CSB	—	Charge Symmetry Breaking
DAQ	—	Data Acquisition system
E1	—	the first of three plastic scintillators at the focal plane of the S800 separator
EMSO	—	Electromagnetic Spin Orbit interaction
FMA	—	Fragment Mass Analyser
ISOL	—	Isotope Separation On-Line
MCP	—	Micro-Channel Plate detector

MED	—	Mirror Energy Difference
MDE	—	Mirror Displacement Energy
NSCL	—	National Superconducting Cyclotron Laboratory
OBJ	—	a plastic scintillator located at the object position of the S800 spectrograph
PID	—	Particle Identification spectrum
RF	—	Radio Frequency timing signal provided by the accelerator
RFGE	—	a timing signal started by an individual Ge signal and stopped by the RF
RFPR	—	a timing signal started by the RF and stopped by the trigger
RFTAC	—	a timing signal started by the MCP and stopped by a delayed RF signal
RIB	—	Radioactive Ion Beam
S800	—	a high-resolution spectrograph at NSCL
SeGA	—	Segmented Germanium Array
TAC	—	Time-to-Amplitude Converter, used here to refer to a timing signal
TDC	—	Time-to-Digital Converter
TOF	—	time-of-flight
V_B	—	nuclear charge symmetry breaking term
V_{Cu}	—	Coulomb monopole single-particle contribution to CSB proportional to l^2
V_{Cl_s}	—	Coulomb monopole single-particle contribution to CSB resulting from the EMSO interaction

-
- V_{CM} — Coulomb multipole term
- V_{Cr} — Coulomb monopole term resulting from radial changes
- XFP — plastic scintillator located at the *extended* focal plane of the A1900 separator

Bibliography

- [1] R. Machleidt and H. Muther, Phys. Rev. C **63**, 034005 (2001).
- [2] J. A. Nolen and J. P. Schiffer, Annu. Rev. Nucl. Sci. **19**, 471 (1969).
- [3] J. A. Cameron et al., Phys. Lett. B **235**, 239 (1990).
- [4] C. D. O’Leary et al., Phys. Rev. Lett. **79**, 4349 (1997).
- [5] M. A. Bentley et al., Phys. Lett. B **437**, 243 (1998).
- [6] S. M. Lenzi et al., Phys. Rev. Lett. **87**, 122501 (2001).
- [7] J. Ekman et al., Phys. Rev. Lett. **92**, 132502 (2004).
- [8] A. P. Zuker, S. M. Lenzi, G. Martinez-Pinedo, and A. Poves, Phys. Rev. Lett. **89**, 142502 (2002).
- [9] A. Gadea et al., Phys. Rev. Lett. **97**, 152501 (2006).
- [10] S. J. Williams et al., Phys. Rev. C **68**, 011301(R) (2003).
- [11] M. A. Bentley and S. M. Lenzi, Prog. Part. Nucl. Phys. **59**, 497 (2007).
- [12] R. F. Casten, *Nuclear Structure from a Simple Perspective*, Oxford Science Publications, 2nd edition, 2000.
- [13] M. H. Shahnas, Phys. Rev. C **50**, 2346 (1994).
- [14] J. Duflo and A. P. Zuker, Phys. Rev. C **66**, 051304(R) (2002).
- [15] D. D. Warner, M. A. Bentley, and P. Van Isacker, Nature Phys. **2**, 311 (2006).
- [16] J. Ekman, *Mirror Nuclei Isospin symmetry breaking in the mass $A=35$ and $A=51$ mirror nuclei*, PhD thesis, Lund University, 2004.

-
- [17] T. W. Burrows, Nucl. Data Sheets **109**, 1879 (2008).
- [18] R. R. C. Clement et al., Phys. Rev. Lett. **92**, 172502 (2004).
- [19] J. Cerny, C. U. Cardinal, H. C. Evans, K. P. Jackson, and N. A. Jelley, Phys. Rev. Lett. **24**, 1128 (1970).
- [20] M. Bentley et al., Report on test experiment and request for remainder of beam time - proposal 1050, Technical report, 2005.
- [21] C. N. Davids et al., Nucl. Instrum. Methods Phys. Res., Sect. B **70**, 358 (1992).
- [22] J. P. Greene, C. J. Lister, P. Reiter, G. E. Thomas, and K. L. Unterzuber, Nucl. Instrum. Methods Phys. Res., Sect. A **459**, 334 (2001).
- [23] I. Y. Lee, Nucl. Phys. A **520**, C641 (1990).
- [24] F. S. Goulding, D. A. Landis, N. Madden, M. Maier, and H. Yaver, 1995 IEEE Nuclear Science Symposium and Medical Imaging Conference Record, Vols 1-3 , 432 (1996).
- [25] S. J. Freeman et al., Phys. Rev. C **69**, 064301 (2004).
- [26] P. Kent, Private communication, 2007.
- [27] Z. Lin, Master's thesis, University of York, 2006.
- [28] A. Gavron, Phys. Rev. C **21**, 230 (1980).
- [29] A. Korgul et al., Phys. Rev. C **77**, 034301 (2008).
- [30] C. Lister, Private communication, 2009.
- [31] J. Hufner, K. Schafer, and B. Schurmann, Phys. Rev. C **12**, 1888 (1975).
- [32] P. G. Hansen and J. A. Tostevin, Annu. Rev. Nucl. Part. Sci. **53**, 219 (2003).
- [33] D. Bazin et al., Phys Rev Lett **91** (2003).
- [34] K. Yoneda et al., Phys. Rev. C **74**, 021303(R) (2006).
- [35] A. Obertelli et al., Phys. Rev. C **73**, 044605 (2006).

- [36] F. Marti, editor, *Commissioning of the Coupled Cyclotron System at NSCL*, volume 600, American Institute of Physics, 2001.
- [37] D. J. Morrissey, B. M. Sherrill, M. Steiner, A. Stolz, and I. Wiedenhoever, Nucl. Instrum. Methods Phys. Res., Sect. B **204**, 90 (2003).
- [38] D. Bazin, J. A. Caggiano, B. M. Sherrill, J. Yurkon, and A. Zeller, Nucl. Instrum. Methods Phys. Res., Sect. B **204**, 629 (2003).
- [39] J. Yurkon et al., Nucl. Instrum. Methods Phys. Res., Sect. A **422**, 291 (1999).
- [40] R. R. C. Clement, *A New Method for the Nuclear Structure Measurement of Neutron Deficient Nuclei*, PhD thesis, Michigan State University, 2003.
- [41] J. A. Caggiano, *Spectroscopy of Exotic nuclei with the S800 Spectrograph*, PhD thesis, Michigan State University, 1999.
- [42] M. Berz, K. Joh, J. A. Nolen, B. M. Sherrill, and A. F. Zeller, Phys. Rev. C **47**, 537 (1993).
- [43] W. F. Mueller et al., Nucl. Phys. A **734**, 418 (2004).
- [44] W. F. Mueller et al., Nucl. Instrum. Methods Phys. Res., Sect. A **466**, 492 (2001).
- [45] K. Siwek, Private communication, 2007.
- [46] J. P. Cali, *National Bureau of Standards Certificate, Standard Reference Material 4218-C, Europium-152, Point-source Activity Standard*, 1978.
- [47] G. F. Knoll, *Radiation Detection and Measurement*, Wiley, 3rd edition, 2000.
- [48] H. Junde, Nuclear Data Sheets **86**, 315 (1999).
- [49] J. R. Brown et al., Physical Review C **80**, 011306(R) (2009).
- [50] J. A. Cameron et al., Phys. Rev. C **44**, 1882 (1991).
- [51] C. Dossat et al., Nucl. Phys. A **792**, 18 (2007).
- [52] H. Junde, Nucl. Data Sheets **87**, 507 (1999).
- [53] J. F. Ziegler, J. P. Biersack, and U. Littmark, *The Stopping and Range of Ions in Matter*, Pergamon Press, New York, 1985.

- [54] I. M. Szoghy, B. Cujec, and R. Dayras, Nucl. Phys. A **153**, 529 (1970).
- [55] J. D. Junde, H and H. Su, Nucl. Data Sheets **107**, 1393 (2006).
- [56] J. A. Tostevin, European Physical Journal-Special Topics **150**, 67 (2007).
- [57] J. Tostevin, Private communication, 2009.
- [58] J. A. Tostevin, Journal of Physics: Conference Series **49**, 21 (2006).
- [59] J. Tostevin, Private communication, 2008.
- [60] E. C. Simpson, J. A. Tostevin, D. Bazin, B. A. Brown, and A. Gade, Phys. Rev. Lett. **102**, 132502 (2009).
- [61] E. C. Simpson and J. A. Tostevin, Phys. Rev. C **79**, 024616 (2009).
- [62] D. Rudolph et al., Phys. Rev. C **78**, 021301(R) (2008).
- [63] K. C. Chung, A. Mittler, J. D. Brandenberger, and M. T. McEllistrem, Phys. Rev. C **2**, 139 (1970).
- [64] D. M. Mei, S. R. Elliott, A. Hime, V. Gehman, and K. Kazkaz, Phys. Rev. C **77**, 054614 (2008).
- [65] E. Caurier, Shell model code antoine, IReS, Strasbourg, 1989-2004.
- [66] E. Caurier and F. Nowacki, Acta Phys. Pol., B **30**, 705 (1999).
- [67] E. Caurier, G. Martinez-Pinedo, F. Nowacki, A. Poves, and A. P. Zuker, Rev. Mod. Phys. **77**, 427 (2005).
- [68] A. Poves, J. Sanchez-Solano, E. Caurier, and F. Nowacki, Nucl. Phys. A **694**, 157 (2001).
- [69] M. Honma, T. Otsuka, B. A. Brown, and T. Mizusaki, Phys. Rev. C **65**, 061301(R) (2002).
- [70] M. Honma, T. Otsuka, B. A. Brown, and T. Mizusaki, Phys. Rev. C **69**, 034335 (2004).
- [71] W. A. Richter, M. G. Van Der Merwe, R. E. Julies, and B. A. Brown, Nucl. Phys. A **523**, 325 (1991).

-
- [72] M. A. Bentley et al., Phys. Lett. B **451**, 445 (1999).
- [73] G. Audi, A. H. Wapstra, and C. Thibault, Nucl. Phys. A **729**, 337 (2003).
- [74] B. Haas, J. Chevallier, J. Britz, and J. Styczen, Phys. Rev. C **11**, 1179 (1975).
- [75] M. A. Bentley et al., Phys. Rev. C **73**, 024304 (2006).
- [76] D. G. Jenkins et al., Phys. Rev. C **72**, 031303(R) (2005).
- [77] J. Ekman, C. Fahlander, and D. Rudolph, Modern Physics Letters A **20**, 2977 (2005).
- [78] R. du Rietz et al., Phys. Rev. Lett. **93**, 222501 (2004).
- [79] F. Brandolini et al., Nucl. Phys. A **642**, 387 (1998).
- [80] A. N. Steer et al., Nucl. Instrum. Methods Phys. Res., Sect. A **565**, 630 (2006).
- [81] A. Stolz, M. Behravan, M. Regmi, and B. Golding, Diamond Relat. Mater. **15**, 807 (2006).
- [82] A. Chester et al., Nucl. Instrum. Methods Phys. Res., Sect. A **562**, 230 (2006).
- [83] J. Simpson, J. Phys. G: Nucl. Part. Phys. **31**, S1801 (2005).
- [84] M. A. Deleplanque et al., Nucl. Instrum. Methods Phys. Res., Sect. A **430**, 292 (1999).